TAMPERE UNIVERSITY OF TECHNOLOGY

Jaakko Murtomäki

DESIGN AND ANALYSIS OF THE TOOLING UPGRADE FOR THE PRODUCTION OF THE SUPERCONDUCTIVE MAIN DIPOLE MAGNET PROTOTYPES OF LHC

Master of Science Thesis

Examiner: Reijo Kouhia
Examiner and topic approved in the
Engineering Sciences Faculty Council
meeting on 14th August 2013

ABSTRACT

TAMPERE UNIVERSITY OF TECHNOLOGY
Master's Degree Programme in Mechanical Engineering
JAAKKO MURTOMÄKI: Design and analysis of the tooling upgrade for the production of the superconductive main dipole magnet prototypes of LHC
Master of Science Thesis, 110 pages, 12 Appendix pages
September 2013
Major: Design of machines and systems
Examiner: Professor Reijo Kouhia
Keywords: CERN, LHC, High Luminosity LHC project, superconductive dipole magnet, welding press, Nb_3Sn, pre-stress, Ar-inert gas furnace

This thesis work has been carried out as a contribution to the development program of superconductive magnets within the LHC High Luminosity study. The thesis provides an insight to the steps that need to be taken in order to produce a superconductive magnet mainly focusing on mechanical assembly. Tooling upgrade is necessary for the production of the superconductive dipole magnet prototypes in near future.

Major attention is given by the introduction of the welding assembly in chapter three. The structural compression is given by the so called shell stress defined by the thermal shrinkage of the weld. The associated aspects include the closure of the gap in the half symmetry of the assembled mock-up. All this is important to minimize the risk for the quenches in the superconductive coil assembly.

In the chapter four all the related constraints seen by the magnet are implied into the FEA model to find out the required minimum shrinkage of the weld. It was necessary to verify that the coil stresses stay below the defined limit during the pressing of the magnet and welding, after the welding procedure, as well as the cooling to 1.9 K followed by operation at nominal current 13 kA (12 T).

An aspect is given to the modifications performed for the sample press. The specification of the press implied the analysis of the required hydraulic system, user control interface and coordination of related activities.

The luminosity upgrade involves the utilization of the Nb_3Sn superconductor. The diffusion process of the Nb_3Sn towards superconductive characteristics implies the stringent heat treatment cycle. An Ar-inert gas furnace is used. It is important to select the appropriate numerical methods to verify critical process parameters as the ramping rate [°C/h] and the circulation speed of the used Ar-inert gas [m/s].

This implies the definition of the appropriate numerical methods to carry out an analysis with the aid of CFD. The analysis should provide solid backround for further development of the analysis of heat transfer between the furnace and the coil.

TIIVISTELMÄ

TAMPEREEN TEKNILLINEN YLIOPISTO
Konetekniikan koulutusohjelma
JAAKKO MURTOMÄKI: Design and analysis of the tooling upgrade for the production of the superconductive main dipole magnet prototypes of LHC
Diplomityö, 110 sivua, 12 liitesivua
Syyskuu 2013
Pääaine: Koneiden ja järjestelmien suunnittelu
Tarkastajat: Reijo Kouhia
Avainsanat: CERN, LHC, High Luminosity LHC-projekti, suprajohtava dipolimagneetti, hitausprässi, Nb_3Sn, esijännitys, Ar-inertti-kaasu-uuni

Tämä diplomityö on tehty osana LHC:n High Luminosity-tutkimusprojektia. Diplomityö tuo katsauksen niihin askeliin, jotka on otettava suprajohtavan magneetin valmistamisessa pääosin keskittyen mekaaniseen kokoonpanoon. Työvälineiden päivitys on tärkeää suprajohtavien dipolimagneettien prototyyppien valmistamiseksi lähi- tulevaisuudessa.

Suuri painoarvo annetaan magneetin hitsauskokoonpanon esittelylle kolmannessa kappaleessa. Rakenteen puristustila aiheutetaan niin sanotulla magneetin kuoren jännityksellä, jonka määrää hitsisauman kutistuma. Siihen liittyvät näkökohdat sisältävät raon sulkeutumisen kokoonpannun magneettimallin puolisymmetriassa. Kaikki tämä on tärkeää quench-ilmiön esiintymisen minimoimiseksi suprajohtavassa kelakokoonpanossa.

Neljännessä kappaleessa kaikki magneetille asetettavat rajaehdot sisällytetään FEA-malliin hitsisauman pienimmän tarvittavan kutistuman löytämiseksi. Kelajännityksien pysyminen määritellyn raja-arvon alla oli todennettava prässäyksen ja hitsauksen aikana, hitsauksen jälkeen, 1.9 K:iin jäähdytyksen jälkeen sekä magneetin käytön aikana sen nimellisvirralla, 13 kA (12 T).

Yksi näkökohta on lyhyiden magneettimallien prässin muunnostyö. Prässin määrittely vaati tarvittavan hydraulisen järjestelmän ja sen käyttöliittymän analyysiä sekä muunnostyöhön liittyvien toimintojen koordinointia.

Luminositeetin kasvattaminen vaatii Nb_3Sn-suprajohteen käyttöä. Nb_3Sn-suprajohteen diffuusioprosessi kohti suprajohtavuutta edellyttää tiukkaa lämpökäsittelysykliä. Kelan käsittelyssä käytetään argon-inertti-kaasu-uunia. On tärkeää valikoida soveltuvat numeeriset menetelmät kriittisten prosessiparametrien määrittelemiseksi, kuten lämmitysramppi [°C/h] ja inertin Ar-kaasun kiertonopeus.

Tämä edellyttää sopivien numeeristen menetelmien määrittelyä analyysin suorittamiseksi CFD:n avulla. Analyysin pitäisi taata tukevan taustan uunin ja kelan lämmönsiirron analyysin jatkokehittelylle.

PREFACE

I had the chance to work at CERN as a technical student for 14 months. I feel it is a priviledge to experience this environment, and work with people who share same interests and values. The development program of new superconductive magnets utilizing Nb_3Sn-technology within the High luminosity study provides highly interesting topics to work with. As a work environment, the LMF-section is a special case at CERN. It is a huge industrial facility that is mostly manned by technicians and few engineers. I want to thank all people who work there, or shared their lunch breaks or coffee pauses with me.

I want to thank Friedrich Lackner and Frédéric Savary of their instructive and helpful support with the analysis and thesis writing process. The thesis writing process proved to be the most difficult part due to complexity of the topics. I'm happy that Friedrich shared his experience and knowledge and I had the chance to learn many new things with his aid. The examiner professor Reijo Kouhia gave me numerous hints about how to enhance the appearance of the thesis. Many thanks to him.

I want to thank people of Aldiance-Linatec-Dimat for their contributions to the improvement of the press. Especially I want to thank Tony Letailleur and Emmanuel Dakin for their help with the development of the press user interface.

I want to thank colleaques in my office, who created an inspiring and funny atmosphare; Thomas Van Puyenbroeck, who shared part of the work with the furnace heat transfer model; Raul Moron-Ballester, who gave me many suggestions and advices about many topics; Jean-Francois Rakotoarison, who inspired me with his thoughts, and Emile Grospelier, who supported me with CAD of the press.

I send my thanks to Henri Riihimäki, who helped me during difficult moments with CFD-codes. I also want to thank Valentina Venturi for her important support with the thesis. Finally I want to thank my family, relatives and friends of their invaluable support during the years of studying.

Tampere, September 23, 2013

ALKUSANAT

Minulla oli mahdollisuus työskennellä CERN:issä 14 kuukautta technical student-sopimuksella. Tunnen että olen etuoikeutettu saadessani kokea tämän ympäristön ja työskennellessäni ihmisten kanssa jotka voivat jakaa samoja arvoja ja kiinnostuksen kohteita. Uusien Nb_3Sn-teknologiaan perustuvien suprajohtavien magneettien kehitystyö High Luminosity-tutkimusprojektin puitteissa takaa mielenkiintoiset aiheet, joihin syventyä. Työympäristönä LMF-jaos on erityistapaus. Se on valtava teollinen tila jota miehittävät pääasiassa teknikot ja vähälukuiset insinöörit. Haluan kiittää kaikkia siellä työskenteleviä, jotka olivat tekemisissä kanssani tai jotka jakoivat lounastuntinsa tai kahvipaussinsa kanssani.

Haluan kiittää Friedrich Lackneria ja Frédéric Savarya heidän ohjaavasta tuestaan tehtävien analysoinnin ja diplomityön kirjoittamisen kanssa. Diplomityön kirjoitusprosessi osoittautui vaativimmaksi osioksi aihealueiden monimutkaisuuden vuoksi. Olen iloinen että Friedrich jakoi avokätisesti kokemustaan ja tietoaan, ja että sain oppia uusia asioita hänen avullansa. Diplomityön ulkoasuun sain lukuisia parannusehdotuksia tarkastaja professori Reijo Kouhialta, joten kiitokset kuuluvat myös hänelle.

Haluan kiittää Aldiance-Linatec-Dimatin henkilökuntaa heidän osastaan prässin päivittämisessä. Erityisesti haluan kiittää Tony Letailleuria ja Emmanuel Dakinia heidän kärsivällisestä avustaan prässin käyttöliittymän kehitystyössä.

Haluan kiittää toimistoni työtovereita, jotka loivat inspiroivan ja hauskan ilmapiirin; Thomas Van Puyenbroeckia joka jakoi kanssani osan uunin lämmönsiirtomallin kehitystyöstä; Raul Moron-Ballesteria joka antoi minulle monia ehdotuksia ja neuvoja useista eri aihepiireistä; Jean-Francois Rakotoarisonia joka inspiroi minua ajatuksillaan ja Emile Grospelieriä joka tuki minua prässin tietokoneavusteisella suun- nittelulla.

Kiitokset kuuluvat Henri Riihimäelle, joka tarjosi apuaan vaikeina hetkinä CFD-ohjelmien kanssa. Haluan myös kiittää Valentina Venturia hänen tärkeästä tuestaan diplomityön kanssa. Lopulta haluan kiittää perhettäni, sukulaisiani ja ystäviäni heidän korvaamattomasta ja kestävästä tuestaan opiskeluvuosien aikana.

Tampereella, 23. syyskuuta, 2013

CONTENTS

TERMS AND THEIR DEFINITIONS

ABBREVIATIONS

ADR	Adiabatic Demagnetization Refrigerator
CFD	Computational Fluid Dynamics
CERN	Conseil Européen pour la Recherche Nucléaire
FEA	Finite Element Analysis
FNAL	Fermi National Accelerator Laboratory (Fermilab)
GUI	Graphical User Interface
ITER	International Thermonuclear Experimental Reactor
LHC	Large Hadron Collider
HL-LHC	High LuminosityLarge Hadron Collider
LMF	Large Magnet Facility Section
MFISC	A 1 m long, 50-mm-twin-aperture NbTi cryo-dipole magnet for LHC
MSC	Magnets, Superconductors and Cryostats Group
NASA	National Aeronautics and Space Administration
Nb_3Sn	Niobium-3-Tin
NbTi	Niobium-Titanium
PID	A proportional-integral-derivative controller
RF-cavity	Radio Frequency cavity
TE	Technology Department

SYMBOLS

a_1	SST-model constant
$\mathbf{B}$	Magnetic field
$c_{1\varepsilon}$	$k-\varepsilon$-turbulence model constant
$c_{2\varepsilon}$	$k-\varepsilon$-turbulence model constant

c_p	Specific heat capacity of the fluid in constant pressure
c_{ps}	Specific heat capacity of the solid
C_s	Momentum source term coefficient
C_μ	$k-\varepsilon$ turbulence model constant
dF	Net force on a differential volume element
dV	Differential volume element
$\mathbf{E}$	Electric field
E_y	Young's modulus, y-axis direction
E_x	Young's modulus, x-axis direction
$\mathbf{F}$	Lorentz force vector
f	Force density
F_1	Blending function
F_2	Blending function
f_w	Weld surface load
f_p	Unit load of the press
f_{pd}	The uniformly distributed press load
G	Spectral incident radiation
G_{xy}	Shear modulus
$I_{\nu 0}$	Radiation intensity leaving the boundary
I_ν	Mean radiation intensity
k	Turbulence kinetic energy per unit mass, the variance of the fluctuations in velocity
K_a	Absorbtion coefficient
L	Luminosity
$\dot{N}$	Interaction rate
p	Pressure

P_k	Turbulent kinetic energy production
q	Volumetric heat source of the fluid
q_e	Point charge
q_r	Radiative heat flux
q_s	Volumetric heat source of the solid
$\mathbf{r}$	Position vector
$\mathbf{s}$	Direction vector
s	Path length
S	Strain rate (strain invariant)
S_i	Radiation intensity source term
T	Temperature of the fluid
t	Time
Ts	Temperature of the solid
$\vec{u}$	Fluid velocity vector
u_{av}	Average displacement
$\vec{u}_s$	Velocity vector of the solid
u_x	Component of velocity in x-direction
v	Computational velocity parallel to y-axis
$\mathbf{v}$	Velocity vector
v_{spec}	Specific velocity of the fan
α	Heat transfer coefficient
α_y	Secant coefficient of thermal expansion, y-axis direction
α_x	Secant coefficient of thermal expansion, x-axis direction
β^*	SST-model constant
Δp	Algebraic difference between the mean total pressure at the fan outlet and the mean total pressure at the fan inlet

ε_ν	Spectral emissivity
λ	Thermal conductivity of the fluid
λ_s	Thermal conductivity of the solid
μ	Molecular (dynamic) viscosity
μ_{eff}	Effective viscosity
μ_t	Turbulence viscosity
ν	Frequency
ν_{yx}	Minor Poisson's ratio
ν_{xy}	Major Poisson's ratio
ρ	Density
$\sigma_{avg,4}$	Average stress in the fourth load step
σ_k	Turbulent Prandtl number for k
σ_{k1}	SST-model constant
σ_{k2}	SST-model constant
$\sigma_{\mathrm{P0.2}}$	Elastic limit of the shell with offset strain of 0.2
ε	Turbulence dissipation rate, the rate at which the velocity fluctuations dissipate
σ	Particle beam cross-section area in the accelerator beam channel
σ_{COA}	Allowable coil stress
σ_{D}	Design stress
$\sigma_{\mathrm{P0.2}}$	Elastic limit of the shell (steel) 316LN
σ_{SHA}	Allowable shell stress
σ_ε	$k-\varepsilon$-turbulence model constant
σ_ω	Turbulent Prandtl number for ω
$\sigma_{\omega 1}$	SST-model constant
$\sigma_{\omega 2}$	SST-model constant

Φ	In-scattering phase function
Ω	Solid angle

1. INTRODUCTION

CERN, the European Organization for Nuclear Research, is an intergovernmental organization including 20[1] member states. The seat of CERN is located in Geneva but its establishments are situated astride the French-Swiss border.

CERN's mission is to capacitate international collaboration in the field of high-energy particle physics research. It designs, builds and operates particle accelerators and the associated experimental areas. CERN's installations are at present exerted by more than 10000 scientific users from research institutes all over the world. The accelerator complex of CERN consists of successive interconnected accelerators. A beam of particles is injected from a linear accelerator to other accelerators (rings), which bring the beam to higher energies. The Large Hadron Collider (LHC) seen in Figure 1.1 is the flag ship of this fusion of accelerator rings.

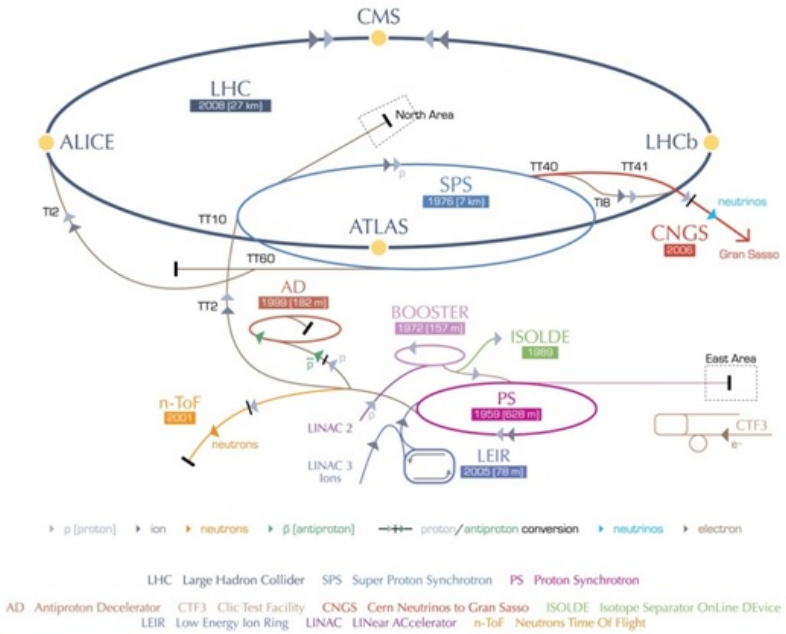

Figure 1.1: An overview of the CERN accelerator complex.

[1] The CERN Member States are currently Austria, Belgium, Bulgaria, the Czech Republic, Denmark, Finland, France, Germany, Greece, Hungary, Israel*, Italy, the Netherlands, Norway, Poland, Portugal, Romania**, the Republic of Serbia*, the Slovak Republic, Spain, Sweden, Switzerland and the United Kingdom. * Associate Member State in the pre-stage to Membership ** Candidate for accession

CERN is currently organized in eight departments:

- Physics - PH
- Beams - BE
- Information Technology - IT
- Technology - TE
- Engineering - EN
- Human Resources - HR
- Finance, procurement and Knowledge Transfer - FP
- General Infrastructure Services - GS

The Technology department (TE) of CERN is responsible for technologies which are specific to existing particle accelerators, facilities and future projects. [34]

The Magnets, Superconductors and Cryostats (MSC) group is part of the TE-department. The mandate of the MSC-group is:

- Design, construction and measurement of superconducting and normal conducting magnets for the CERN accelerator complex
- Responsibility of the magnet integration in the CERN accelerator complex and quality control of magnets and magnet cryostats
- Support to operation of accelerators and magnets, magnet performance and current leads
- Development of associated technologies, namely superconductors, insulation and polymers, superconducting electrical devices and magnetic measurements for present and future accelerators. [35]

A major R&D project in program is given by the upgrade of the LHC cryo-dipole magnets in order to support High Luminosity (HL-LHC) project.

The Large Magnet Facility section (LMF) is part of the MSC-group. The mandate of the LMF-section is:

- CERN-wide support for the engineering, manufacturing and maintenance of superconducting accelerator magnets
- Responsibility of installation, commissioning and operation of the LHC Large Magnet Facility
- Engineering, manufacture and maintenance of busses, electrical joints and interconnects. The LMF-section is responsible for production technologies, tooling development and procurement as well as installation and operation of the polyimide laboratory
- Responsibility of logistics and storage management of spare parts, cold masses and complete magnets [36]

1.1 LHC and the High Luminosity LHC (HL-LHC) project

The LHC is the youngest accelerator in operation on the CERN site. The accelerator is installed in a 27 km circumference tunnel, about 100 m underground. It accelerates and collides proton beams as well as heavier ions up to lead. The LHC design is based on superconducting twin-aperture cryo-magnets. They operate in a superfluid helium bath at 1.9 K. [6]

To fully exploit LHC's physics potential after 2017 up to about 2030, a very ambitious upgrade of the LHC luminosity by a factor 5 (also known as upgrade Phase II) was deemed necessary. [37] Luminosity L is the parameter to measure the number of particle collisions, and it is defined as follows:

$$L = \frac{\dot{N}}{\sigma} \tag{1.1}$$

where $\dot{N}$ is the interaction rate and σ the particle beam cross-section area in the accelerator beam channel

For the upgrade, it is necessary to provide a beam with more intense lower emittance. [6] To enable the ambitious luminosity upgrade, it is essential to replace the triplet magnets and realize all hardware changes needed.

The LHC commissioning and especially the incident of September 2008 just after the LHC start-up, evoked delays to the schedule. That has significantly modified the scenario for the replacement of the triplet magnets. To minimize the machine stops and maximize the productive use of the LHC for physics, the upgrade will now take place in one stop, at around 2020. This new phase of the LHC life has been named as High Luminosity LHC (HL-LHC) and it has the scope of attaining the integrated luminosity threshold of 3000 fb^{-1} in 10-12 years. All the hadron colliders in the

world have so far produced a total integrated luminosity of about 10 fb^{-1}, while the LHC will deliver about 200-300 fb^{-1} at best in its first 10-12 years of life. [37]
All this will be attained by improving the LHC Injector chain, and by developing the hardware baseline:

- New stronger and larger aperture quadrupoles that utilize Nb_3Sn superconductor with the field in 11-13 Tesla range along with new NbTi superconducting dipoles and quadrupoles in the interaction regions and matching sections;

The more powerful magnets require also improvements on the periferic devices, like:

- New helium cryogenic plants and new electrical power supplies;
- Novel superconducting RF-cavities rotating the beam in the interaction regions (Crab Cavities), complemented with their power systems and controls;
- New beam collimators, based on advanced material and new concepts. [6] Collimators are used to maximize the beam intensity, and a powerful collimation system is required to handle the ultra-intense LHC-beams in a super conducting environment. [8] They are foreseen in conjunction with a new type of LHC dipole, rated for 11 T as a replacement of the 8.33 T and with a shorter length in order to ensure the necessary longitudinal space for the collimator in the cold zone;[8; 6] CERN and FNAL have activated a joint development program to demonstrate the feasibility of Nb_3Sn technology for the purpose. Single-, and twin-aperture magnets are currently under development (Figure 1.2). [1]
- CERN has started a development program for high field magnets based on brittle Nb_3Sn superconductors. The superconducting coil needs to be heat treated in an inert gas furnace. For this it is necessary to develop heat treatment procedures for the coils with industrial furnaces. [6]

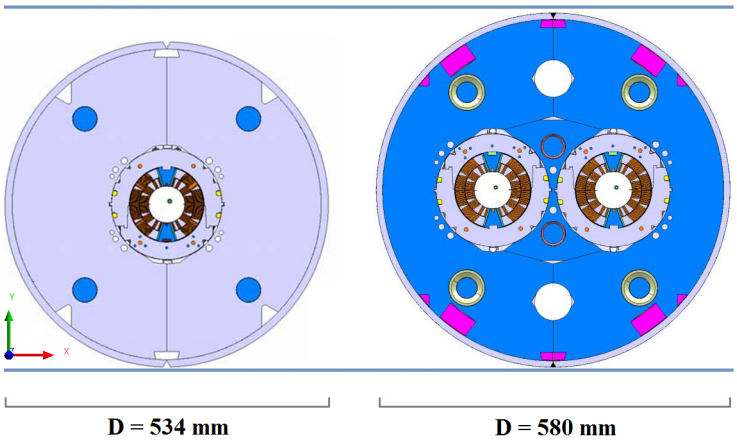

Figure 1.2: Intersections of the new single (1-in-1, left) and twin aperture (2-in-1, right) dipole magnets. [4]

1.2 Contributions of the Large Magnet Facility Section

The Large Magnet Facility Section has to modify its tooling and equipment for the future production of the superconductive magnets using Nb_3Sn superconductor.

The plan is to primarily develop 2 m long magnet models before proceeding to the production of prototypes, which are longer. The short models will lead the way for the production of longer dipole and quadrupole magnet designs in future with a foreseen length of 6,5 m.

For the mentioned purposes the tooling used for the series production of the LHC main magnets had to be upgraded. One chose to improve the existing welding press from the company Fjellman for magnet shell welding. To understand the utilization of the tooling in more detail, a finite element analysis (FEA) was performed.

Additionally the change to the brittle Nb_3Sn superconductors led to a requirement to purchase a new furnace for the heat treatment of superconducting coils. Too high thermal gradients inside the coils may provoke degradation of the superconductor quality, and makes the heat treatment a delicate procedure. The heat treatment had to be analyzed using computational fluid dynamics (CFD), because no previous knowledge about this procedure existed at CERN.

Currently at ITER, the conductors based on Nb_3Sn technology are used in the superconducting magnets of the experimental tokamak nuclear fusion reactor [9]. The superconducting material for the toroidal field coils and the central solenoid is designed to attain high magnetic field (13 Tesla). [33] NASA is using th Nb_3Sn technology for lightweight low-current Adiabatic Demagnetization Refrigerator (ADR) magnets operating at 10 K and for Variable Gravity Testbed Facility.[7; 10]

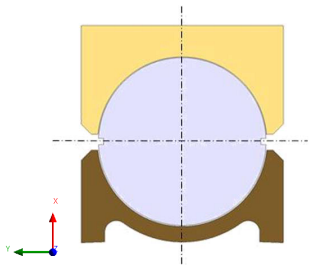

Figure 1.3: The hydraulic load is applied by the cradles to the magnet assembly. [4]

This thesis includes the work of the author relative to the introduced contributions on going at LMF-section. It has been divided into three parts. The first part (Chapter 3) introduces the dipole magnet assembly and tooling.

The second part (Chapter 4) describes the FEA completed to find out if the closure of the yoke-yoke gap inside the magnet by welding is feasible using the cradles seen in Figures 1.3, 1.4, 1.5. The use of cradles implies that the hydraulic force of the press is applied to the magnet assembly by cradles located above and below the magnet assembly (1.3).

The third part (Chapter 5) describes the upgrade of the welding press at LMF-section designed for the pressing of the magnet with cradles. For that, the hydraulic equipment and control interface as well as the press frame have been modified.

The fourth part (Chapter 6) describes the application of CFD to simulate heat transfer in a furnace between a retort box and a fixture containing a superconducting coil. The heat transfer is enhanced with a turbulent flow in an inert gas environment of the retort.

The fifth part (Chapter 7) includes the comprehensive summary of the thesis.

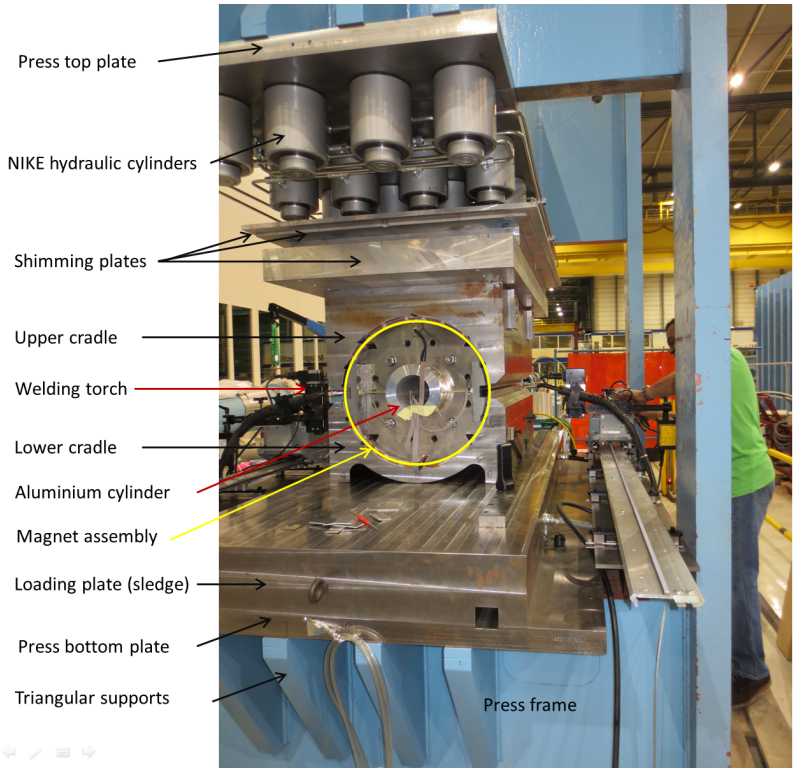

Figure 1.4: The improved press with a dummy dipole magnet assembly to be welded under the press load. The coil has been replaced by the aluminium cylinder. [24]

Figure 1.5: A dummy dipole magnet assembly subject to press load by the cradles undergoes shell test welding operation. The rails and the table of the magnet introduction system can be seen in front. [24]

2. INTRODUCTION OF THE MECHANICAL STRUCTURE OF THE DIPOLE MAGNET AND TOOLING

2.1 Introduction of the main parts of the dipole magnet assembly

A dipole magnet assembly can be seen in Figure 2.1. The magnet consists of two shells, yoke laminations, collars and the coils. The shell is the outer rolled austenitic steel plate structure that supports the magnet assembly. Cylindrical shell halves are manufactured by rolling steel plates, but the shape of the rolled plates is not perfectly round.

The purpose of the yoke is to transfer forces from collared coils assembly to the shells, but also to act as a medium for the magnetic field.

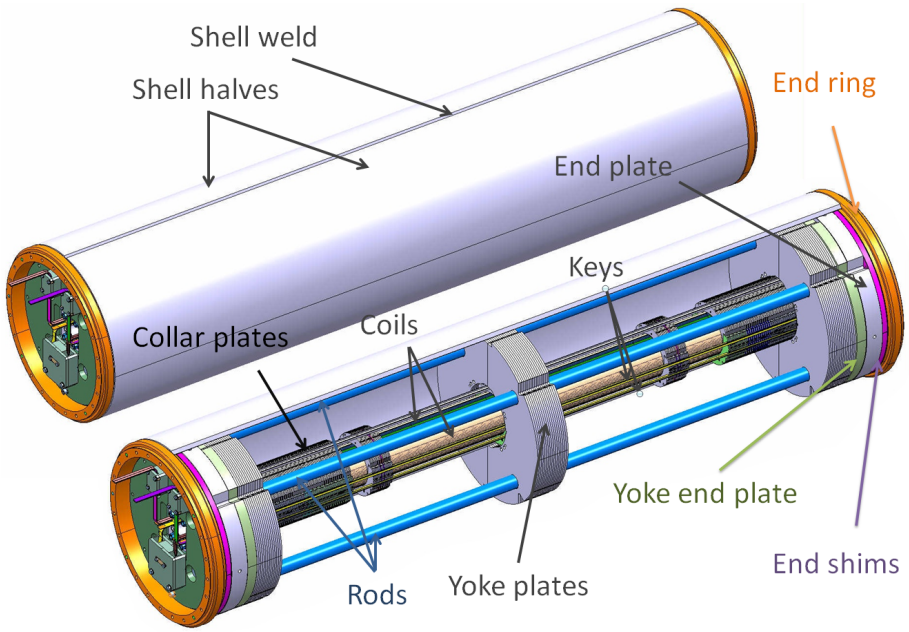

Figure 2.1: A Single aperture 11-T dipole magnet (1-in-1) with and without a shell. The shell assembly is to be welded together from two rolled metal plates. The yoke is made by stacking steel plates. [27]

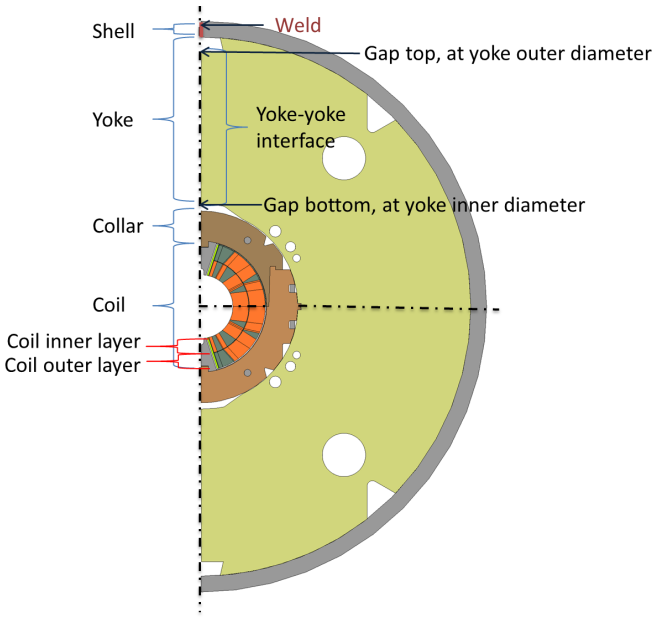

Figure 2.2: An intersection of the single-aperture dipole magnet. The location of the shell weld seam can be seen on the symmetry line. The coil is divided into into inner and outer layers. [26]

The yoke consists of steel plates, and the detailed drawing of the yoke can be seen in Figure 2.9 in the Appendix on the page 14.

An intersection of a half of a dipole magnet can be seen in Figure 2.2. The overlapping collar plate assembly protects, supports and provides the right shape of the coils. Collars are secured by keys that are shown with more detail in Figure 2.3.

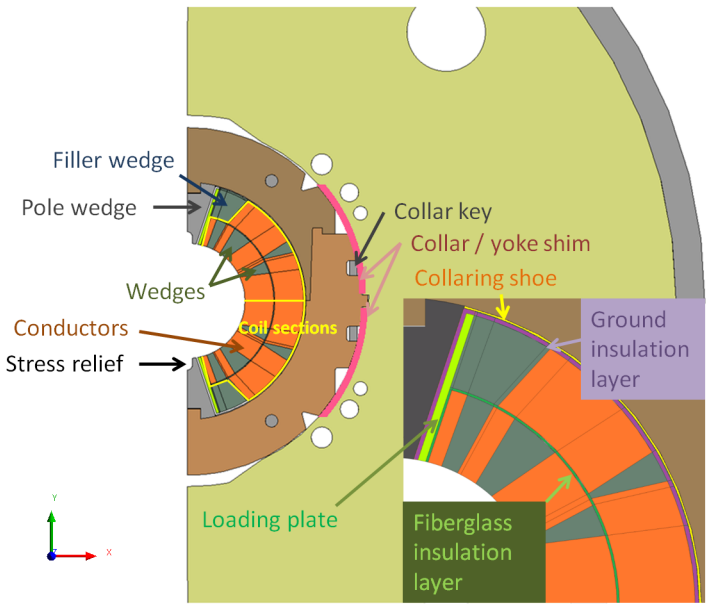

Figure 2.3: A close-up from the single-aperture magnet intersection. Coil sections consist of conductors and wedges molded in Epoxy filled blocks. [26]

The beam channel is the circular space (aperture) located inside the coils where the particles circulate.

2.2 The collar and coil design

The magnet assembly features a removable pole design, which is inspired by MFISC-model (Figure 2.4 and 2.5) [2].

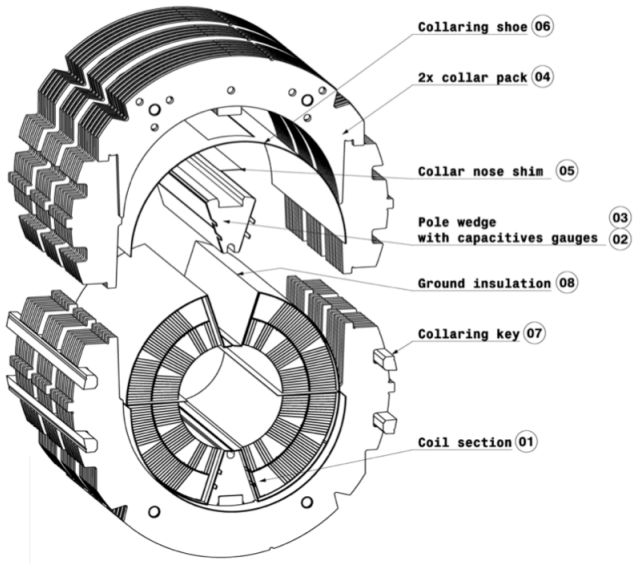

Figure 2.4: The collared coil assembly. The removable pole wedges can be seen. [30]

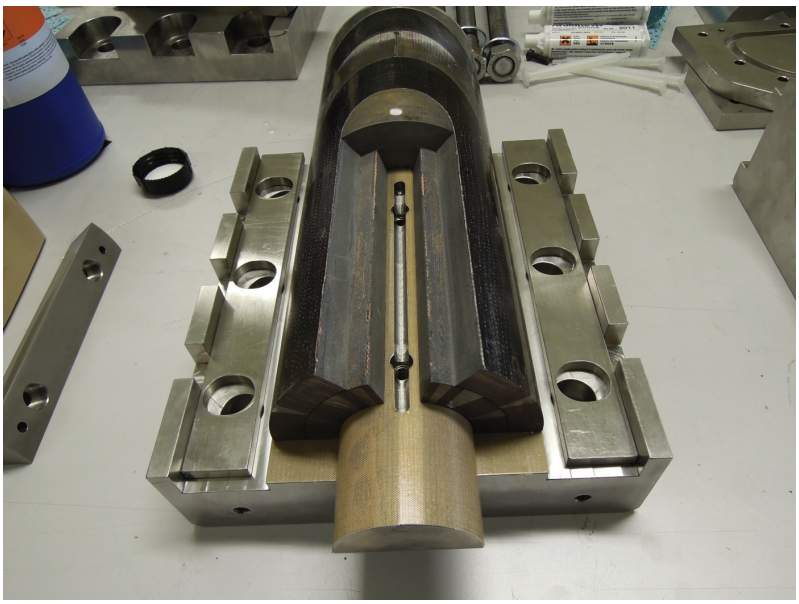

Figure 2.5: 7 Extremity from practice coil type FNAL PC01 (Nb_3Sn). [31]

The collar thickness was adopted to obtain maximum stiffness within the available space. The aim was to attenuate the spring-back effect after the collaring process, in which the collars are installed around the coils with a collaring press.

The removable pole design provides means to adjust the coil pre-compression at the poles. In order to match the azimuthal size of the inner layers (coil sections and wedges) to simplify the pole wedge geometry as shown in Figure 2.3, an ancillary Cu-alloy filler wedge is added to the outer layer. A stainless steel loading plate is positioned between the coil and the pole wedge to protect the fragile Nb_3Sn coils during the collaring process. [1]

2.3 Cradles

For the utilization of cradles to press the magnet assembly, a new cradle geometry was defined (Figure 2.6).

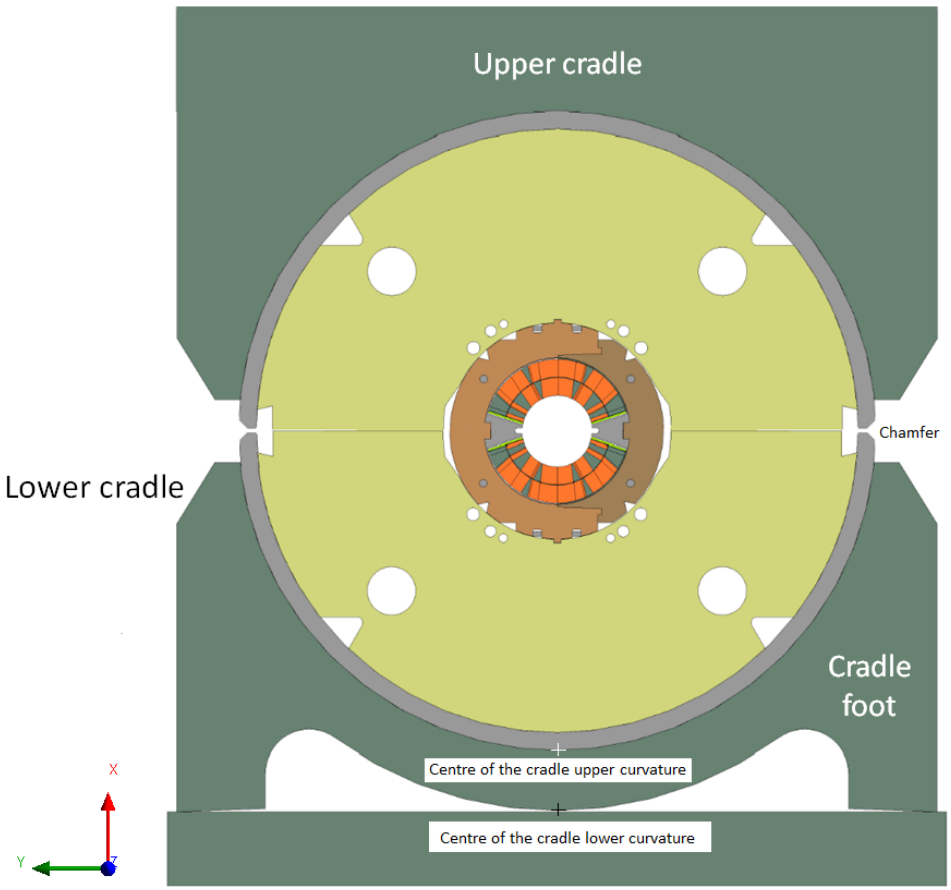

Figure 2.6: A Cradle assembly and single aperture 11-T dipole magnet (1-in-1) intersection. The magnet halves have been turned 90° clockwise from Figure 2.2 for the welding position. [26]

In order to ensure even contact between shell and yoke before welding, cradles are used to even out the geometric deviations from circular shape.

The cradle geometry was further developed from a previous cradle design, and it was redefined to meet the new requirements. The obsolete drawing of the press with the original cradles can be seen in Figure A.1 on the page 105 in the Appendix.

The 15 mm thick shell has a diameter of 540 mm. As seen in Figure A.3 on the page 107 in the Appendix, the diameter of the upper cradle is 1 mm smaller than the diameter of the shell. This feature ensures that the upper cradle has to open up around the magnet, simultaneously squeezing the shell against the yoke surface. This ensures contact between the yoke and the shell in the beginning of the pressing.

The lower cradle is 1 mm larger than the 15 mm thick shell, as seen in Figure A.4 on the page 108 in the Appendix. When the hydraulic cylinders of the press introduce load on the lower cradle and the centre of the cradle upper curvature hits first the shell (2.6), the lower cradle closes around the magnet assembly.

To enhance the closure, the lower cradle has a sloped cut at 2° from horizontal plane under the cradle feet, as seen in Figure A.4 on the page 108. For the 12 mm thick shell, the same cradles are used but the 3 mm gap has to be shimmed.

Tolerance of 1 mm in the rolled shell diameter is included in the mentioned cradle dimensions.

2.4 Press

Cradles are loaded by a short sample press seen in Figure 2.7. The short sample press consists of the main frame, cradles and hydraulic cylinders.

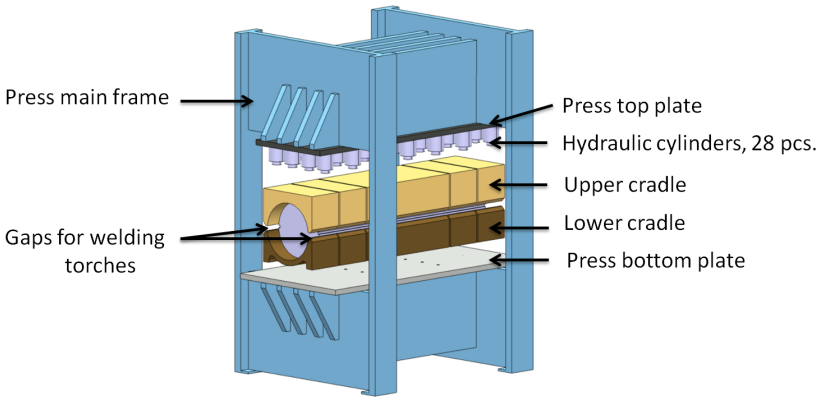

Figure 2.7: The skinning press with cradles. The upper cradles can be loaded by 28 hydraulic cylinders with the maximum achievable vertical load of 375 t/m. The openings for longitudinal welding can be seen on the sides of the cradles.

The magnet can be moved on its place by using a sledge. On the sledge, the magnet is placed inside the lower cradle. The hydraulic cylinders seen on the top plate push the upper cradle against the upper magnet shell. The magnet is supported on the lower cradle, which in turn is mounted on sledge on the press frame.

Pressure is then applied to the magnet assembly. After that the shell halves can be welded together through gaps seen between the cradles on both sides of the magnet (Figure 2.7). All dimensions of the cradles can be seen in Figure A.3 and Figure A.4.

The coils are compressed by the collared coils assembly. After that, the rest of the magnet is assembled around collared coils assembly. The magnet assembly is transferred to the press and mounted on the lower cradle on the press sledge.

2.5 Loads of the dipole magnet from assembly to operation

The magnet structure is subject to different load conditions from assembly to operation. They can be simplified into load steps as shown in Figure 2.8.

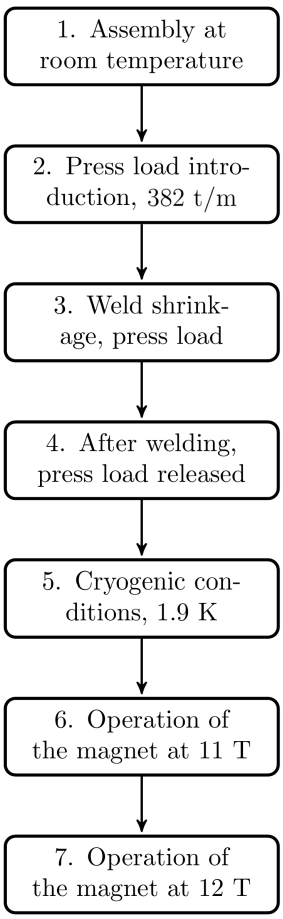

Figure 2.8: Loads of the dipole magnet from assembly to operation.

The upper cradle is mounted on top of the magnet assembly, shimming plates are added on top of the upper cradle and the assembly is moved inside the press on the sledge.

The assembly is pressed from the top with hydraulic cylinders. The magnet is uniformly loaded with the required press unit load, along the magnet length (in this analysis f_p = 382 t/m (3750 N/mm) was used). The shell welding operation is performed. The weld shrinks as the weld cools down. The magnet manufacture is then finalized and the magnet is transported to the site. Before operation, the magnet is cooled down to 1.9 K. During the operation 11 T field will be used, but the magnet has been designed to attain the nominal 12 T field.

2.6 Functional requirements of the magnet during assembly and welding of the magnet

The mechanical design of the magnet has to provide rigid clamping of the superconducting coil. [1]. It is essential to accomodate the coil with minimum distortion of the conductor positioning.

The intention is to pre-stress the magnet structure by using thermal shrinkage of the shell weld. The geometry of the yoke is described in detail in Figure 2.9. Thermal shrinkage compresses the yoke-yoke interfaces at the inner diameter of the yoke halves (gap bottom, Figure 2.2) due to geometry of the yoke half (the gap geometry can be seen in Figure 2.9). The yoke laminates act as a reserve of potential energy.

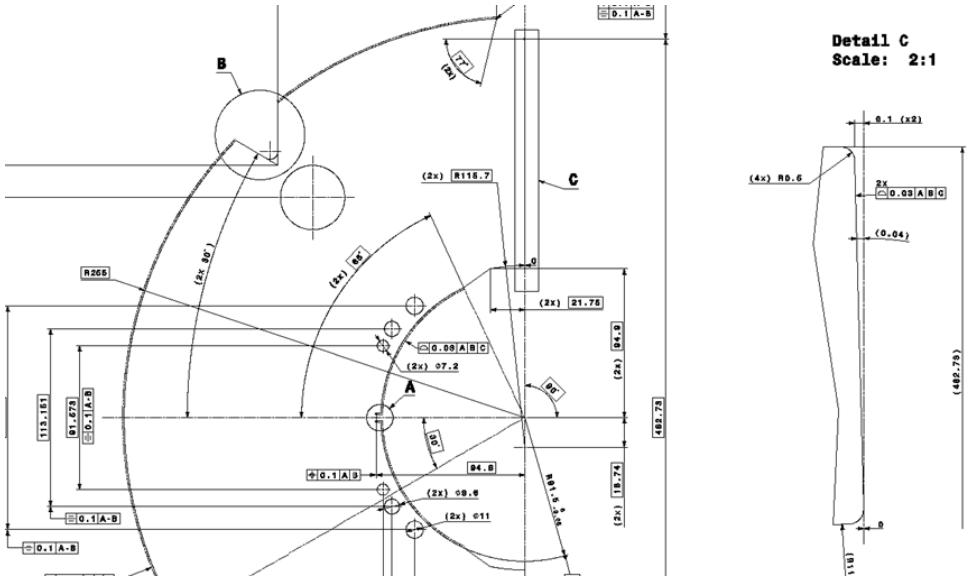

Figure 2.9: Part of the yoke drawings, showing the gap geometry. The drawing describes the left half of the yoke, but it has the same geometry than the right half of the yoke seen in Figure 2.2. In detail C it can be seen that the tapered gap of the yoke is 0 mm at the inner diameter of the yoke and 0.1 mm at the outer diameter of the yoke. [21]

Load cond.	Coil stress (MPa)	Shell stress, steel 316LN (MPa)
Room temp. 20 °C	$\sigma_{\mathrm{COA}} = 140$	$\sigma_{\mathrm{D}} = 160$
1.9 K	$\sigma_{\mathrm{COA}} = 140$	$\sigma_{\mathrm{SHA}} = \sigma_{\mathrm{P0.2}}$
1.9 K, 11 T	$\sigma_{\mathrm{COA}} = 140$	$\sigma_{\mathrm{SHA}} = \sigma_{\mathrm{P0.2}}$

Table 2.1: Functional requirements regarding the coil and shell stress. σ_D is the design level of the shell stress in room temperature based on analysis of the magnet group to maintain sufficient structural integrity of the magnet assembly during the operation of the magnet in 11 T magnetic field. [4] $\sigma_{\mathrm{P0.2}}$ is the elastic limit of the shell with offset strain of 0.2 %. For the steel 316LN $\sigma_{\mathrm{P0.2}} = 948.67$ MPa at 4.2 K, and the difference to the elastic limit at 1.9 K is negligible. [5] σ_{COA} is the allowable max stress of the coil defined by the Technology department. [4]

Pressing the magnet before and during welding is a method to produce a stable and rigid mechanical structure, keeping the coils in compression, even under high magnetic loads.

The stress level one is aiming at on the shell (after welding, in room temperature) is based on experience from previous magnet models. One is aiming at 160 MPa (σ_{D}, Table 2.1). It is sufficient to keep the gap bottom closed (as the yoke halves are in contact) and the shell stress remains below the allowable shell stress σ_{SHA} at any temperature (Table 2.1). Based on experience it was anticipated that the maximum shell pre-stress after welding can be 190 MPa. [23]

2.7 Functional requirements of the magnet structure during operation of the magnet

A quench is an abnormal termination of magnet operation that occurs when part of the superconducting coil enters the normal resistive state. This can occur when the coil warms above a critical temperature, bringing operations to an abrupt halt. In the case of a large superconducting magnet, which can be several meters long and carry currents of 10 kA and more, the quench creates a loud sound as the coolant (liquid helium, with a temperature close to absolute zero) turns into gas and vents through pressure relief valves. This can lead to destruction of the magnet. [38]

The Lorentz force is the force acting on a point charge q_e moving with velocity $\mathbf{v}$ in the presence of electric field $\mathbf{E}$ and magnetic field $\mathbf{B}$ [22]:

$$\mathbf{F} = q_e(\mathbf{E} + \mathbf{v} \times \mathbf{B}) \tag{2.1}$$

The units are defined as follows [q_e] = C = As = FV, [E] = N/C = V/m, [B] = T = Ns/Cm.

The Lorentz forces can cause micro-vibrations to the structure, which can produce frictional heating in the superconductor. This heating can impose quench in superconductor. If the magnet assembly has been pressed, the components have low clearance. The risk of getting additional movements of the structure due to the Lorenz forces during operation is minimized.

During powering, Lorentz forces act on the coil and need to be balanced by the magnet structure. Because of this, the structure is be pre-stressed before operation of the magnet. The yoke-yoke interface is closed after welding of the shell. When the magnet coil is cooled down, the closure of the yoke-yoke interface extends to outer corners of the yoke halves, and the mechanical excitation remains.

The applied mechanical excitation on the interface is released in operation and works as a counter-balancing force to Lorentz forces. The interface has to be kept closed after full power to ensure proper function of the magnet by keeping the structural clearances necessarily small. The closure of the yoke-yoke interface can be seen in Figure 2.10.

In detail, the gap at the bore (gap bottom, Figure 2.2) should remain closed within two digits in millimetres scale up to 12 T [1]. After this, "the gap closed" refers to this requirement. The poles should remain under compression at all times and maximum coil stress should remain under 140 MPa (σ_{COA},Table 2.1 on page 15) [1]. Functional requirements for the coil stress are given by the coil strength measurements done in laboratory conditions.

Nevertheless, static stresses should be maintained at an allowable level seen in Table 2.1. The allowable stress is the design level of stress for the coil and shell (σ_{COA}, coil allowable stress, and σ_{SHA}, shell allowable stress).

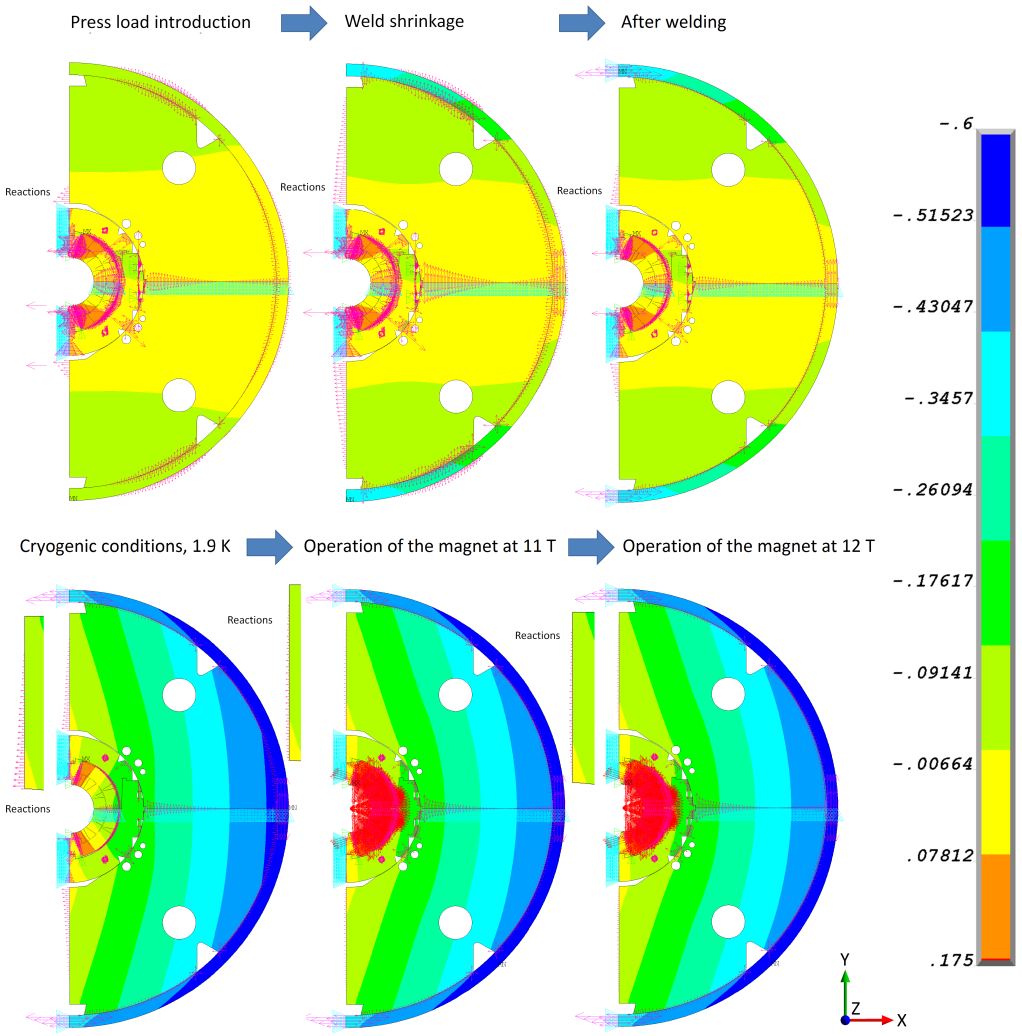

Figure 2.10: The displacement (unit: mm) plot in the x-axis direction of the frictionless model with a 15 mm thick shell for the load steps 2-7. The frictionless model is introduced in the chapter 3.3 on page 22). The load steps are introduced in the chapter 2.8 on page 13. The displacement is relative to the 1. load step. This demonstrates the closure of the yoke-yoke interface, and the displacement of the shell. The structure displaces into the negative x-axis direction. In the load steps 5, 6 and 7 it can be seen that the coil pushes back the yoke in the middle, but on the sides the gap closure holds. This can be seen from the reaction forces still present along the interface indicated by the red arrows. The displacement constraint on the shell weld was set to produce the 163 MPa on the "After welding" load step to produce these plots. The 163 MPa was chosen, since it is between the range of 115-190 MPa defined for the FEA of magnet with 15 mm shell.

3. THE PRE-STRESS OF A 1-IN-1 DIPOLE MAGNET SHELL AND SUPERCONDUCTING COIL

By the use of FEA it was verified that the coils are under compression during the pressing and welding of the magnet and that the coil stress doesn't exceed allowable limit.

It was further determined whether the thermal shrinkage of the welds between shell halves can be sufficient to close the yoke-yoke interfaces and keep them in this state during powering of the magnet to ensure rigid and stable structure of the magnet. The required theoretical weld shrinkage was determined and the pre-stress for the shell was computed. Shells of thicknesses 12 mm and 15 mm were compared.

The required weld shrinkage was determined in an iterative process with respect to the functional requirements in the chapter 2.7 on page 15 and 2.6 on page 14. The iterative process used is described with more detail in the chapter 3.5 on page 24.

3.1 Simplifications

The modelling task was simplified to save computation time:

- The FEA was performed based on 2D-plane stress model
- Symmetry around the vertical axis was used (Figure 2.2).
- Static structural analysis was seen sufficient, because the deformations of the magnet assembly and cradles are not large and the stick-slip effect between parts was seen negligible.

A 2D-plane stress model of the magnet was further developed [25]. The model is written in ANSYS parametric design language (APDL). It was decided that the new model will be based on the existing model of the magnet assembly. The model geometry has a thickness of 1 mm throughout the structure and utilizes 2D-solid elements explained later on page 21. In this model, many material parameters are linearly dependent on the temperature of the structure. The material properties can

be seen in Table A.1 on page 100 and in Table A.2 on page 101 in the Appendix.

It was thought that the symmetrical model based on the lower cradle and the magnet symmetry is sufficient to get accurate results. If the upper cradle doesn't compress enough laterally to close the gap tightly between it and the shell, the hydraulic cylinders pushing at the outer extremities of the shimming plate above the upper cradle seen in Figure 1.5 can be used to increase lateral compression to force gap closure (cylinders at the extremities mean the cylinders of the circuits A, C and E, their location being described later in the chapter 4.2 on page 44).

Geometry and constraints

The model is more representative in the case of the 15 mm thick shell, since the size of the cradle equals the one used in reality.

For the 12 mm thick shell, the cradle diameter was reduced in the model as well as the width of the cradle at extremities. Width at the extremity was 640 mm for the 12 mm shell and 644 mm for the 15 mm shell.

In reality the same upper and lower cradles are used for both magnet assemblies, the smaller one with the 12 mm shell requiring additional shimming for the 3 mm gap, however that was not modelled. The cradle bottom plate is modelled as a 250 mm thick plate, but in reality the press has the cradle bottom plate and the press bottom plate to support the lower cradle.

The shell geometry is modelled to be perfectly circular, as well as the yoke. The assumption is taken that the shell is in even contact with the yoke.

The sloped cut in the weld seam of the shell wasn't modelled as in Figure 2.6 but was left straight like in Figure 2.2. The exact geometry is to be defined later from the knowledge gained by previous and oncoming welding tests to reach the maximum shrinkage with the currently used welding technologies. A summary of the welding test can be seen in the document: Plane welding tests, longitudinal welding of the shrinking cylinder [3].

The geometry and elements of the magnet and press are additionally symmetric about the central line, with one exception: the overlapping three layers of collar elements are only symmetric about the x-axis. A zero-displacement constraint in the orientation of the y-axis was applied to the nodes at the central line for all symmetrical parts. A zero-displacement constraint in the orientation of the x-axis was given to the collar and coil nodes at the symmetry line.

Contact surfaces were modelled for all separate parts. The wedges and conductors of the coil sections were modelled to be fully integral.

The magnet half was modelled to rest in a stationary position against the over-constrained fixed wall (Figure 3.1, Figure 3.2. This wall represents the yoke-yoke

interface, where the gap is located.

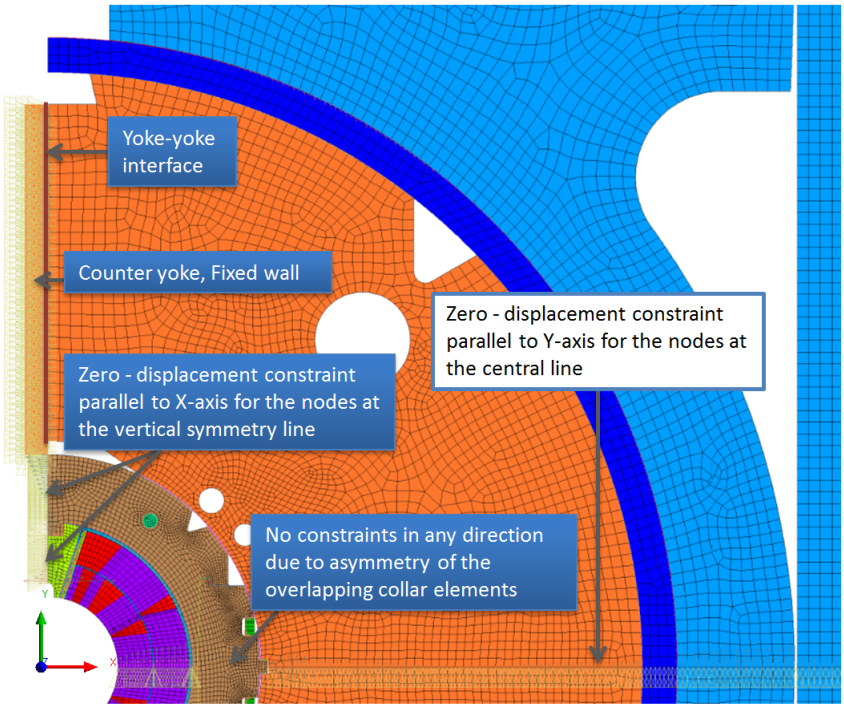

Figure 3.1: Boundary conditions. Left: As indicated the fixed region of the counter-yoke and the constrained nodes of the collared coil assembly. Below: As indicated the constrained nodes at the central line. [26]

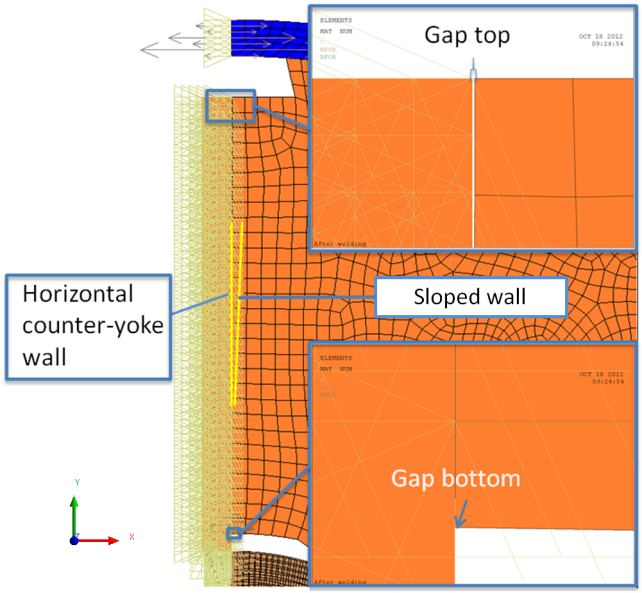

Figure 3.2: The gap geometry. The yellow lines have been exaggerated to represent underlying wall geometries. [26]

3.2 The element types of the magnet and cradle model

The element used for the 2D-domains is Plane183 seen in Figure 3.3. PLANE183 is a quadratic 2-D, 8-node or 6-node element. For the analysis 8-nodes were used. Thickness of the plane can be included in the element options, making it 2-D solid element. In the model the thickness was set to 1 mm everywhere, except to overlapping collar plates, where the thickness was set to 0.5 mm.

The element used for the contact surfaces is CONTA172 seen in Figure 3.4. CONTA172 is used to represent contact and sliding between 2-D "target" surfaces and a deformable surface, defined by this element.

The element used for the target surfaces is TARGE169 seen in Figure 3.5. TARGE-169 is used to represent various 2-D "target" surfaces for the associated contact elements. The contact elements themselves overlay the solid elements describing the boundary of a deformable body and are potentially in contact with the target surface, defined by TARGE169. [40]

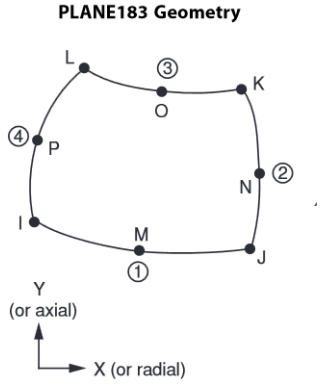

Figure 3.3: The PLANE183 2-D-solid element was used for all domains. [40]

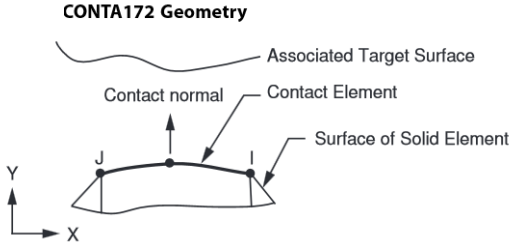

Figure 3.4: The CONTA172 element was used for contact surfaces. [40]

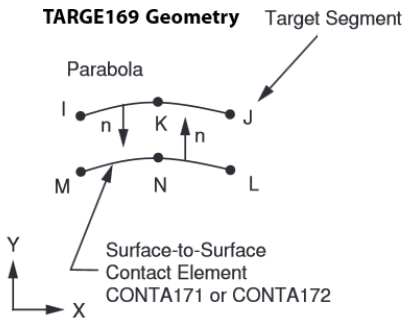

Figure 3.5: The TARGE169 element was used for target surfaces. [40]

3.3 Friction

In order to get an estimation of friction between shell and yoke two approaches were compared:

- Introducing a frictionless and bonded contact in ANSYS [39]
- Bonding the nodes over a 90° on the shell and yoke contact surface (Figure 3.6)

Presented results are based on the frictionless and bonded contact approach. Implementation of friction would require the implementation of further load steps for realistic static to kinematic friction transition. The fact that the model is static, practically also limits one to examination of static friction effects. In reality, dynamical friction would be present as stick-slip effect. Contact elements were used between all parts in the assembly.

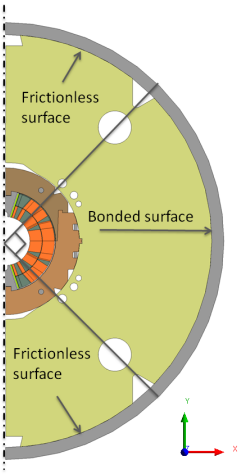

Figure 3.6: The bonded and frictionless surfaces. The bonded contact angle is 90°. It was thought that the shell sticks on this area due to strong frictional contact. [26]

3.4 The element quality of the magnet and cradle model

The dependency of the results on the number of elements was not checked excluding the shell elements, because the magnet model was already used for analysis in the magnet group.

One wanted to get the peak von-Mises stress for the weld of the shell, where the peak stress of the shell is located in the inner corner of the shell weld on the yoke side (the location to pick shell stress results is shown in Figure 3.7.

Normally peak stress results on the extremities or corners of the geometry are strongly dependent on the element size chosen. It was seen that reducing the element size from 5 mm to 4.5 mm decreased shell max stress in the final load step by 10 %. After that, reducing the element size didn't have any remarkable effect on the results, but instead the time consumed for computation increased by a factor of 5. Because one had to complete numerous iterations to reach the goal of the FEA, the 4.5 mm element size of the shell was chosen.

For the cradle and the cradle bottom plate the element size of 5.0 mm was seen sufficient, as one was not interested to pick any results from them. The insulation layers and collaring shoe had only one element layer in the thickness direction, as seen in Figure 3.8.

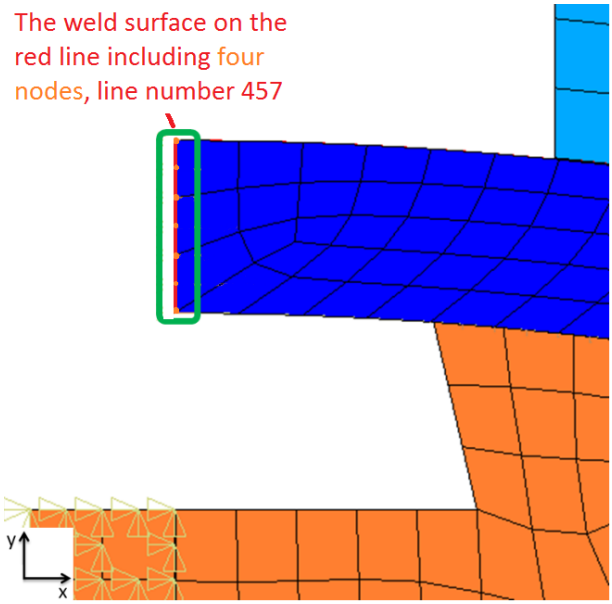

Figure 3.7: The location of the nodes to look for the shell pre-stress results (von-Mises). An average and maximum von-Mises stress were computed from the weld surface encircled. [26]

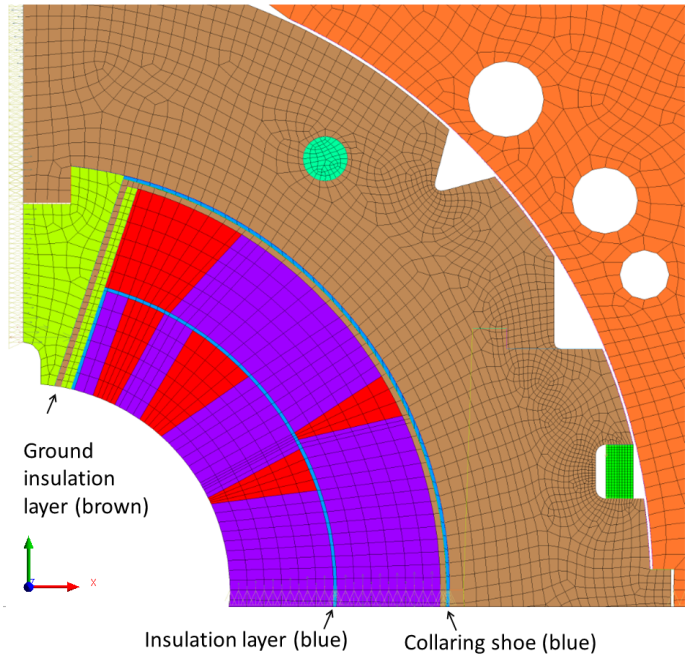

Figure 3.8: The mesh of the collared coil showing the thin element layers. The elements of the inner insulation layer and collaring shoe are blue and the elements of the ground insulation layer are brown. [26]

In the available time, it was not possible to evaluate the effect of the number or size of these elements to overal results. It was seen that the elements of the insulation layers were mostly under compression. The thin elements of the insultion layers were not seen to have a big impact on the results, because shear between the insulation layer and collar contact surfaces or coil section contact surfaces was seen negligible.

3.5 Load steps

The initial geometry for the magnet before any load steps is given as each part would rest on their place without interference of any contact surfaces.

3.6 Assembly and loading

Assembly at RT

The first load step seen in Figure 3.9 is actually assembling the magnet in the collaring press. The load step imposes interferences of the contact surfaces between the collared coil assembly and yoke. The required interferences of the coil and collar are achieved, causing the coil max von-Mises stress to reach 74.6 MPa.

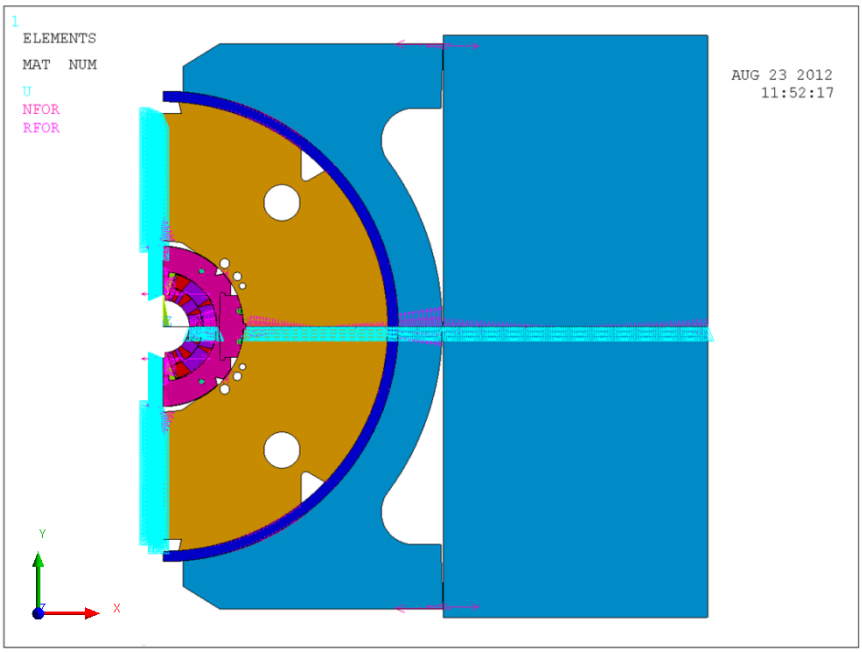

Figure 3.9: Collared coil assembly at RT [26]

In the model the mechanical loads are provided by applying the interference on the contact elements. As seen in Figure 3.10, shimming is used in various locations. In the model, interference of contact and target elements simulates shimming and is realized by the use of ANSYS CONTA172 element real constant FTOLN.

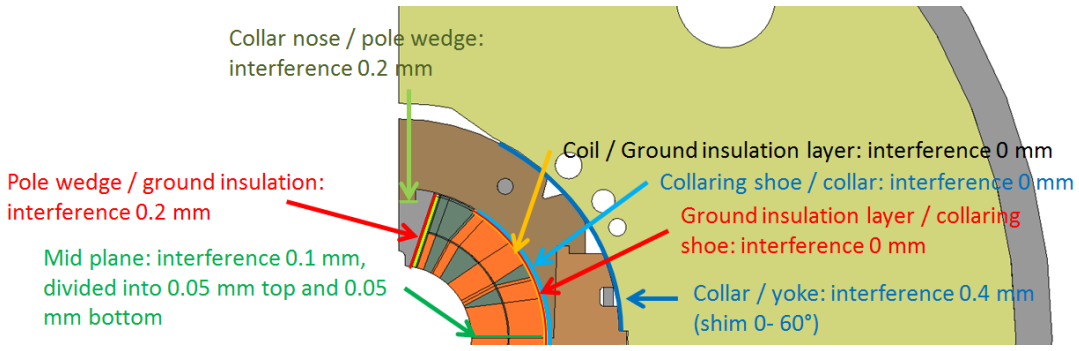

Figure 3.10: Shimming in the first load step is realized by the imposed interference of target and contact surfaces. Interference is applied by the parameter FTOLN. [26]

> "FTOLN is a factor based on the thickness of the element which specifies an allowable maximum penetration for the augmented Lagrangian method. If ANSYS detects any penetration larger than this tolerance, the global solution is still considered unconverged, even though the residual forces and displacement increments have met convergence criteria." [42]

Press load introduction 382 t/m

The magnet is uniformly loaded with the press unit load, $f_p = 382$ t/m (3750 N/mm) along the magnet length, or z-axis defined in Figure 3.11. The load to the magnet should come only through the feet of the cradle. It was verified that with the desired geometry and load, centre of the cradle lower curvature can't get in contact with the loading plate. The cradle feet are staying in contact with the loading plate all the time during the load step.

The shell is originally resting on its place on the yoke, fixed in the y-axis direction, but free to move in the x-axis direction. The cradle is dropped into the contact with the shell toward the negative x-axis direction. The cradle (with larger diameter than the shell) touches the shell at the centre of the cradle upper curvature initially. During the load step iterations, as the load gradually rises to the defined load, the closed contact surface gradually increases up to the sides of the cradle.

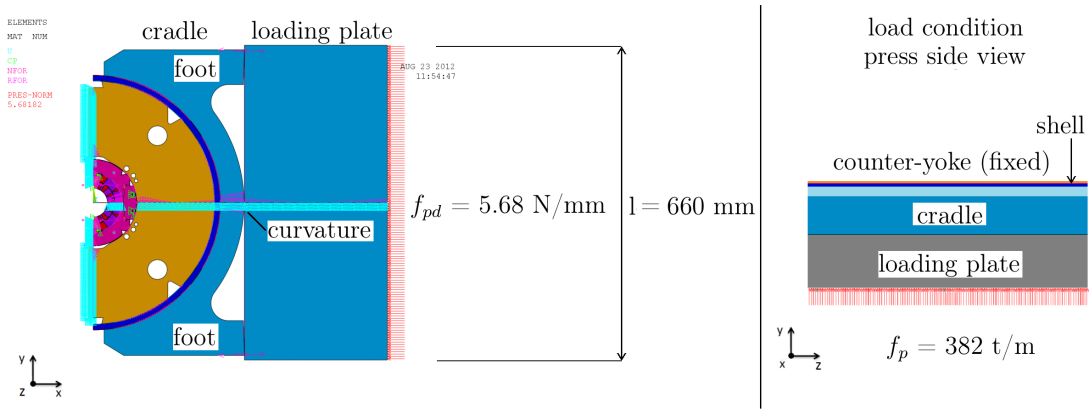

Figure 3.11: Press load introduction. The press unit load f_p is applied to the model intersection (the 2-D solid elements of the intersection defined 1 mm thick). The uniformly distributed press load f_{pd} indicated by the red arrows along the 660 mm wide loading plate equals then 5.68 N/mm in the y-axis direction. [26]

3.7 Welding sequence

Weld shrinkage

The weld shrinkage is implemented in the model as a surface load f_w into negative x-axis direction as indicated in Figure 3.12.

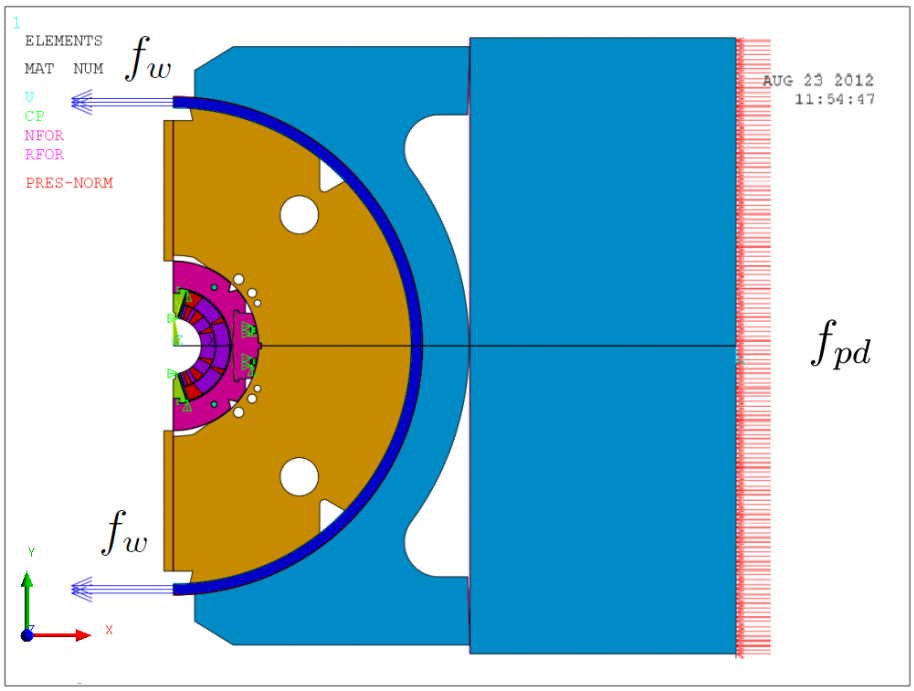

Figure 3.12: Weld shrinkage [26]

The weld surface load f_w and the corresponding average displacement of the weld nodes u_{av} in negative x-axis direction is iteratively adjusted to produce the shell pre-stress $\sigma_{avg,4} = 190$ MPa (in the negative x-axis direction) on the "After welding" load step. The weld nodes are at the location to pick the shell pre-stress results, and can be seen in Figure 3.7.

The aim is to get the resulting stresses for the cases "The maximum shrinkage one possibly can possibly achieve with $\sigma_{av} = 190$ MPa" for the both shell thicknesses. The minimum displacement constraint for the both shell thicknesses can be found by ensuring that the gap bottom stays closed at all times within two digits in mm-scale. That defines the "The minimum shrinkage required to keep the gap closed after welding". The shrinkages u_{av} can be seen in Tables 3.1 and 3.2.

The load f_w turned slightly the weld surface (line nr 457, Figure 3.7 on page 23) around z-axis in the 3rd load step due to uniform load on the shell geometry. The node displacement on the shell outer diameter displaced at maximum only 0.04 mm more than the node on the shell inner diameter in all cases, so the effect of this on any computations can be seen negligible.

Case	Surf. load f_w (MPa)	Shrinkage u_{av} (mm)
Frictionless, $\sigma_{avg,4}$ = 190 MPa	175	0.46
Bonded, $\sigma_{avg,4}$ = 190 MPa	175	0.34
Frictionless, $\sigma_{avg,4}$ = 138 MPa	120	0.33
Bonded, $\sigma_{avg,4}$ = 140 MPa	120	0.26

Table 3.1: Applied weld loads of 12 the mm shell in negative x-axis direction. The weld surface was loaded by f_w in the 3rd load step and displacement constrained in the load steps 4-6 by u_{av}. The surface load f_w equals to average azimuthal stress on the weld in the 3rd load step, $\sigma_{avg,3}$.

Case	Surf. load f_w (MPa)	Shrinkage u_{av} (mm)
Frictionless, $\sigma_{avg,4}$ = 188 $\approx$ 190 MPa	175	0.47
Bonded, $\sigma_{avg,4}$ = 189 $\approx$ 190 MPa	175	0.35
Frictionless, $\sigma_{avg,4}$ = 116 MPa	100	0.28
Bonded, $\sigma_{avg,4}$ = 115 MPa	95	0.23

Table 3.2: Applied weld loads of 15 the mm shell in negative x-axis direction. The weld surface was loaded by f_w in the 3rd load step and displacement constrained in the load steps 4-6 by u_{av}. The surface load f_w equals to average azimuthal stress on the weld in the 3rd load step, $\sigma_{avg,3}$.

After welding

The resulting average nodal displacement u_{av} caused by the surface load f_w from the "Weld shrinkage" load step is applied as nodal displacement constraint for the weld to negative x-axis direction (seen in Figure 3.13) from the "After welding" load step onwards. The location of the displacement constrained nodes is same as the location to pick the shell pre-stress results seen in Figure 3.7 on page 23. The press load f_p is set to zero. The reaction forces to calculate stress $\sigma_{avg,4}$ were exctracted with the following APDL-commands for the load steps 4-6:

LSEL,S,LINE,,457 (select the weld surface line nr 457, Figure 3.7 on page 23)
NSLL,S,1 (select nodes on that line)
NSEL,R,EXT (select nodes on the exterior of the elements)
*DIM,shFYSm,,1,1 (define a one-cell table to save the results)
*GET,shFYSm(1),FSUM,0,ITEM,FX (exctract the sum of the x-component forces)
*SET,shFYSm(1),shFYSm(1) (set a value to the one-cell table)

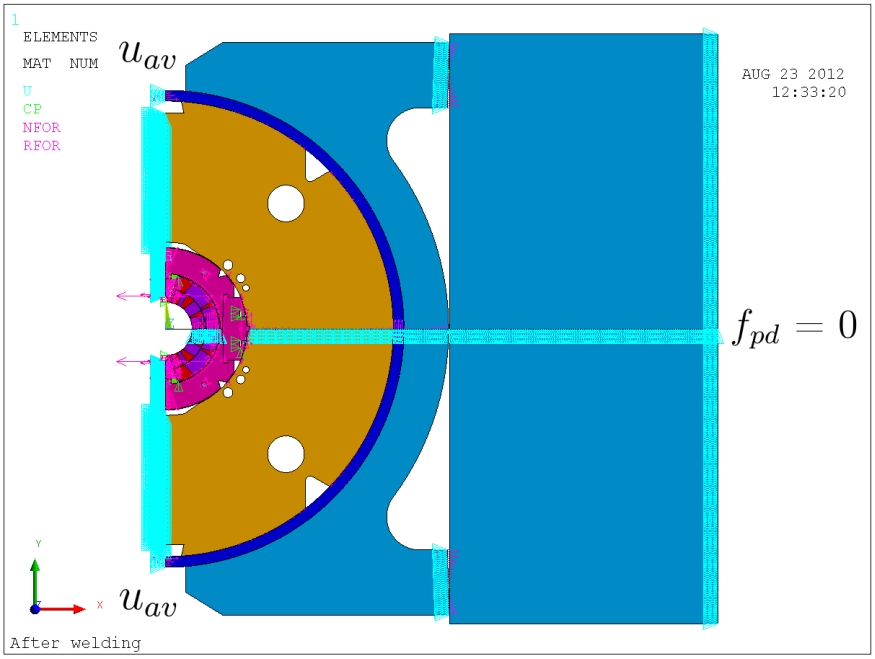

Figure 3.13: After welding. [26]

3.8 Cryogenic conditions, 1.9 K

In the load step the structure is cooled down to 1.9 K. An uniform temperature load T = 1.9 K is applied to the whole structure. In the model the cradle feet and the press plate are fixed and the remaining closed contact disappears due to thermal shrinkage of the cradle and shell. In reality the magnet has already been transferred and assembled to the cryostat independently, and the cradles remain at the press.

3.9 Operation of the magnet

The Lorentz-forces of the 11.22 T and 12 T magnet field are applied to the coil in these load steps. These nodal forces are transferred from an electromagnetic simulation of the coil to the mechanical model.

All load steps of the model and the iterative processes to compute the weld shrinkages are shown in Figure 3.14.

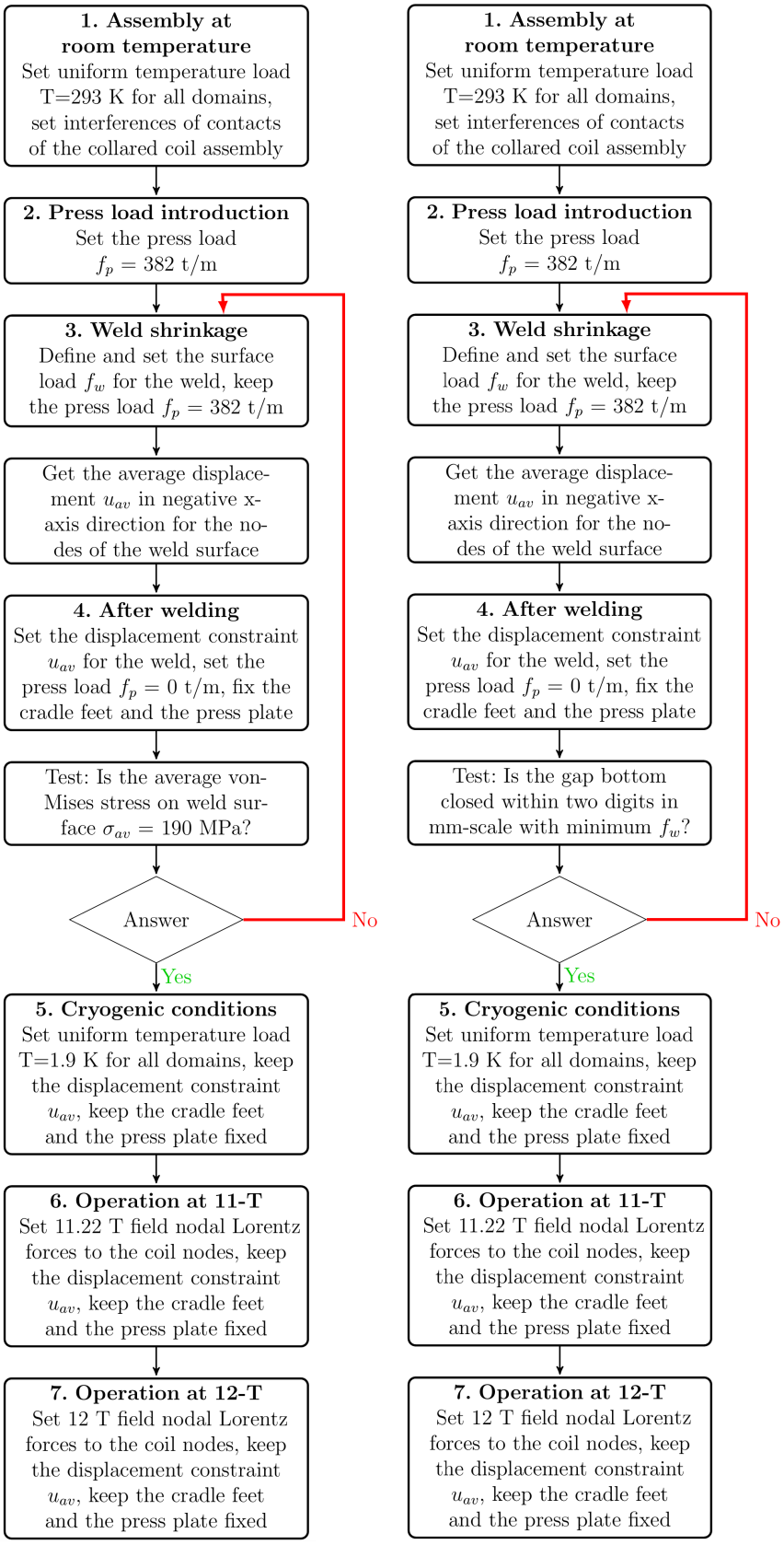

Figure 3.14: The iterative computation of the weld shrinkage. The computation was completed for 12 mm and 15 mm shells. After computation the final von-Mises stress results of the shell and coil can be exctracted for each load step. On the left the iterative process to get the "Maximum shrinkage that one can possibly achieve" and on the right the process to get the "Minimum shrinkage required to keep the gap closed after welding" explained on page 26. [26]

3.10 The results

The coil stress

The results of the pre-stress in the coil conductors were extracted from the yellow coil conductor mesh area seen in Figure 3.15. The maximum von-Mises stress was picked from the area. The location of the max stress on the area varied due to the different loading conditions in each load step.

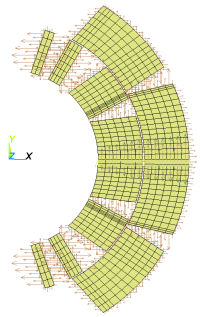

Figure 3.15: The max nodal coil stress results were extracted from the yellow coil conductor mesh area in the picture. The red arrows indicate reaction forces. [26]

Figure 3.16 and Figure 3.17 plot the coil maximum stress. From the results it can be noted that till 11 T for the 12 mm or the 15 mm shell, the stress stagnates between 113-120 MPa regardless of the bonded or frictionless case.

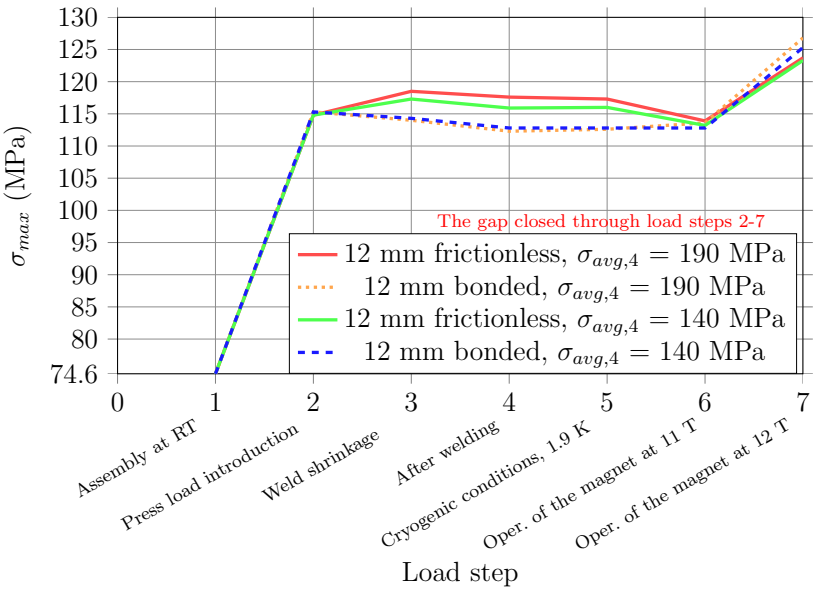

Figure 3.16: The maximum von-Mises coil stress on the dipole with a 12 mm thick shell. The shrinkages u_{av} can be seen in Table 3.1.

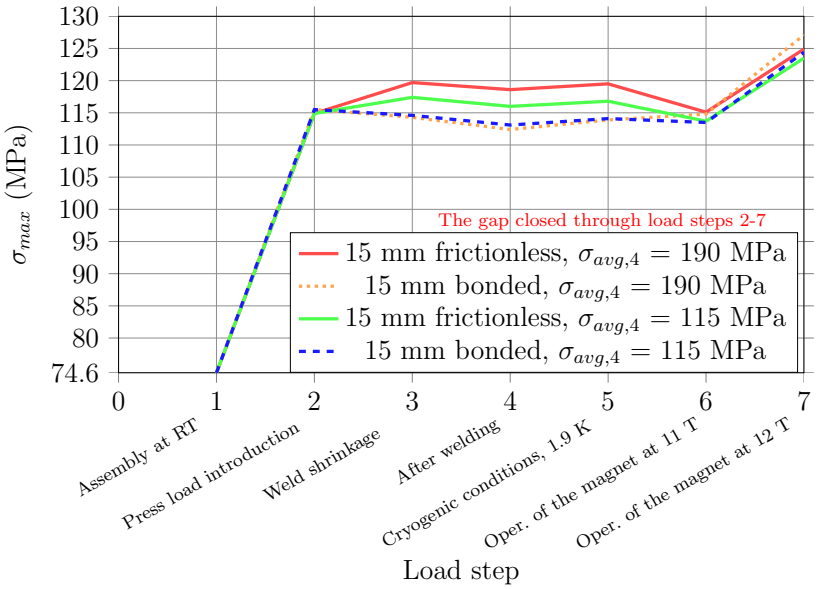

Figure 3.17: The maximum von-Mises coil stress on the dipole with a 15 mm thick shell. The shrinkages u_{av} can be seen in Table 3.2.

At 12 T, the stress rises up to 128 MPa, still well below the $\sigma_{\mathrm{COA}} = 140$ MPa. The plot of the coil stress can be seen in Figure 3.18.

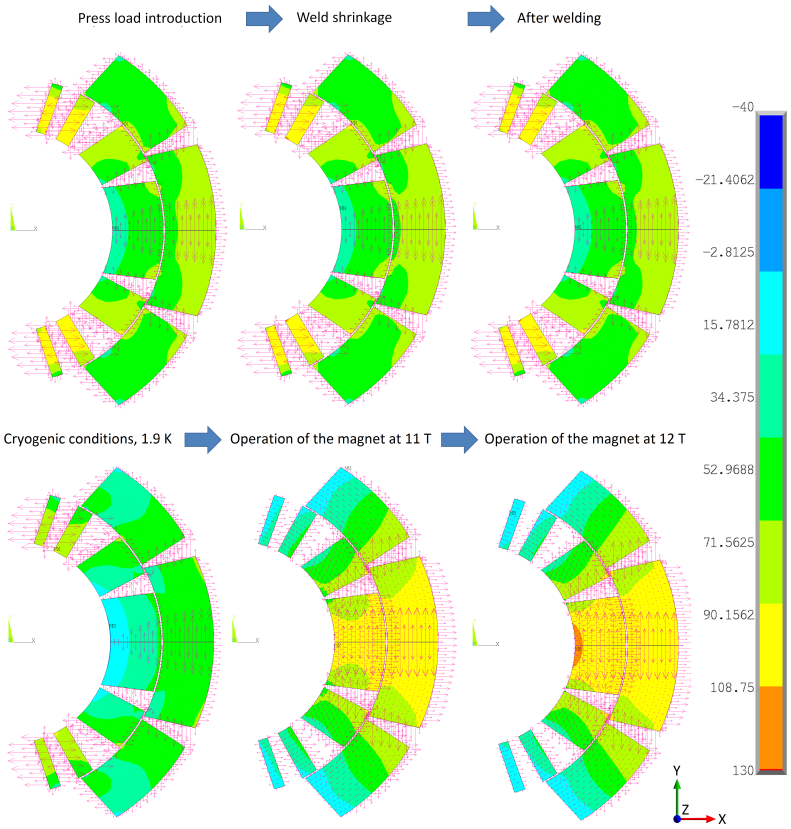

Figure 3.18: The von-Mises coil stress (unit: MPa) plot of the frictionless model (described in the chapter 3.3 on page 22) with a 12 mm thick shell for the load steps 2-7. The red arrows indicate reactions on the nodes.

The shell stress

The result of the pre-stress of the shell was calculated as averaged total nodal force in the negative x-axis direction on the weld divided by the thickness of the shell. The location of the nodes can be seen in Figure 3.7 on page 23 The results of average shell pre-stress can be seen in Figure 3.19 and 3.20. The results of maximum shell pre-stress can be seen in Figure 3.21 and 3.21.

Gap bottom was closed at all times in load steps 2-7 and 190 MPa was the aim for the maximum in the "After welding" load step. For the dipole with the 12 mm thick shell, during the cool down and powering, the stress rises up to around 375 MPa. The minimum stress required to close the gap rises up to around 310 MPa. For the dipole with the 15 mm thick shell, during the cool down and powering, the stress rises up to around 370 MPa. The minimum stress required to close the gap rises up to around 275 MPa. Shortly; the minimum stress to keep the gap closed decreases if the shell is thicker.

The displacement sequence in the direction parallel to x-axis for the load steps 2-7 is shown in Figure 2.10 for 15 mm thick shell. The Von-Mises stress plots of

the frictionless and bonded models for the load steps 2-7 of the magnet with 12 mm thick shell can be seen in Figures 3.23 and 3.24

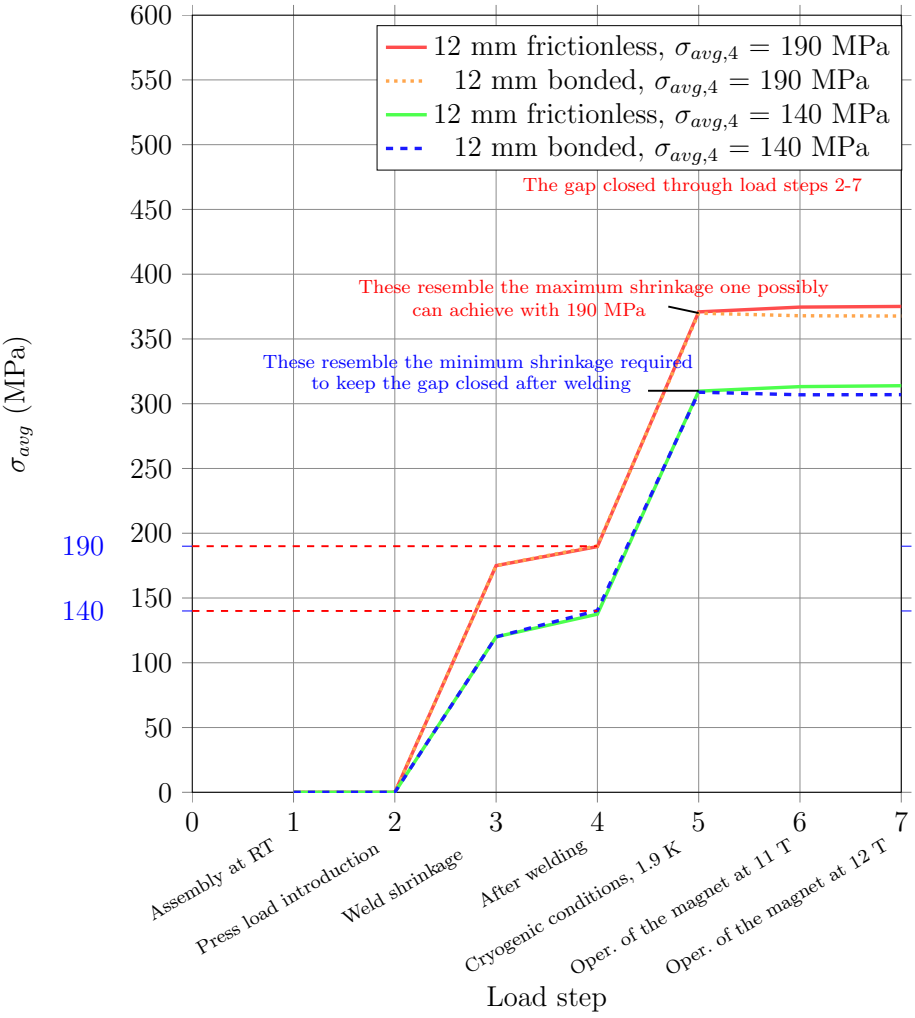

.

Figure 3.19: The average azimuthal weld pre-stress on the 12 mm thick shell. The weld shrinkages can be seen in Table 3.3.

Case	Surf. load f_w (MPa)	Shrinkage u_{av} (mm)
Frictionless, $\sigma_{avg,4}$ = 190 MPa	175	0.46
Bonded, $\sigma_{avg,4}$ = 190 MPa	175	0.34
Frictionless, $\sigma_{avg,4}$ = 138 MPa	120	0.33
Bonded, $\sigma_{avg,4}$ = 140 MPa	120	0.26

Table 3.3: Applied weld loads of 12 the mm shell in negative x-axis direction. The weld surface was loaded by f_w in the 3rd load step and displacement constrained in the load steps 4-6 by u_{av}.

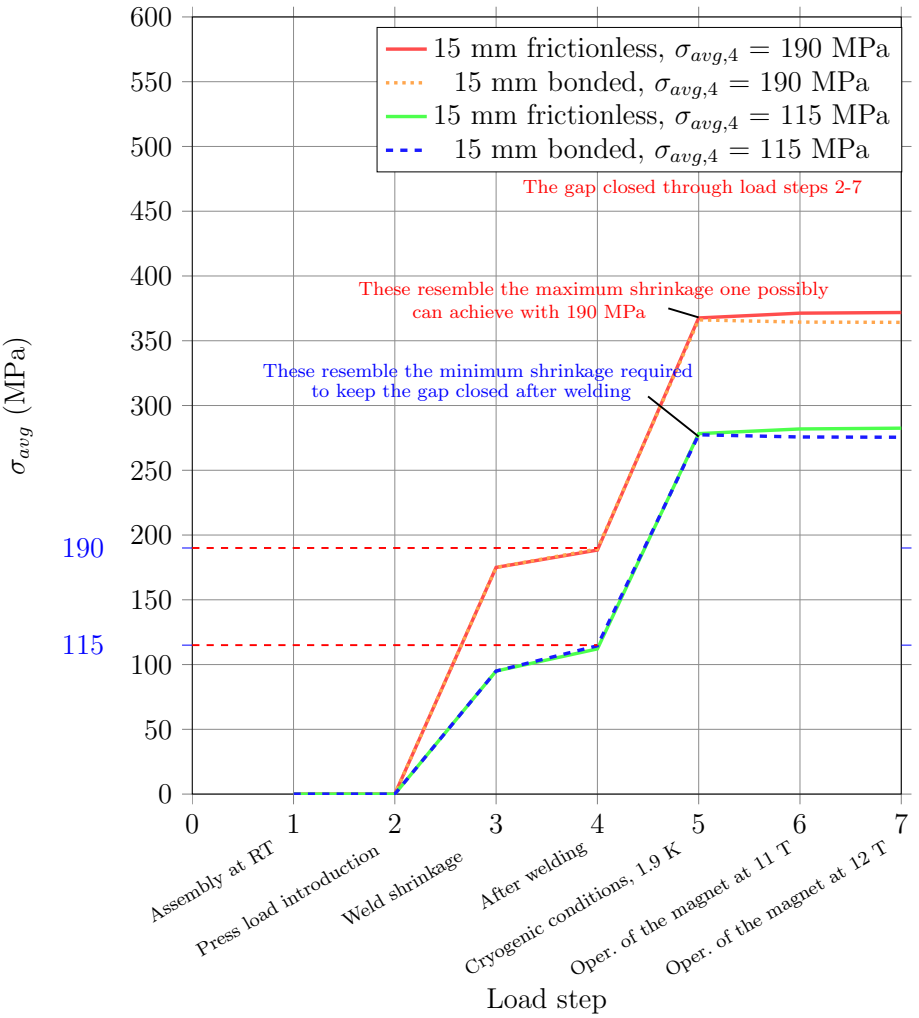

Figure 3.20: The average azimuthal weld pre-stress on the 15 mm thick shell. The weld shrinkages can be seen in Table 3.4.

Case	Surf. load f_w (MPa)	Shrinkage u_{av} (mm)
Frictionless, $\sigma_{avg,4} = 188 \approx 190$ MPa	175	0.47
Bonded, $\sigma_{avg,4} = 189 \approx 190$ MPa	175	0.35
Frictionless, $\sigma_{avg,4} = 116$ MPa	100	0.28
Bonded, $\sigma_{avg,4} = 115$ MPa	95	0.23

Table 3.4: Applied weld loads of 15 the mm shell in negative x-axis direction.The weld surface was loaded by f_w in the 3rd load step and displacement constrained in the load steps 4-6 by u_{av}.

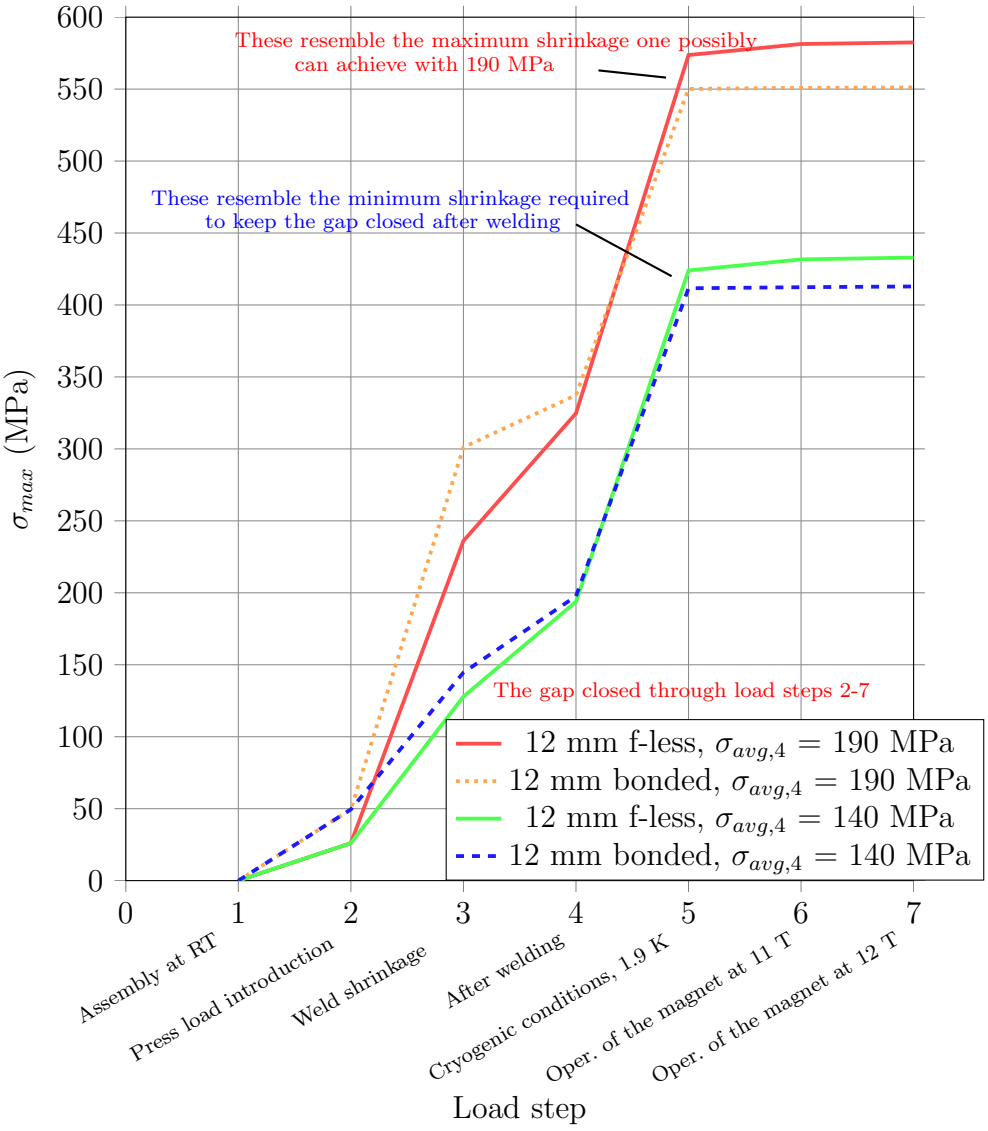

Figure 3.21: The maximum azimuthal weld pre-stress on the 12 mm thick shell. The weld shrinkages can be seen in Table 3.3.

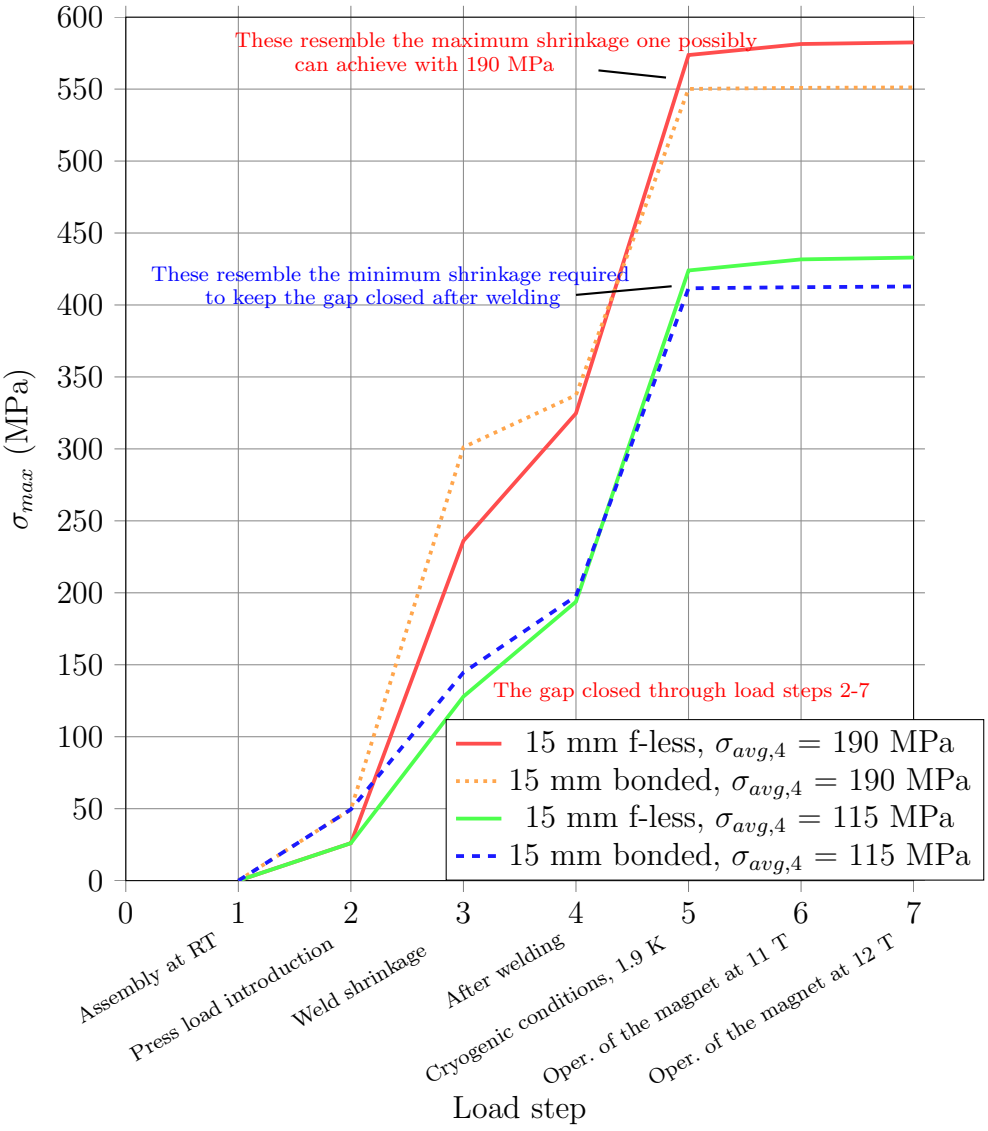

Figure 3.22: The maximum azimuthal weld pre-stress on the 15 mm thick shell. The weld shrinkages can be seen in Table 3.4.

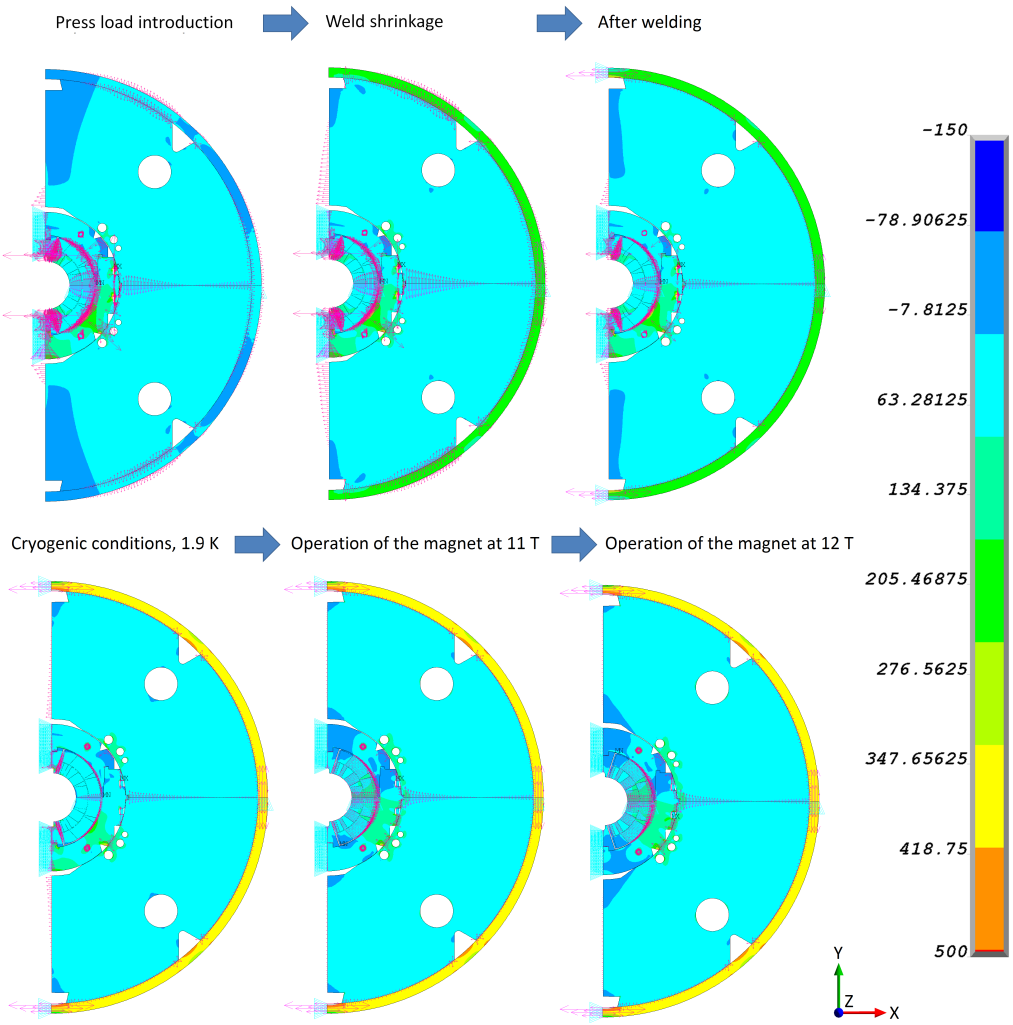

Figure 3.23: The von-Mises stress (unit: MPa) plots of the frictionless model (described in the chapter 3.3 on page 22) for the load steps 2-7 of the magnet with 12 mm thick shell. The displacement constraint u_{av} was set to produce the 190 MPa on the "After welding" load step to produce these results.

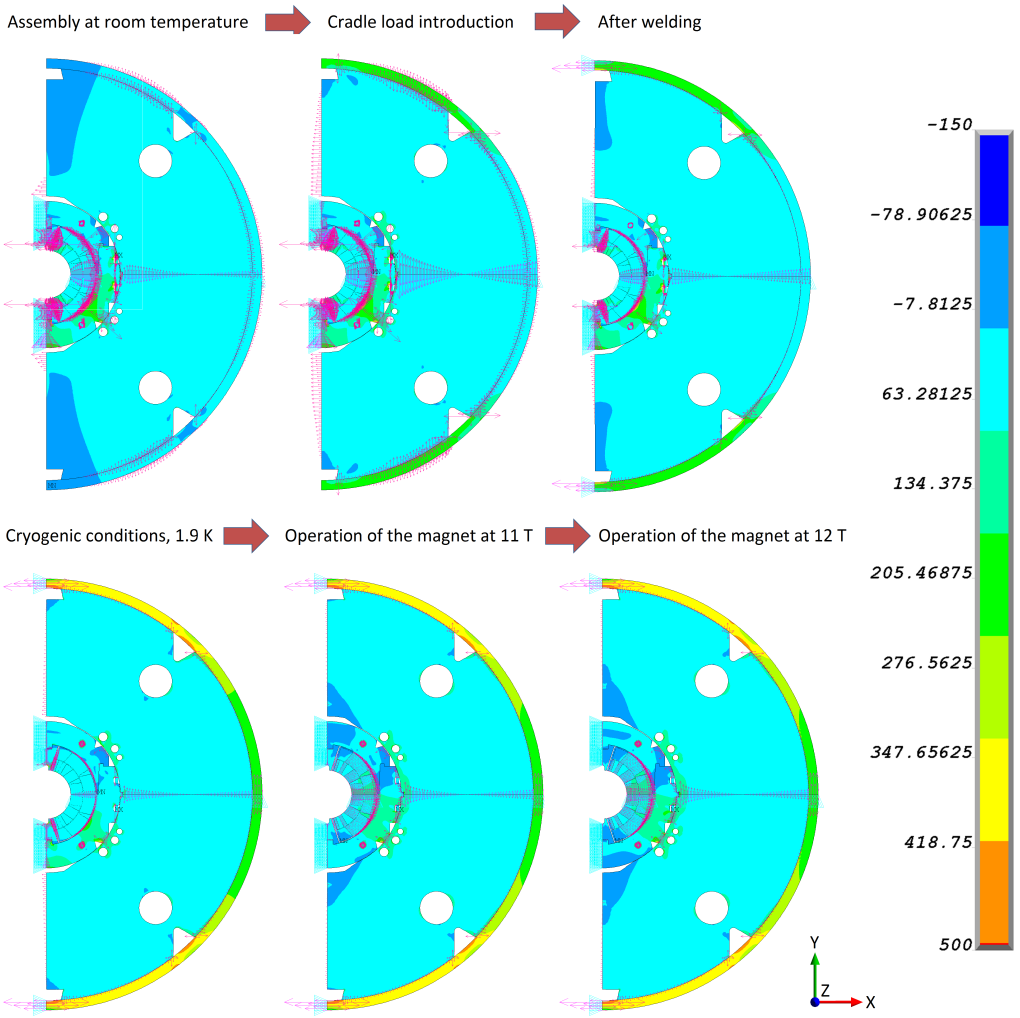

Figure 3.24: The von-Mises stress (unit: MPa) plots of the bonded model (described in the chapter 3.3 on page 22) for the load steps 2-7 of the magnet with 12 mm thick shell. The displacement constraint u_{av} was set to produce the 190 MPa on the "After welding" load step to produce these results.

The gap behaviour

Results of the gap displacement were taken from the locations in Figure 3.2 shown at the extreme nodes. The gap is closed within two decimals in the mm-scale after the first load step. The gap top length for 12 mm shell can be seen in Table 3.5 and for the gap bottom in Table 3.6. The gap length was calculated from the displacement component parallel to x-axis.

Case	F-less 190	Bon. 190	F-less 140	Bon. 140
Load step	mm	mm	mm	mm
Assembly at RT	0.200000	0.200000	0.200000	0.200000
Press load introduction	0.029579	0.032731	0.029579	0.032731
Welding shrinkage	0.023869	0.00086	0.007758	0.003262
After welding	0.003119	0.005505	0.041892	0.02099
Cryogenic conditions, 1.9 K	0.000056	0.000535	0.005601	0.001687
Oper. of the magnet at 11 T	0.000008	-0.000004	0.000598	0.000066
Oper. of the magnet at 12 T	0.000139	-0.000006	0.000305	-0.000001

Table 3.5: The gap top length for the 12 mm shell. The initial yoke geometry before collaring press has the top gap of 0.1 mm at the outer diameter of the yoke (see drawing 2.9 in the Appendix).

Case	F-less 190	Bon. 190	F-less 140	Bon. 140
Load step	mm	mm	mm	mm
Assembly at RT	0.100000	0.100000	0.100000	0.100000
Press load introduction	0.000045	0.000048	0.000045	0.000048
Welding shrinkage	0.000047	0.0000300	0.000044	0.000031
After welding	0.000052	0.000025	0.000053	0.000033
Cryogenic conditions, 1.9 K	0.000056	0.00004	0.000052	0.00004
Oper. of the magnet at 11 T	-0.000001	-0.001914	-0.000512	-0.003099
Oper. of the magnet at 12 T	-0.000844	-0.005413	-0.002825	-0.007469

Table 3.6: The gap bottom lenght for the 12 mm shell. The initial yoke geometry before collaring press has the bottom gap of 0.0 mm at the inner diameter of the yoke (see drawing 2.9 in the Appendix).

3.11 Conclusions

Due to manufacturing issues the real shell is not perfectly round. Since the shape and frictional behaviour of the surfaces is not known, the model was kept simple. This implies that, with the model, one cannot get exact results for the behaviour of the gap, shell stress and coil stress. To say something solid, one can only approximate the lower and upper boundaries of the result variables for the shell, when the bottom gap stays always closed and the estimated maximum available pre-stress after welding (190 MPa) is not exceeded.

One can think that the bonded case resembles the minimum, and that the frictionless resembles the maximum in terms of required shrinkage. During the loading of the cradle, the shell wall to be welded can displace due to variation of the shell radius. This has to be taken in account when defining the geometry of the chamfer. If not well tested and considered, the weld can become too thin in some cases and the thermal shrinkage of the weld is too short to pre-stress the shell. Should that

be the case, the shell remains too loose.

Theoretically one can say that the shrinkage has to be at least approximately 0.27-0.33 mm to close the yoke gap. At the moment of writing this report, and since there are still unknown parameters, computations done with the model may be futile. By taking in account the non-uniform contact between the yoke assemly and the shell and between the shell and the cradles, one may even have a reason to estimate the need of 0.6-0.8 mm shrinkage in reality. To be on the safe side, one must find the right geometry of the wall to be welded by trial and error. Also the welding parameters have to be considered.

As the average shell stress goes high in the last three load steps, it can be seen that the maximum azimuthal stress at the weld stays well below the $\sigma_{\mathrm{P0.2}} = 948.67$ MPa (steel 316LN). It can be seen that the use of 15 mm shell is a way to reduce the required minimum pre-stress on the shell weld to close the gap. On average, the minimum stress rises up to level of 310 MPa for a 12 mm thick shell and 280 MPa for a 15 mm thick shell.

Using the model one can get the maximum theoretical coil stress. However, the coil stress stagnates and stays in all cases and load steps well below the $\sigma_{\mathrm{COA}} = 140$ MPa. It means that one is still in safe area for the design with respect to the coil stress.

There are welding experiments coming with real magnets in the end of the year. The results and the accuracy of the model can be compared with measured results later.

4. THE WELDING PRESS

The hydraulic welding press was originally designed for the welding of short LHC main magnet models. The press had been earlier stored in bldg. nr. 927 and then moved to bldg. 180 to be modified for the needs of the 11-T quadrupole and dipole magnet project. It was planned to modify it to be used for the welding of short prototype magnets using a new cradle approach described in the previous chapter.

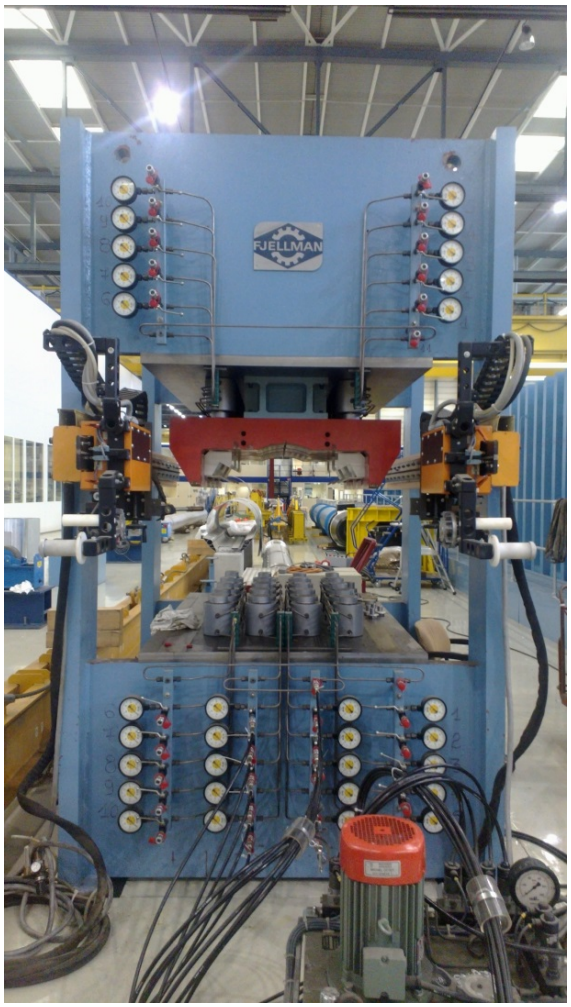

Figure 4.1: The unmodified press in August 2012. The welding robots can be still seen on the girders. They were removed and the press will get new robots after validation in 2013. Also the press includes the old manometers six hydraulic circuits including five cylinders each.

The press assembly was produced by Fjellman Press AB in 1992 in Mariestad, Sweden, and it's equipment was changed in 2013 after price quotations from five companies in France and Switzerland. This upgrade includes a new hydraulic concept and interface. The author had specified the requirements of the hydraulic system after discussions with LMF-section. The hydraulic system was then designed by Aldiance Linatec-Dimat at Cluses in France. The interface was specified and designed by the author and LMF-section; the software for the control was written by Aldiance Linatec-Dimat. Furthermore the modification includes a new loading - unloading concept and a reinforced main frame which were mostly realized at CERN internally. The fabrication of the new cradles of the press were outsourced to Bulgaria. The unmodified press can be seen in Figure 4.1.

4.1 Press specification

The press was designed to be capable of flattening 12-15 mm thick and 2,5 m long shells against the yoke. It has to have a flexible loading concept to enable LMF-section to adapt to various types of magnet assemblies in the future. The new specifications can be seen in Table 4.1. The old 79 ton NIKE hydraulic cylinders were taken from the old version of the press and reused in the new version. Only 28 out of the total of 30 were needed and the worst two cylinders were selected away.

It is to be determined how much force one would need for the welding of the magnet. The old press frame was specified at 850 tons maximum so the maximum load of the press was not limited by the cylinders. Having 2168 mm total shell length the 1-1 dipole magnet is the longest of the prototype magnets. By 850 tons this length can be covered by 392 ton/m along the longitudinal axis.

On the contrary, the larger welding press at LMF-section for 15 m long dipole magnets has the nominal load of 400 ton/m. However, the load on the shells should not be uniform. The sufficient shrinkage can be achieved with less force at the longitudinal extremities of the shells, and the rest of the force can be transferred to the center of the magnet. This leads to the requirement of sectorization of the hydraulic system described in the next chapter. The right division of the load between extremities and center of the shells has to be determined later at LMF-section based on experience. In any case, by transforming the load to the center of the magnet, the press is able to attain almost the nominal load of the larger press. Additionally, lateral degree of freedom was specified to be even more flexible with the welding.

Property	Value	Unit
Nominal load of the frame	850	ton
Nominal load of a single cylinder	79	ton
Nominal pressure of a cylinder	700	bar
Amount of cylinders	28	-
Amount of circuits	6	-

Table 4.1: The main properties of the press.

4.2 Hydraulic sectorization

The original location of the cylinders on the base plate can be seen in Figure 4.1 on page 42 and in Figure A.2 on page 106 in the Appendix. In the upgrade, the cylinders were relocated to the top plate as seen in Figure 4.3, and reconfigured to six circuits operating in five sections according to Figure 4.2. These five sections allow the use of five cradles pairs (top and bottom cradles). Having two circuits for one section enables lateral degree of freedom to adapt the cradle more flexibly to different loading cases.

The cradles A-D have different length - maximum cylinder force ratio than the circuits E and F. Therefore the maximum capability of each circuit operating at 700 bar is defined as in Table 4.2.

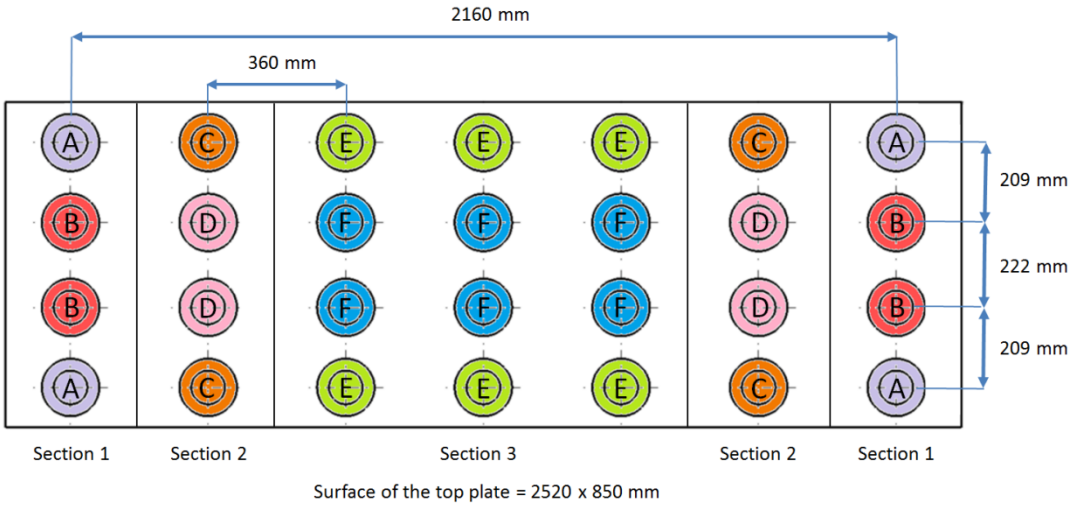

Figure 4.2: The sections of the press. The press has been divided into 5 sections, the four sections indicated as Section 1 and Section 2 are similar, and the press is symmetric along the longitudinal axis. The six hydraulic circuits use nomenclature A-F.

Nominal Loads	Load/unit length	Length	Load on section	Load of each cyl.
Location	ton/m	m	ton	ton
Circuit A (1x4)	458	2x0,345=0,69	316,02	79
Circuit B (1x4)	458	2x0,345=0,69	316,02	79
Section 1 (2x4)	916	2x0,345=0,69	2x316,02=632,04	79
Circuit C (1x4)	458	2x0,345=0,69	158	79
Circuit D (1x4)	458	2x0,345=0,69	158	79
Section 2 (2x4)	916	2x0,345=0,69	2x316,02=632,04	79
Circuit E (1x6)	445	1,065	473,92	79
Circuit F (1x6)	445	1,065	473,92	79
Section 3 (2x6)	890	1,065	2x473,92=947.85	79

Table 4.2: The nominal loads of the sections, circuits and cylinders.

4.3 Improvements on the press main frame

The press table was lengthened to 2.5 m by changing extended base plate for the cylinders (top plate) and for the sledge (bottom plate). The extensions were bolted to the frame and 16 triangular reinforcements below them were welded to the extensions and the main frame. The base plate and the top plate were machined. oindent A girder was fixed next to the press in vertical direction in order to allow the attachment of the hydraulic hoses as seen in Figure 4.3. On the top plate the pipes were located to the sides of the press.

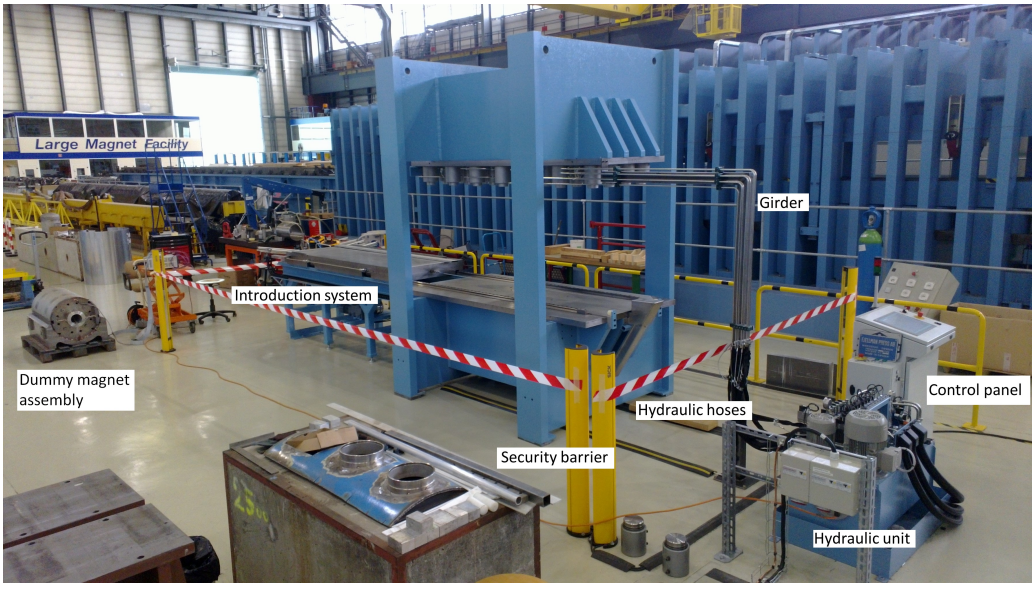

Figure 4.3: The improved press on 16.8.2013. The dummy 11-T 1-in-1 short magnet model is resting on the cradle. The magnet introduction system, press, security barrier can be seen. The control panel, and the hydraulic unit are on the right. The hydraulic pipes and hoses can be seen attached to the support girder between the hydraulic unit and the cylinders.

Moreover, a table for the introduction of the magnet was constructed. It consists of a motor, wire and pulleys to move a sledge on rails carrying a magnet on it. The sledge itself can be lifted up by four 5 ton cylinders. During the welding the sledge rests on its base plate.

4.4 Safety of the press

Safety functions of the press were realized in many ways. The following three main safety functions will automatically stop the pumps and shuts down the pressure after their conditions have been met. The software also informs the user by error messages.

- The original press frame has the nominal load of 850 ton. This total load was enabled by the software, because it was necessary to run the press on its nominal load in order to verify its functionality in a long duration test (duration 15 h) as a part of the factory acceptance test. Exceeding the total load limit releases the pressure in the cylinders.

- The hardware limits the load of each cylinder to 79 ton. This is realized by safety relief valves, which are set to release the over pressure after the nominal pressure of 700 bar has been overpassed.

- During the magnet introduction and ramping up of the hydraulic pressure in the cylinders, the access to the press side is forbidden. A security circuit system capable to observe whether a person or a limb is inside the press frame has been installed. The system uses light barriers which are located around the press frame. For any detection of movements inside the controlled area and within the explained window of time the system

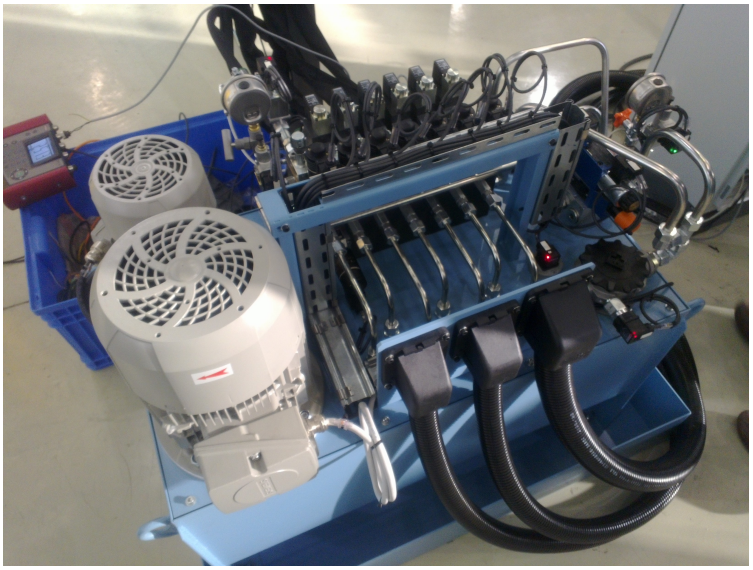

Figure 4.4: The hydraulic unit of the press.

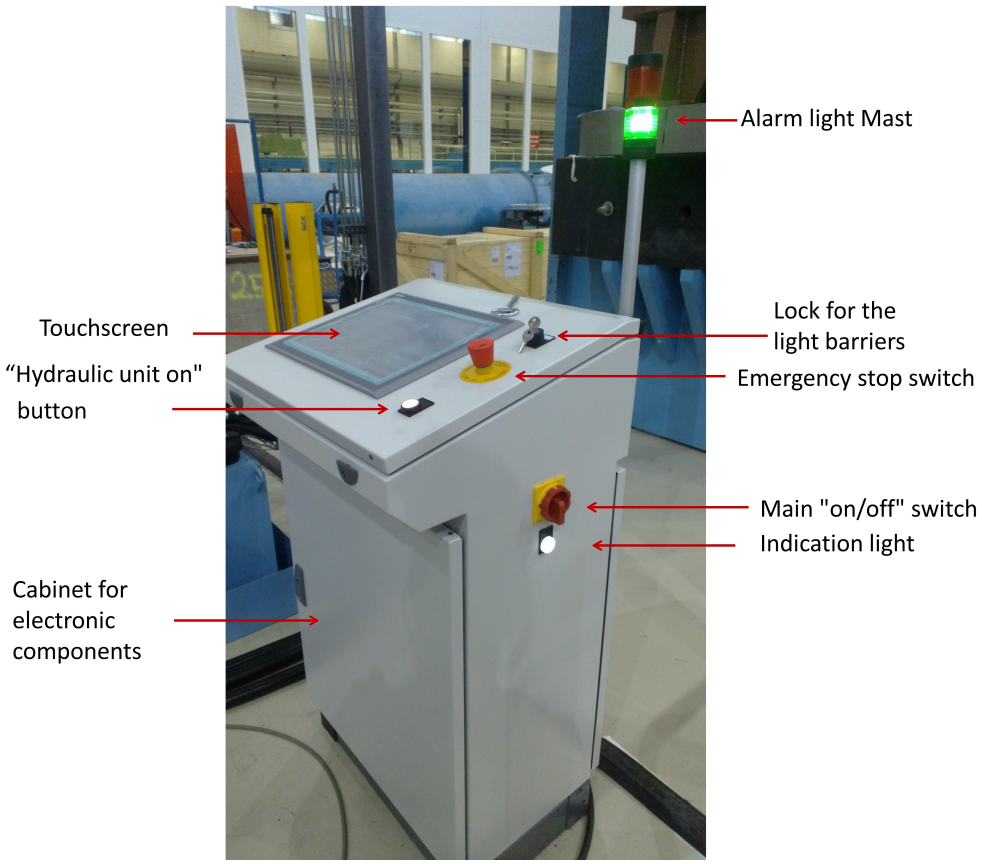

Figure 4.5: The control panel of the press. The main "on/off" switch is located on the right side of the panel with the white indication light. On the top, the lock for the light barriers can be seen with emergency stop and "hydraulic unit on" button below it. The white button also has a white light indication. The mast has a red alarm light for errors and a green light to distinguish between manual and auto-modes.

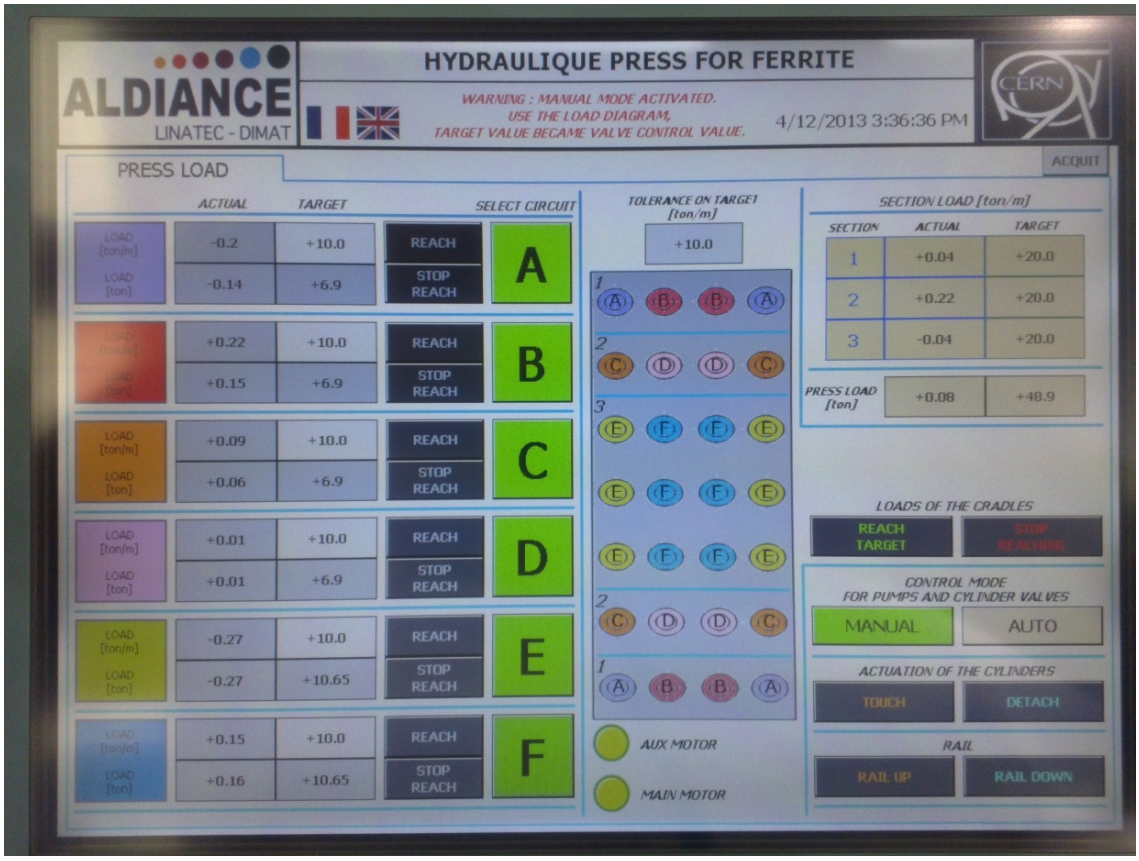

Figure 4.6: The graphical user interface of the press

4.5 User interface

The graphical user interface (GUI) of the press was realized on the touchscreen on the user control panel seen in Figure 4.5. It has command buttons and input cells to define the pressing operation to be done, and outputs to have visual control over the current load status of the press. The GUI can be seen in Figure 4.6. The different functions of the interface have been explained in the Table 4.3 and Table 4.4 on pages 49 and 50.

4.6 Control mode for pumps and cylinder valves

The press has two modes of operation, the manual and auto-modes. The manual mode has been implemented to use the press in more redundant way, in case the PID-control circuits of the press have problems.

4.7 Manual mode of the press

PID-control circuit is bypassed in manual mode. Target load is a parameter to control the actual load level given by the sensors. The actual load level is based on a

nonlinear load diagram for this parameter. The pressure sensor data has no effect on electromagnetic valves. Therefore, no feed-back loop exists between the valve and sensor in each circuit. Target value has to be understood as a parameter for load and a user has to use a load diagram that has been provided to reach target loads that fulfills requirements.

In the manual mode the pump is running continuously. Since there is no active control of pressures, pressures are not maintained at the same level as minor leaking in the pistons decreases pressure levels constantly.

4.8 Automatic mode of the press

In the auto-mode each circuit reaches target load values set by the operator (set-point) and the feedback control attempts to maintain the load levels within given general tolerance value. Sensors are used to monitor actual pressure levels in circuits, and PID-control unit controls electromagnetic valves. When testing the press, it was very difficult to reach the target load without overshooting too much in auto-mode. The problem is that the control parameters vary much between the start, when the pressure is very low and the desired level.

Button/input cell	Description	Unit
Control mode		
Manual mode	Manual control mode of the press	
Auto-mode	Automatic control mode of the press	
Table		
Table up (1x4)	Raise the rail up	
Table down (1x4)	Lower the rail down	
Loads of cradles		
Reach target	Reach the target load with all active circuits	
Stop reaching	Stop reaching the Target load with all active circuits	
Touch	Lower the cylinders of active circuits down	
Detach	Raise all cylinders up	
Press load		
Select circuit A - F	Activate circuits.	
Reach	Reach the target load with the selected individual circuit	
Stop reaching	Stop reaching the Target load with all active circuits	
Target (Load)	The target load of the individual circuit in Auto-mode	ton/m
Other		
Tolerance on target	The tolerance of all circuit loads for Auto-mode	ton/m
Acquit	Quit error messages on the message line	
Flag of GB/France	Changes the language between english and french	

Table 4.3: The command buttons and input cells of the GUI.

Therefore, an additional procedure to set up a high enough pressure level in manual mode first was established. Auto-mode cannot be used until each of the selected circuits has 5 ton/m or more actual load in manual mode. This load can be attained by using at least 50 ton/m target values for the control variable. After that auto-mode can be accessed. In auto-mode the pump is not running continuously, and the pump is stopped if the actual load differ less from target value than the current tolerance value. If this condition is fulfilled at least 20 s, the pump will be stopped.

Output cell	Description	Unit
Press load		
Target (Load)	Target total load of the cylinders in the circuit	ton
Actual (Load)	Actual total load of the cylinders in the circuit	ton
Actual (Load)	Actual circuit load per unit length along the length of the magnet	ton/m
Section load		ton/m
Section	Number of the section	
Target	Target load of section	ton/m
Actual	Actual load of section	ton/m
Press load		ton
Target	Reach the target load with all active circuits	ton
Actual	Stop reaching the Target load with all active circuits	ton
Other		
Text msg. line	Text messages of press functions and errors	
Aux motor	Light green colour - motor on, dark green colour - motor off	
Main motor	Light green colour - motor on, dark green colour - motor off	

Table 4.4: The output cells of the GUI.

5. HEAT TRANSFER OF A SUPERCONDUCTIVE NB_3SN DIPOLE MAGNET COIL IN AN INERT GAS FURNACE

5.1 Furnace at the building 927

The heat treatment of the Nb_3Sn coils require a gas tight reaction furnace. A simplified side profile of the main functional entities can be seen in Figure 5.1.

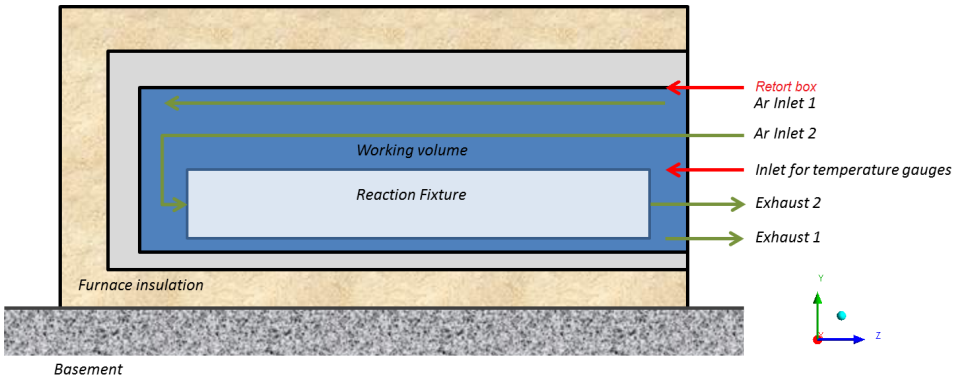

Figure 5.1: Simplified side profile of the furnace. The main functional entities can be seen.

This 2.5 m long furnace is is currently used at CERN for the short sample development program. It is the precursor of the larger furnace that will be extended to the length of 6.5 m for the full-scale 11 T-dipole magnet prototype program. The main design parameters are described in Table 5.1. The drawings of the furnace can be seen in Figures A.5, A.6 and A.7 on pages 109-110 in the Appendix.

In Figure 5.1 a reaction fixture is placed inside the retort box. This fixture can be described as a mould in which the Nb_3Sn coil is mounted during the reaction treatment. Hence, the main assembly of the reaction fixture consists of the Nb_3Sn coil and its insulating material as well as heat resistant stainless steel.

The blue working volume seen in the picture is located inside the retort box. There are two gas circuits that allow purging of the working volume and the reaction fixture.The inlet circuits allow sufficient pre-heating of the inert gas during the entire duration of the heat treatment. An overview of the equipment can be seen in Figure 5.2.

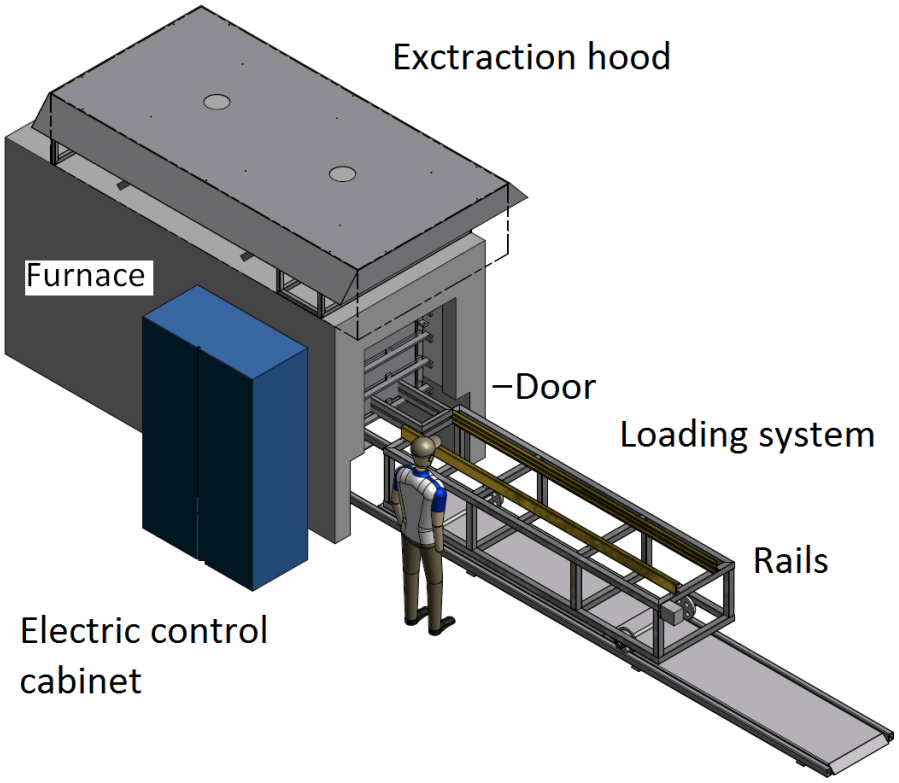

Figure 5.2: An overview of the furnace. The furnace has an loading system in front including rails and a sledge to move the fixture inside the furnace.

Parameter	Value	Unit
Working volume and installation area		
Length	6.5	m
Min. cross-section (W x H)	0.6 x 0.5	m^2
Max installation area (chariot, electrical cabinet and control box)	2 x 7.5 m	ton/m
Loads		
Max. linear load (metallic fixture and coil)	700	kg/m
Max. operation temperature	900	°C
Heating rate	20-150	°C/h
Max. allowable cooling rate	45	°C/h
Temperature stability	-5/+3	°C
Temperature uniformity	+/-3	°C

Table 5.1: The main dimension and parameters characterising the furnace.[6]

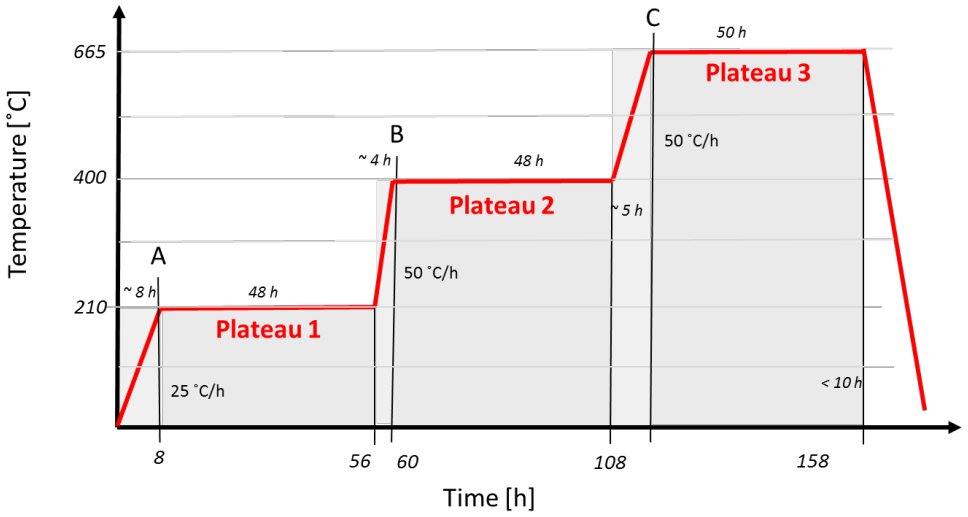

Figure 5.3: The specified plateaus of the coil reaction treatment.

The heat cycle including specified plateaus of the treatment as well as the ramp loads can be seen in Figure 5.3.

A half-cut overview can be seen in Figure 5.4. It shows how the retort is located inside the furnace. The location of the heating elements can be seen placed all along the side walls of the furnace. A more detailed half-cut overview that reveals the location of the cooling fan can be seen in Figure 5.5.

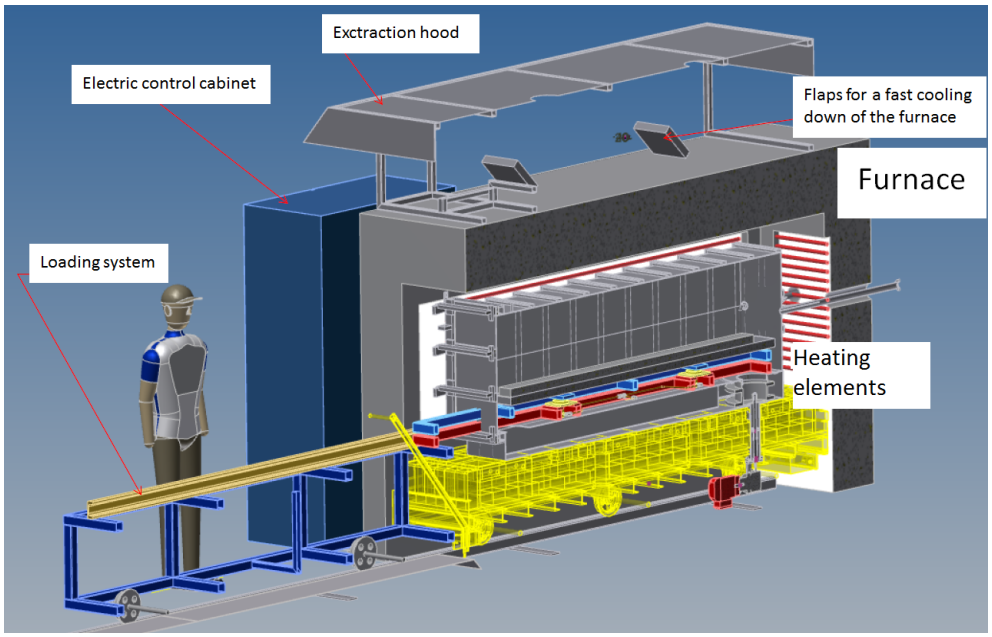

Figure 5.4: A half-cut overview of the furnace equipment.

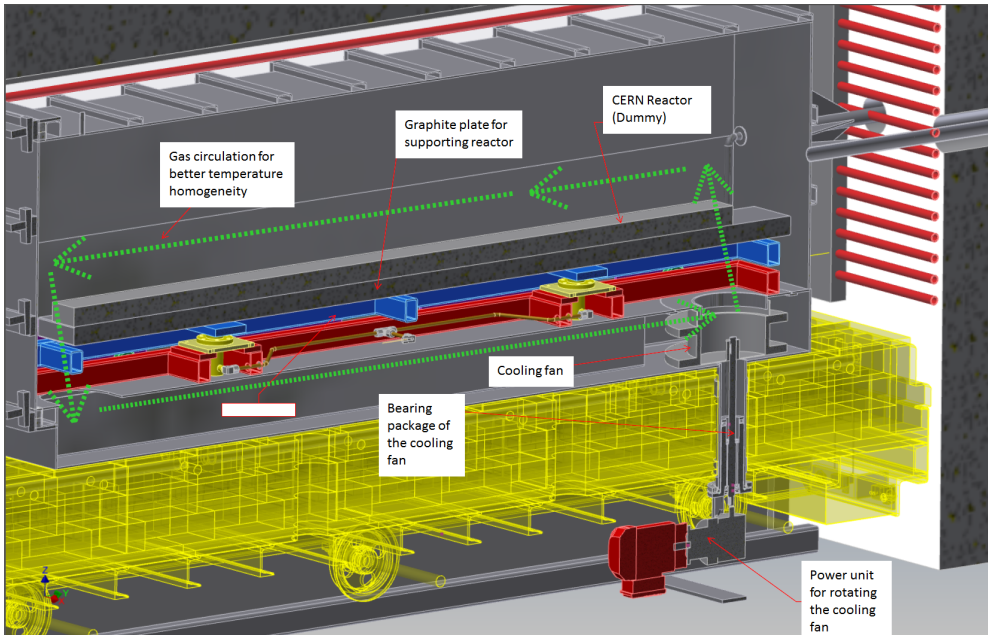

Figure 5.5: A half-cut overview of the inner area. The cooling fan can be seen on the bottom right area of the retort. A centrifugal fan with radial (straight) blades is implemented. The circulation of inert gas is indicated with the green arrows.

A view inside the furnace can be seen in Figures 5.6 and 5.7 showing the ceramic insulation of the door opening. The door can be closed tightly to minimize heat losses through the door side.

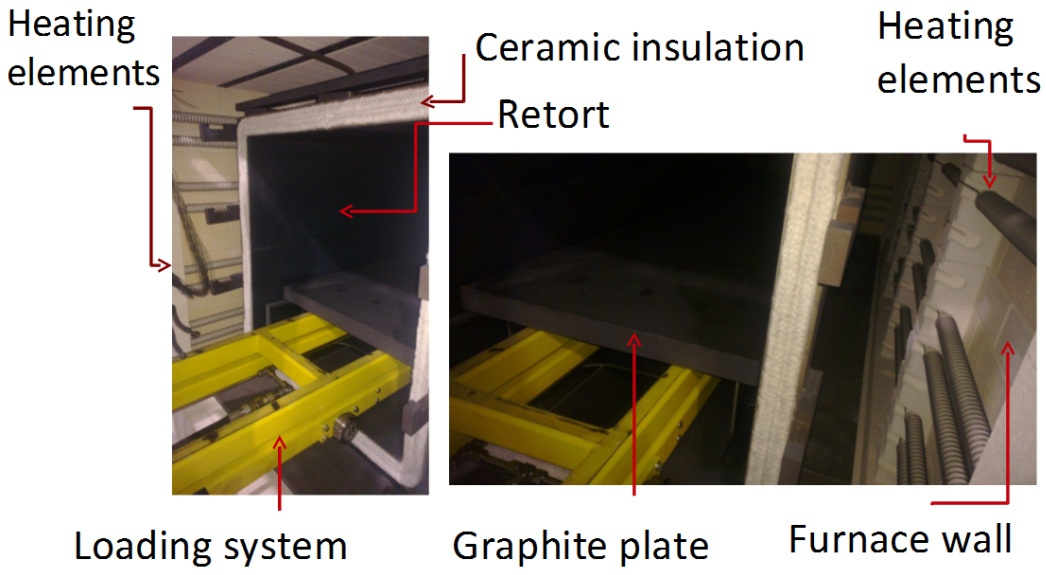

Figure 5.6: A view inside the furnace and retort through the door opening.

Figure 5.7: The front view of the furnace showing the door opened.

The fixture with T-bar structures can be seen in Figure 5.8. Temperature measurement of the furnace during heating was conducted before. Four temperature sensors were placed on tips of the two T-bars on top of the fixture to measure the temperature close to the roof and the side walls of the retort.

Figure 5.8: The fixture with T-bars. The four temperature sensors are located on both tips of the T-bars, and 20 temperature sensors all along the surface, in 10 mm deep holes.

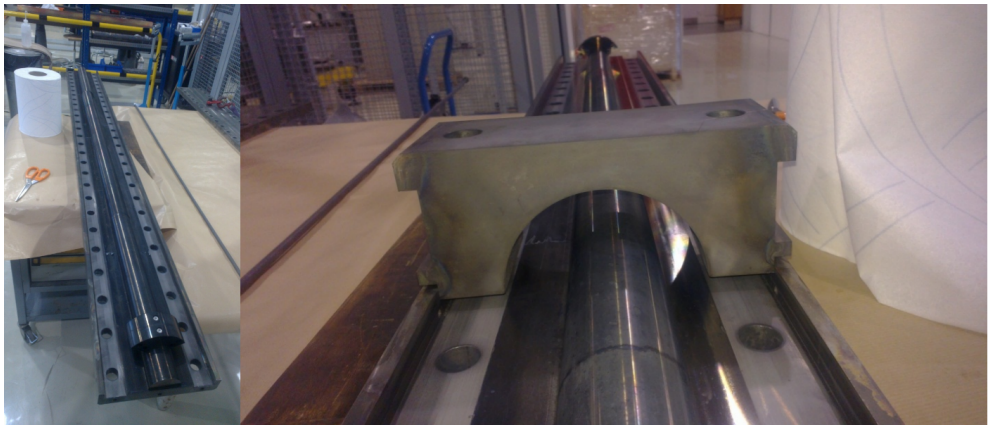

Figure 5.9: The inside area of the coil mould.

Additionally 20 temperature sensors were placed on the fixture to monitor fixture temperature in 10 mm deep holes on the surface of the fixture. The coil mould can be seen open in Figure 5.9. The coil is placed in the coil mould of the fixture. The fixture can be closed tightly by bolts.

5.2 Model of the furnace

The manufacturing of Nb_3S coils involves a heat treatment in order to perform diffusion towards superconducting characteristics. The diffusion process requires stringent temperature stability within 1°C. The aim is to find adequate numerical methods to verify various parameters of influence as the ramping rate [T/h] and the circulation speed of the used Ar-inert gas [m/s]. All these parameters are having an important influence on the heat cycle and especially on the temperature stability. Important in this analysis is to have an estimation of the temperature gradient inside the coil during the heat treatment.

To build a model of heat transfer in furnace is a complicated task. Hachem has researched stabilized finite element method for heat transfer and turbulent flows inside industrial furnaces in the Ecole des Mines de Paris, Centre de mise en forme des Matériaux. [17]

The furnace has heating elements around its inner walls. During the ramping up of the temperature they create a certain heat flow into the furnace. The heat transfer can occur as radiation, conduction and natural convection, heating the surrounding gas and walls of the furnace, and finally the retort. Major part of the heat transfer occurs as radiative heat transfer between the heating elements and the outer wall of the retort box. As the retort is heated up, also the inert gas environment inside the retort and fixture are subject to the heat load.

It is very difficult to estimate the heat losses of the furnace through the insu-

lation of the walls or the door. It is not meaningful to try to build a model with a heat source on the heating elements and a full geometry of the furnace and the retort. With the sensors placed on the T-bar structures it was possible to directly monitor the temperature of the working volume near retort roof. The model should be compared against these results. Because of that it was decided that the retort inner surface facing the gas is included with a temperature load on it. It is sufficient to model only the inert gas domain of the retort with a fixture inside.

In the early stage of the furnace heat transfer model, it is not necessary to include the coil geometry inside the fixture. A worst case-scenario of the heat transfer into the middle of the coil can be computed assuming that the fixture is a solid steel block. Then the computed temperature gradient between the middle of the coil and in the extremities is larger than in reality due to the poor conductivity of steel with respect to conductivity of Nb_3Sn and copper.

Heat transfer coefficient α is a quantitative characteristic of convective heat transfer between a fluid medium (a fluid) and the surface (wall) flowed over by the fluid. This characteristic appears as a proportionality factor a in the Newton-Richmann relation

$$\dot{q} = \alpha(T_w - T_f) \tag{5.1}$$

where $\dot{q}$ is the heat flux density on the wall, T_w the wall temperature and T_f the characteristic fluid temperature.[43]

After the simplifications, there are no other boundary conditions than the temperature of the retort inner surface facing the gas and the fan rotational speed. The heat transfer is then defined by the temperature load on the inner retort surface, initial temperatures of the inert gas domain and fixture and heat transfer coefficient between the inert gas domain and the fixture. Between the retort and the fixture, the radiative heat transfer dominates. Hot spots apper at the extremities (corners) of the fixture during heating up due to the geometry of the retort and the fixture. Because of that the heat transfer between the gas and the solid vary along the surface of the fixture.

The thermal conduction inside the fixture cools down the surfaces of the fixture, and the turbulent flow of the fan transfers heat from the hot spots to colder regions. During the heating up the temperature load on the retort wall rises and enhances heat exchange constantly due to the increasing gradient of temperature between the retort load surfaces and the fixture walls. It is necessary to have a software that computes the wall heat transfer coefficient based on the turbulent wall function coefficient. The heat transfer coefficient should be consistent with the wall heat flux, the wall temperature and the wall adjacent temperature (near-wall temperature).

ANSYS CFX has this capability so it was chosen to be used to perform the analysis.

The fan geometry is complicated. In this first iteration it was not necessary to implement the fan as such into the models. Instead it was decided that the fan would be included as a virtual fan. It can accelerate gas inside the retort to create turbulent flow in the retort without being accurately modelled by using the momentum source available in CFX.

All the geometries of the retort and fixture were simplified as much as possible to obtain sufficiently accurate results in the limited time frame. It was desided that in this first iteration, material parameters were kept constant, independent of the temperature change. The material properties can be seen in the Tables A.3 and A.4 on pages 102-103 in the Appendix.

The analysis contains three different cases that differ in the rotational speed of the fan. The three cases are:

- A: Fan 905 r/min
- B: Fan 450 r/min
- C: Fan 0 r/min

5.3 Domains and Boundary conditions

The dimensions of the model are shown in Figure 5.10. It was necessary to only include the half of the furnace due to the use of symmetry about the z-axis.

The domains chosen are the Fixture domain (steel), Gas domain (argon) and Fan sub-domain of the Gas domain (argon) at the fan location. Sub-domains can be defined to domains. Sub-domains use the same numerical models as default as the domains they were defined. Their location can be seen in the Figure 5.11.

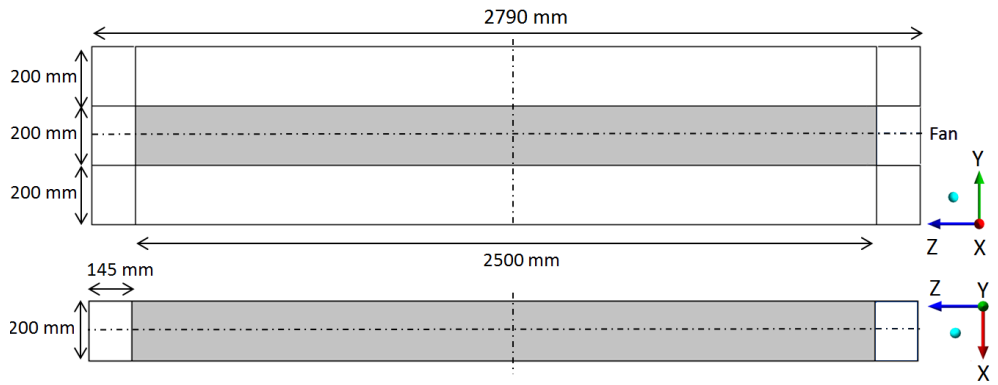

Figure 5.10: The dimensions of the model

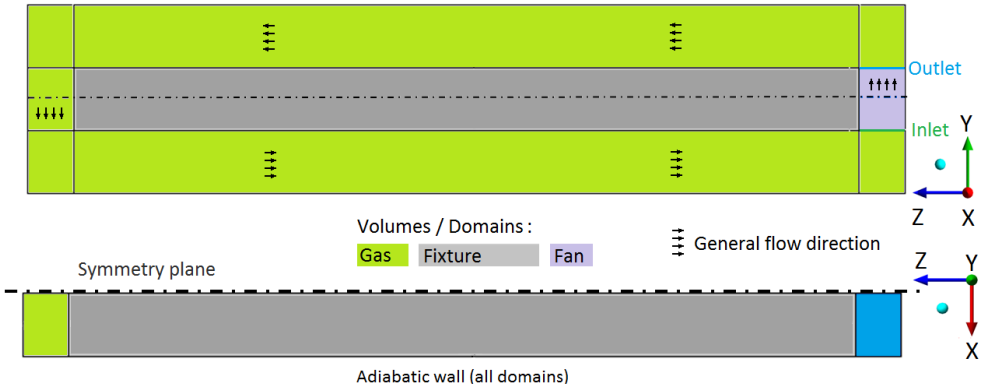

Figure 5.11: The volumes and domains of the model

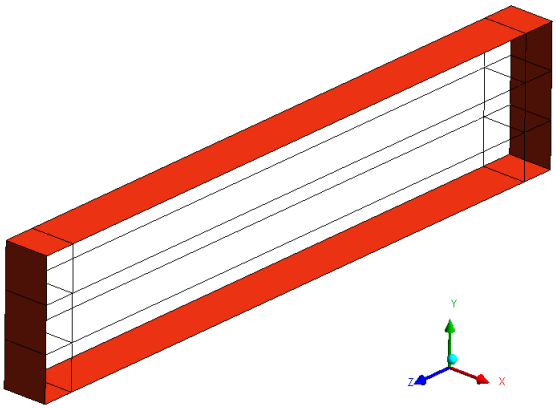

Figure 5.12: The load surfaces of the retort box.

One uses the symmetry about z-axis (Figure 5.11) and adiabatic boundary condition is given for the front wall (Figure 5.11).

Temperature load is applied around retort (50°C/h ramp from 200 to 400°C, then constant 400°C for 2 h). The load surfaces are shown in the Figure 5.12 The general momentum source load for fan sub domain is defined in the Fan sub-domain.

5.4 Thermal Energy-heat transfer model

The thermal energy model includes the transport of enthalpy through the fluid domain and it does not include the effects of mean flow kinetic energy. It consequently reproduces the same results as the Total Energy model when kinetic energy effects disappear and is suitable for modelling heat transfer in low-speed flows as the flow inside the retort.

The heat transfer by conduction or convection is governed by the equation of energy conservation. This equation is the only one to consider in the case of non-deformable solids. On the other hand, in fluids, heat transfer is related to the flow

and thus, the simulation of the convective heat transfer generally requires the computation of the velocity. [46]

Problems which deal with convection are governed by the instantaneous equations of mass, momentum and energy conservation. For turbulent flows, the instantaneous equations are averaged leading to additional terms. The continuity equation is defined in x-direction as

$$\frac{\partial \rho}{\partial t} + \vec{\nabla} \cdot (\rho \vec{u}) \quad = \quad 0. \tag{5.2}$$

where ρ is the density ($[\rho] = \mathrm{kg/m^3}$), t the time ($[t] = \mathrm{s}$), and $\vec{u}$ the fluid velocity vector.

The momentum equation in x-direction is defined as

$$\rho \frac{\partial u_x}{\partial t} + \rho \vec{u} \vec{\nabla} u_x \quad = \quad \vec{\nabla}(\mu \vec{\nabla} u_x) - \frac{\partial p}{\partial x} \tag{5.3}$$

where u_x is the component of velocity in x-direction ($[u_x] = \mathrm{m/s}$), μ is the molecular (dynamic) viscosity ($[\mu] = \mathrm{kg/(m\ s)}$) and p the pressure ($[p] = \mathrm{kg/(m\ s^2)}$).
The thermal energy equation is defined in x-direction as

$$\frac{\partial}{\partial t}(\rho c_p T) + \vec{\nabla}(\rho \vec{u} c_p T) \quad = \quad \vec{\nabla} \cdot (\lambda \vec{\nabla} T) + q. \tag{5.4}$$

where c_p is the specific heat capacity of the fluid in constant pressure ($[c_p] = \mathrm{kg^2/(s^2\ K)}$) T the temperature of the fluid ($[T] = \mathrm{K}$), λ the thermal conductivity of the fluid ($[\lambda] = \mathrm{(kg\ m)/(s^3\ K)}$, and q the volumetric heat source ($[q] = \mathrm{kg/(m\ s^3)}$). The equations are defined similarly in y and x-directions, velocity u_x being replaced by u_y or u_z. [46]

5.5 Conjugate heat transfer

CFX enables the creation of solid regions (domains) in which the equations for heat transfer are solved, but with no flow. This is known as conjugate heat transfer. The conservation of energy equation can account for heat transport due to solid motion, conduction and volumetric heat sources within solid domains as follows [12]

$$\frac{\partial}{\partial t}(\rho c_{ps} T_s) + \vec{\nabla}(\rho \vec{u}_s c_{ps} T_s) \quad = \quad \vec{\nabla} \cdot (\lambda_s \vec{\nabla} T_s) + q_s. \tag{5.5}$$

where c_{ps} is the specific heat capacity of the solid, $\vec{u}_s$ the velocity vector of the solid, Ts the temperature of the solid, λ_s the thermal conductivity of the solid, and q_s the volumetric heat source of the solid.[46]

5.6 The $k-\varepsilon$-turbulence model

Turbulent flow is characterized by very rapid fluctuations of the velocity, the pressure and the temperature. In most of cases the flow is turbulent, meaning that it presents vortices, also called eddies. Modelling turbulence is an extremely difficult task because eddies can be of different scale. A way to model turbulence is obtained by expressing the velocity terms appearing in Navier-Stokes equations, with a mean value and a fluctuation written as

$$u = \bar{u} + u', \tag{5.6}$$
$$v = \bar{v} + v', \tag{5.7}$$
$$p = \bar{p} + p', \tag{5.8}$$
$$t = \bar{t} + t'. \tag{5.9}$$

This set of time-averaged equations are called RANS (Reynolds Average Navier-Stokes) equations. [46]

The k-ε model is a two equation model, which means, it includes two extra transport equations to represent the turbulent properties of the flow. The first transported variable is the turbulent kinetic energy k ($[k] = \mathrm{m}^2/\mathrm{s}^2$), which determines the energy in the turbulence. The second transported variable is the turbulent dissipation ε ($[\varepsilon] = \mathrm{m}^2/\mathrm{s}^3$), which determines the scale of the turbulence.

The $k-\varepsilon$ model gives good results only in cases where mean pressure gradients are small. The accuracy has been shown experimentally to be reduced for flows containing large adverse pressure gradients. [46]

The $k-\varepsilon$ model is based on the turbulent viscosity concept, so that

$$\mu_{eff} = \mu + \mu_t, \tag{5.10}$$

where μ_{eff} is the effective viscosity ($[\mu] = \mathrm{kg}/(\mathrm{m\ s})$), μ the molecular (dynamic) viscosity and μ_t the turbulence viscosity. The $k-\varepsilon$ model assumes that the turbulence viscosity is linked to the turbulence kinetic energy k and the turbulence dissipation

rate ε via the relation [46]

$$\mu_t = C_\mu \rho \frac{k^2}{\varepsilon}, \tag{5.11}$$

where C_μ is the $k-\varepsilon$ turbulence model constant and k is the turbulence kinetic energy per unit mass. It is defined as the variance of the fluctuations in velocity. It has dimensions of $[length]^2[time]^{-2}$, as for example m^2/s^2. The turbulence dissipation ε is the rate at which the velocity fluctuations dissipate, and has dimensions of k per unit time, $[length]^2[time]^{-3}$, as m^2/s^3. [12]

The two extra equations related to the turbulent kinetic energy k and the turbulent dissipation ε are the following [46]

$$\begin{aligned} \frac{\partial}{\partial t}(\rho k) + \frac{\partial}{\partial x}(\rho \bar{u} k) + \frac{\partial}{\partial y}(\rho \bar{v} k) &= \frac{\partial}{\partial x}((\mu + \frac{\mu_t}{\sigma_k})\frac{\partial k}{\partial x}) + \frac{\partial}{\partial y}((\mu + \frac{\mu_t}{\sigma_k})\frac{\partial k}{\partial y}) \\ &\quad + P_k - \rho\varepsilon, \end{aligned} \tag{5.12}$$

$$\begin{aligned} \frac{\partial}{\partial t}(\rho \varepsilon) + \frac{\partial}{\partial x}(\rho \bar{u} \varepsilon) + \frac{\partial}{\partial y}(\rho \bar{v} \varepsilon) &= \frac{\partial}{\partial x}((\mu + \frac{\mu_t}{\sigma_\varepsilon})\frac{\partial \varepsilon}{\partial x}) + \frac{\partial}{\partial y}((\mu + \frac{\mu_t}{\sigma_\varepsilon})\frac{\partial \varepsilon}{\partial y}) \\ &\quad + c_{1\varepsilon}\frac{\varepsilon}{k}P_k - \rho c_{2\varepsilon}\frac{\varepsilon^2}{k}, \end{aligned} \tag{5.13}$$

where σ_k is the turbulence model constant for the k equation, σ_ε, $c_{1\varepsilon}$ and $c_{2\varepsilon}$ are the $k-\varepsilon$ turbulence model constants and P_k is the turbulent kinetic energy production defined as

$$P_k = -\rho\overline{u'^2}\left(\frac{\partial \bar{u}}{\partial x}\right) - \rho\overline{u'v'}\left(\frac{\partial \bar{u}}{\partial y} + \frac{\partial \bar{v}}{\partial x}\right) - \rho\overline{v'^2}\left(\frac{\partial \bar{v}}{\partial y}\right). \tag{5.14}$$

The different constants are determined experimentally [11] and evaluated as

$$C_\mu = 0.09, \sigma_k \approx 1, \sigma_\varepsilon = 1.3, c_{1\varepsilon} = 1.4, c_{2\varepsilon} = 1.92.$$

5.7 Shear Stress Transport (SST) Method-turbulence model

The SST method is also a two equation model, but it actually combines the effects of the $k-\varepsilon$ method and the $k-\omega$ method. It was developed to blend the robust and accurate formulation of the $k-\omega$ model in the near-wall region with the free-stream independence of the $k-\varepsilon$ model in the far field. To achieve this, the $k-\varepsilon$ is converted into a $k-\omega$ formulation. The SST model is similar to the standard $k-\omega$ model, but it includes the following refinements: [46; 47]

- The standard $k-\omega$ model and the transformed k-ε model are both multiplied by a blending function and both models are added together. The blending function is designed to be one in the near-wall region, which activates the standard $k-\omega$ model, and zero away from the surface, which activates the tansformed $k-\varepsilon$ model;
- The SST model includes a damped cross-diffusion derivative term in the ω equation;
- The definition of the turbulent viscosity is modified to account for the transport of the turbulent shear stress;
- The modeling constants are different.

These features make the SST model more accurate and reliable for a wider class of flows than the standard $k-\omega$ model.

This model assumes that eddy-viscosity [16],

$$\nu_t = \frac{\mu_t}{\rho}, \tag{5.15}$$

is computed as follows (Menter SST two-equation model from 2003 [15; 14])

$$\nu_t = \frac{a_1 k}{\mathbf{max}\left(a_1\omega, SF_2\right)}, \tag{5.16}$$

where S is the strain rate (strain invariant),

$$S = \sqrt{2S_{ij}S_{ij}}, \tag{5.17}$$

a_1 is the model constant and F_2 the blending function.

The blending function F_2 is defined as follows

$$F_2 = \mathbf{tanh}\left[\left[\mathbf{max}(\frac{2\sqrt{k}}{\beta^*\omega y}, \frac{500\nu}{y^2\omega}\right]^2\right] .[13] \tag{5.18}$$

For turbulence kinetic energy applies

$$\frac{\partial k}{\partial t} + \frac{\partial u_j k}{\partial x_j} = P_k - \beta^* k\omega + \frac{\partial}{\partial x_j}\left[(\nu + \sigma_k\nu_t)\frac{\partial k}{\partial x_j}\right] \tag{5.19}$$

where σ_k is the turbulent Prandtl number for k. It is defined as follows

$$\sigma_k = \frac{1}{\frac{F_1}{\sigma_{k,1}} + \frac{(1-F_1)}{\sigma_{k,2}}}, \tag{5.20}$$

and the term P_k is defined

$$P_k = \mathbf{min}\left(\tau_{ij}\frac{\partial U_i}{\partial x_j}, 10\beta^* k\omega\right) \tag{5.21}$$

where [15]

$$\tau_{ij} = \mu_t\left(2S_{ij} - \frac{2}{3}\frac{\partial u_k}{\partial x_k}\delta_{ij}\right) - \frac{2}{3}\rho k\delta_{ij}, \tag{5.22}$$

$$S_{ij} = \frac{1}{2}\left(\frac{\partial u_i}{\partial x_j} + \frac{\partial u_j}{\partial x_i}\right). \text{ [15]} \tag{5.23}$$

For the specific dissipation rate applies

$$\begin{aligned}\frac{\partial \omega}{\partial t} + \frac{\partial u_j \omega}{\partial x_j} &= \alpha S^2 - \beta\omega^2 + \frac{\partial}{\partial x_j}\left[(\nu + \sigma_\omega \nu_T)\frac{\partial \omega}{\partial x_j}\right] \\ &\quad +2(1-F_1)\sigma_{\omega 2}\frac{1}{\omega}\frac{\partial k}{\partial x_i}\frac{\partial \omega}{\partial x_i},\end{aligned} \tag{5.24}$$

where σ_ω is the turbulent Prandtl number for ω. It is defined as follows

$$\sigma_\omega = \frac{1}{\frac{F_1}{\sigma_{\omega,1}} + \frac{(1-F_1)}{\sigma_{\omega,2}}}, \tag{5.25}$$

and the blending function F_1 [13]

$$F_1 = \mathbf{tanh}\left\{\left\{\mathbf{min}\left[\mathbf{max}(\frac{\sqrt{k}}{\beta^*\omega y}, \frac{500\nu}{y^2\omega}, \frac{4\sigma_{\omega 2}k}{CD_{k\omega}y^2}\right]\right\}^4\right\}. \tag{5.26}$$

The term $CD_{k\omega}$ can be defined as

$$CD_{k\omega} = \mathbf{max}\left(2\rho\sigma_{\omega 2}\frac{1}{\omega}\frac{\partial k}{\partial x_i}\frac{\partial \omega}{\partial x_i}, 10^{-10}\right). \text{[14]} \tag{5.27}$$

The different model constants are $\beta^* = \frac{9}{100}$, $\sigma_{k1} = 0.85$, $\sigma_{k2} = 1$, $\sigma_{\omega 1} = 0.5$, $\sigma_{\omega 2} = 0.856$.

Each of the rest of the model constants is a blend of an inner (1) and outer (2) constant, blended via [15]

$$\phi = \phi_1 F_1 + \phi_2(1 - F_1). \tag{5.28}$$

where ϕ_1 represents constant 1 and ϕ_2 represents constant 2 and the constants are $\alpha_1 = \frac{5}{9}$, $\alpha_2 = 0.44$, $\beta_1 = \frac{3}{40}$, $\beta_2 = 0.0828$.

5.8 Pressure-velocity coupling

It is necessary to enhance models that include fans to accomodate a modified pressure-redistribution term. In CFX, a co-located (non-staggered) grid layout is used so that the control volumes are identical for all transport equations. These kind of methods lead to a decoupled (checkerboard) pressure field. To avoid this, Rhie and Chow [19] proposed an alternative discretization for the mass flow, and it was modified by Majumdar [20] to remove the dependence of the steady-state solution on time step. The pressure-velocity coupling can be chosen in CFX for the Fan-sub-domain. More information on the pressure-velocity coupling can be found in the CFX manual. [41]

5.9 Radiation Transport

The goal of the radiation modeling is to solve the radiation transport equation, obtain the source term, S, for the energy equation, and the radiative heat flux at walls, among other quantities of interest. The problem should be restricted to coherent time-independent radiation processes. This is normally a very good approximation of situations likely to be met in industrial applications, where the time scale for radiation to come into local equilibrium is very short and the temperatures are relatively low. [41]

The spectral radiative transfer equation (RTE) can be written as

$$\begin{aligned} \frac{dI_\nu(\mathbf{r},\mathbf{s})}{ds} &= -(K_{a\nu} + K_{s\nu})I_\nu(\mathbf{r},\mathbf{s}) + K_{a\nu}I_b(\nu,T) + \\ &\quad \frac{K_{s\nu}}{4\pi}\int_{4\pi} dI_\nu(\mathbf{r},\mathbf{s'})\Phi(\mathbf{s}\cdot\mathbf{s'})d\Omega' + S_i \end{aligned} \tag{5.29}$$

where ν is the frequency ($[\nu] = 1/\mathrm{s}$), $\mathbf{r}$ the position vector, $\mathbf{s}$ the direction vector, s

the path length ($[s] = \mathrm{m}$), K_a the absorbtion coefficient, K_s the scattering coefficient, I_b the blackbody emission intensity ($[I_b] = \mathrm{W}/(\mathrm{m}^2)$).

I_ν is the spectral radiation intensity ($[I_b] = \mathrm{W}/(\mathrm{m}^2)$), which depends on the position (r) and the direction (s), T the local absolute temperature ($[T] = \mathrm{K}$), Ω the solid angle, Φ the in-scattering phase function, S the radiation intensity source term ($[S_i] = \mathrm{W}/(\mathrm{m}^2)$), or particle-radiation interactions.

For the Multiband and Weighted sum of Gray gases, the solution must be computed for each spectral band (sub-index ν of the symbols) and a final integration to obtain the total radiation quantities is required. One uses the Gray spectral model, so the computation is done once for a unique radiation intensity field.

The RTE is a first order integro-differential equation for I_ν in a fixed direction, $\mathbf{s}$. To solve this equation with a domain, boundary condition for I_ν is required. Because the furnace doesn't have transparent walls, it is sufficient to have the condition for diffusively emitting and reflecting opaque boundaries, as follows [41]

$$I_\nu(\mathbf{r}_w, \mathbf{s}) = \varepsilon_\nu(r_w) I_b(\nu, T) + \frac{\rho(\mathbf{r}_w)}{\pi} \int_{n \cdot S' < 0} I_\nu(\mathbf{r}_w, \mathbf{s}') \mid \mathbf{n} \cdot \mathbf{s}' \mid d\Omega', \qquad (5.30)$$

where ε_ν is the spectral emissivity.

5.10 The Discrete Transfer model

The discrete transfer model is based on tracing the domain by multiple rays leaving from the bounding surfaces. It depends upon the discretization of equation of transfer along rays. the path along a ray is discretized by using the sections formed from breaking the path at element boundaries. The physical quantities in each element are assuemd to be uniform.

The rays are traced through the domain in the same manner as the photons would be tracked in the Monte Carlo model. Hence, the model description for both Monte Carlo and Discrete Transfer is identical. For the results to be accurate the elements must be chosen so that the radiation field is reasonably homogenous inside them. The elements have to be small enough that the scattering optical depth is less than unity across each element. [41]

The implementation of the Discrete Transfer model in CFX assumes that the scattering is isotropic; therefore, equation 6.29 can be simplified as

$$\frac{dI_\nu(\mathbf{r},\mathbf{s})}{ds} = -(K_{a\nu}+K_{s\nu})I_\nu(\mathbf{r},\mathbf{s}) + K_a I_b(\nu,T) + \frac{K_{s\nu}}{4\pi}\int_{4\pi} I_\nu(\mathbf{r},\mathbf{s'})d\Omega' + S_i. \tag{5.31}$$

Assuming that the system is reasonably homogenous, so that

$$I_\nu(\mathbf{r}) \sim I_\nu(\mathbf{r}+d\mathbf{r}) \qquad q_\nu^R(\mathbf{r}) \sim q_\nu^R(\mathbf{r}+d\mathbf{r}), \tag{5.32}$$

the approach is then to solve for the intensity, I_ν, along rays leaving from the boundaries using the equation of transfer

$$I_\nu(\mathbf{r},\mathbf{s}) = I_{\nu 0}\, e^{(-(K_{a\nu}+K_{s\nu})s)} + I_{b\nu}(1-e^{(-K_a s))} + K_{s\nu}\overline{I_\nu} \tag{5.33}$$

where $I_{\nu 0}$, I_ν are radiation intensity leaving the boundary and mean radiation intensity, respective.

Then, integrate I over solid angle at discrete points to get the spectral incident radiation G, and the radiative heat flux q_r ($[q_r] = \mathrm{W}/(\mathrm{m}^2)$), and use the homogeneity assumption to extend the solution to the entire domain. Non-linearities in the system due to scattering, diffuse reflection, or temperature dependency of radiation quantities is overcome by iteration. [41]

5.11 Fan model

Introduction to fans

Fans utilize power from a motor to output a volumetric flow of air at given pressure. They are usually composed of blades attached to a rotor that could give a centrifugal or axial momentum to the fluid, depending on their orientation. Moving blades of a propeller increase static pressure across the fan rotor and increase kinetic energy of air particles. Axial fans deliver air in an overall direction that is parallel to the fan blade axis. They can be designed to produce a high flow rate, but they can work against relatively low pressure. Centrifugal fans deliver air in a perpendicular direction to the blower axis at relatively low flow rate, but, for a given air volume, they are able to operate against high pressure. A centrifugal and and an axial fan can be seen in Figure 5.13. In the furnace a centrifugal fan with radial (straight) blades is implemented.

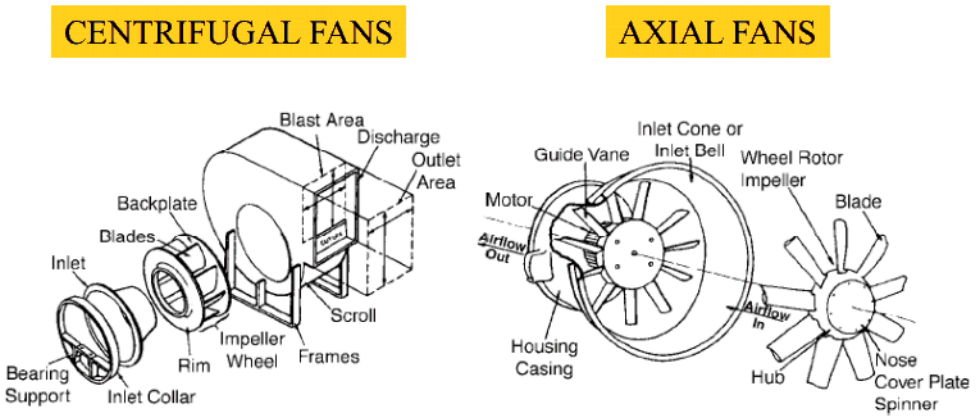

Figure 5.13: Components of centrifugal and axial fans. [18]

In order to describe and summarize the parameters playing a role in the fan operation, considerations about the velocity vectors for air at a blade inlet and outlet are done leading to useful equations that are not described here in details.

Fan curves

The aerodynamic aspects of a fan are described in a fan curve, such as in Figure 5.14. The fan performance curve has to be read from right to left, because at the right one starts with a healthy aerodynamic flow ending up with the aerodynamic stall at the left (shut-off point). Unlike for an airplane wing, aerodynamic stall is not critical for the functionality of the fan. The stalled fan will deliver air at an increased static pressure, with a decreased volumetric flow rate, and increase in noise. From an energy viewpoint at the shut-off point, the fan is in the condition of the maximum potential energy. In contrast at free delivery, the fan is in the condition of the maximum kinetic energy. Neither of the conditions exist in practice, but it is useful to understand it to be able to compare fans.

The system curve describes the aerodynamic resistance of the system, against which the fan is working. The operating point of the fan is located at the intersection of the system curve and fan curve. Fans settle to the operating point after the flow conditions have stabilized. [49]

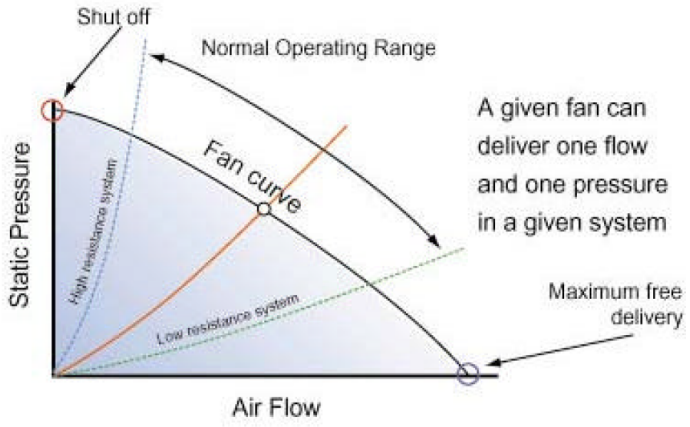

Figure 5.14: A generalized fan curve. The red line is the system curve, that characterizes the aerodynamic resistance of the system. The operating point is the white dot in the middle of Figure.

A manufacturer of fans provides a fan curve for each fan they produce. The fan curves predict the pressure-flow rate performance of each fan. Each fan has it's own typical fan curve that characterizes the fan performance. The fan curve has the static pressure p_{st} ($[p_{st}]$=Pa) as a function of volumetric flow rate $\dot{V}$ ($[\dot{V}]$ = m^3/s).[48] The pressure curves of the centrifugal fan of the furnace for two rotational speeds can be seen in Figure 5.15.

According to [44]:
"Static pressure is the difference between the absolute pressure at a point in an air stream or aplenum chamber and the absolute pressure of ambient atmosphere, being positive when the pressure at the point is above the ambient pressure and negative when below. It acts equally in all directions, is independent of velocity and is a measure of the potential energy available in an air stream."

This applies for argon gas as well. A fan has to overcome the static pressure that causes the resistance of flow for instance in ducts and ventilation channels.

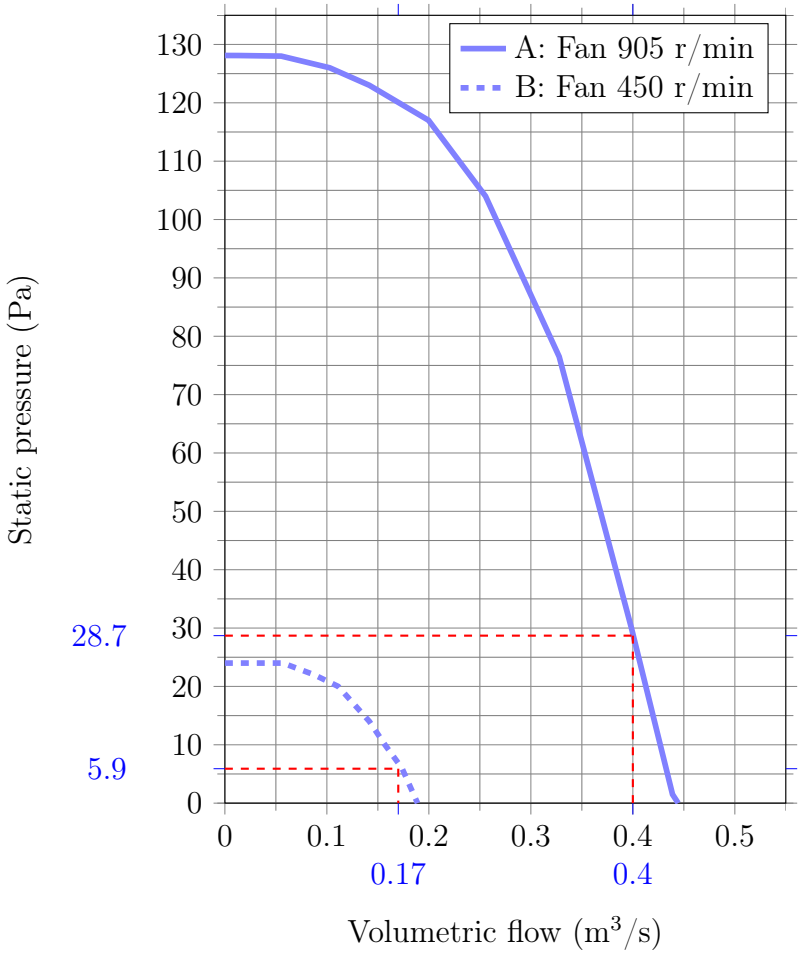

Figure 5.15: The fan curves of the furnace fan for the two rotational speeds used in the simulations. The red dashed lines indicate the operation points of the fan in CFX-models, when the solutions have stabilized after 100 s. The fan has the dimensions: ⌀355 x 102 x 236,5 mm (without a case). Max power intake of the fan of the case A: 40 W and of the case B: 3 W [32]

In many CFD codes, The fan curve can be used to build a virtual fan without actually modelling the real fan's blade geometry. One has to take the assumption as

$$p_{st} = \Delta p, \tag{5.34}$$

where Δp is the algebraic difference between the mean total pressure at the fan outlet and the mean total pressure at the fan inlet. It is the measure of the total mechanical energy added to the air or gas by fan.[44]

Δp will now be used to form the following equations, but will be interpreted as the static pressure on the fan curves. The fan curve can be implemented in CFX as a

function given as [45]

$$f(\Delta p) = \dot{V} \tag{5.35}$$

Force density

Before going to more details, one should undestand the definition of force density. In fluid mechanics, the force density is the negative gradient of pressure. It has the physical dimensions of force per unit volume. It is a vector field representing the flux density of the hydrostatic force within the bulk of the fluid. Force density is represented by the symbol f ($[f] = \mathrm{N/m^3}$), and is defined as divergence of pressure

$$f = \nabla p, \tag{5.36}$$

where p is the pressure.

Hence, the net force dF on a differential volume element dV of the fluid is

$$dF = f dV. \tag{5.37}$$

Thus, the force density at a point in a fluid, divided by the density, is called the acceleration of the fluid at a point [50]. The virtual fan should produce the force density that corresponds to the force density of a real fan.

General momentum source

The force density equation can be supplied to the CFD-software (in CFX momentum source, as expressions) and it can be allowed to determine the operating point and system resistance. The CFD-software works by numerically solving the governing equations of flow and heat transfer in three dimensions and takes in the account the effects of turbulence (and gravity). [49]

In CFX, the fan can be modelled by defining a sub-domain to a volume, and by setting a source of force density to that volume, which is called the general momentum source. For the direction parallel to y-axis, it can be denoted S_y. It has the unit of force density. With the assumption that the virtual fan and the real fan have exactly the same geometries, the momentum source is given as

$$S_y = -C_s(v - v_{spec}(\Delta p)), \tag{5.38}$$

where C_s is the momentum source term coefficient ($[C_s] = \mathrm{kg/(m^3 s)}$), v is the computational velocity parallel to y-axis ($[v] = \mathrm{m/s}$), $v_{spec}(\Delta p)$ is the specific velocity of the fan ($[v_{spec}] = \mathrm{m/s}$), the velocity relative to the pressure difference Δp over the fan sub-domain. The specific velocity functions as a control variable of the momentum source.

Defining a momentum source to a volume adds an additional force term to the Navier-Stokes equations on each node belonging to the volume. It can be applied to any coordinate direction[45]. It should be noted, that the unit of the momentum source term coefficient is chosen so, that the momentum source has the same units as the force density. It is used to obtain good convergence, when the source is a function of velocity.[45] However, according to author's experience the momentum source term coefficient C_s is a variable, which depends on the velocity of the flow. It should be experimentally tuned to match the velocity at all times. In this simulation, it was defined as in the Table 5.2.

Time (s)	$C_{s,A}$	$C_{s,B}$
0.0	0.010	0.003
0.1	0.050	0.020
0.5	1.000	0.300
0.6	5.000	2.000
10.0	500.000	250.000
$\geq$ 20.0	800.000	350.000

Table 5.2: Momentum source term coefficients for the case A and B.

It is necessary to set both the "Redistribute in Rhie Chow" and "Include Coefficient in Rhie Chow" parameters true in Sources tab, when the momentum source is meant to induce a pressure change (like fan model, for instance), to avoid pressure wiggles near the subdomain boundary [45].

For the specific velocity, the following applies

$$v_{spec}(\Delta p) = \frac{f(\Delta p)}{A_{fan}}, \tag{5.39}$$

$$v_{spec}(\Delta p) = \frac{f(p_{out} - p_{in})}{A_{fan}}, \tag{5.40}$$

where A_{fan} is the sectional area of the fan, p_{in} is the average pressure at the inlet of the fan (see Figure 5.11 on the page 59), p_{out} is the average pressure at the outlet of the fan (see Figure 5.11 on the page 59). [45]

At an operating point

$$v_{spec}(\Delta p^*) = \frac{\dot{V}^*}{A_{fan}}, \tag{5.41}$$

where $\dot{V}^*$ is the volumetric flow of the fan at an operating point Δp^*=p_{out}*-p_{in}*.

It is now possible to examine how the real fan curve can be applied to the model when the geometry of the fan is simplified from the reality. The total force produced by the real and virtual fans must be equal:

$$F_{fan} = F_{vir}, \tag{5.42}$$

where F_{fan}, F_{vir} is the total force produced by the real fan and the total force produced by the virtual fan, respectively.

When applying fan curves of a real fan geometry to simplified model geometries, one must be careful to take in account the size of the real fan volume. It is necessary to define a new parameter, K, that takes in account the volume size differences. It is given by

$$K = \frac{V_{fan}}{V_{vir}}, \tag{5.43}$$

where V_{fan} is the volume of the real fan, V_{vir} is the volume of the virtual fan. Finally it can be concluded that the momentum source in the model should be corrected with the parameter K. The momentum source is then given by

$$S_y = -C_s(v - v_{spec}(\Delta p))K. \tag{5.44}$$

It can be noted that the volume of the real fan defines the total force of the fan model. Great care need to be taken to find out the effective real fan volume.

The numerical models, interfaces and domains

The presented numerical models are applied to domains. They were applied as follows:

- Thermal energy heat transfer model (Gas-domain, Fan-sub-domain)
- Conjugate heat transfer model (Fixture-solid domain)
- $k-\varepsilon$-model with scalable wall function and SST-turbulence model with automatic wall function (Gas-domain, Fan-sub-domain)
- For the case C (Fan 0 r/min) laminar model was used instead of a turbulence model
- Pressure-velocity coupling (Gas-domain, Fan-sub-domain)
- Discrete transfer radiative heat transfer model with Surface to Surface-transfer model and Gray-spectral model (Gas domain, Fan sub-domain).

The numerical models applied to interfaces between solid and gas domain are General connection-interface model and Conservative interface flux-heat transfer model. Between the connections inside the Gas-domain (including the Fan sub-domain) the Conservative interface flux-option for mass and momentum is chosen.

As an initial condition for all domains is 200° C temperature. For the Gas-domain 1 atm relative pressure is given and a zero velocity condition for all cartesian directions.

Mesh

The mesh of the domains can be seen in Figure 5.16. The mesh was refined to allow adequate computation of the velocity profile close to the boundaries between the Fixture- and Gas-domains, and the boundary between Gas-domain and inner retort wall. The minimum thickness of the mesh was 1.50 mm (in the z-axis direction) and maximum 2.25 (in y-axis direction).

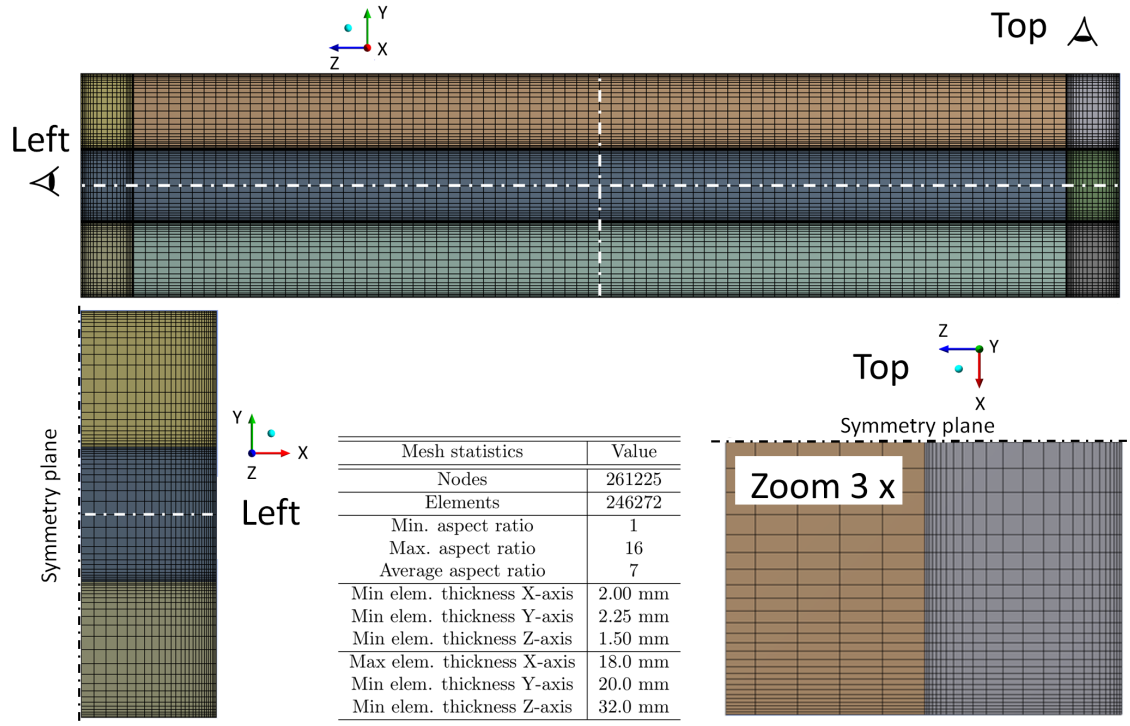

Mesh statistics	Value
Nodes	261225
Elements	246272
Min. aspect ratio	1
Max. aspect ratio	16
Average aspect ratio	7
Min elem. thickness X-axis	2.00 mm
Min elem. thickness Y-axis	2.25 mm
Min elem. thickness Z-axis	1.50 mm
Max elem. thickness X-axis	18.0 mm
Min elem. thickness Y-axis	20.0 mm
Min elem. thickness Z-axis	32.0 mm

Figure 5.16: The mesh of the model and statistics of the mesh.

Time steps

The time steps (Table 5.3) depend on the turbulence model used. They were found by experience. Normally too high time steps led to non-convergence, so it was necessary to reduce their size especially in the beginning of the computation when the velocity of the gas increases fastly. After the velocities have stabilized, larger time step sizes can be used to reduce computational time.

$Time$(s)	A_{SST}	$A_{k-\varepsilon}$	B_{SST}	C_{lam}
0	0.01	1^{-4}	0.01	0.01
1	0.05	$1^{-4}t$	0.05	0.05
10	0.10	$1^{-4}t$	0.10	0.10
$\geq$100	2.00	$1^{-4}t$	1.00	1.00

Table 5.3: The time steps of the models (s). In the $A_{k-\varepsilon}$ column, t=$Time$. A: Fan 905 r/min B: Fan 450 r/min C: Fan 0 r/min. A&B: $k-\varepsilon$ and SST-turbulence models, C: laminar model (none).

5.12 Validation of the model

The fan model validation

No experimental measurement data was available for comparison with the simulated fan outlet velocities. In Figure 5.17 it can be seen that while the specific velocity decreases after starting the simulation, the velocity of argon rises rapidly. After the rough start, the velocities stabilize to decent values.

In Figure 5.18 the rise of the pressure difference Δp can be compared with the rise of the average velocity of argon at the fan outlet. It can be immediately seen that the curves have different shapes. For the case A, Δp doesn't stabilize as smoothly as for the case B.

In the Figure 5.19 and 5.20 the streamlines of the velocity can be seen. After comparing these figures it can be noted that the turbulent velocity profile seems to be fully developed after 14.6 s.

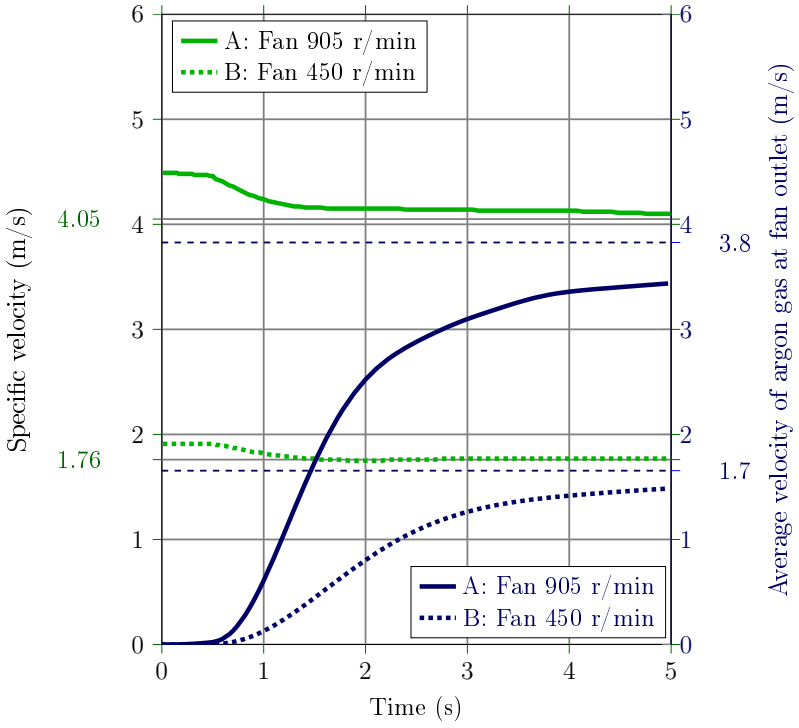

Figure 5.17: Velocities of the fan right after the start of the simulation. All curves stabilize after 100 s to their operating point values marked on the diagram. The SST-turbulence model was used.

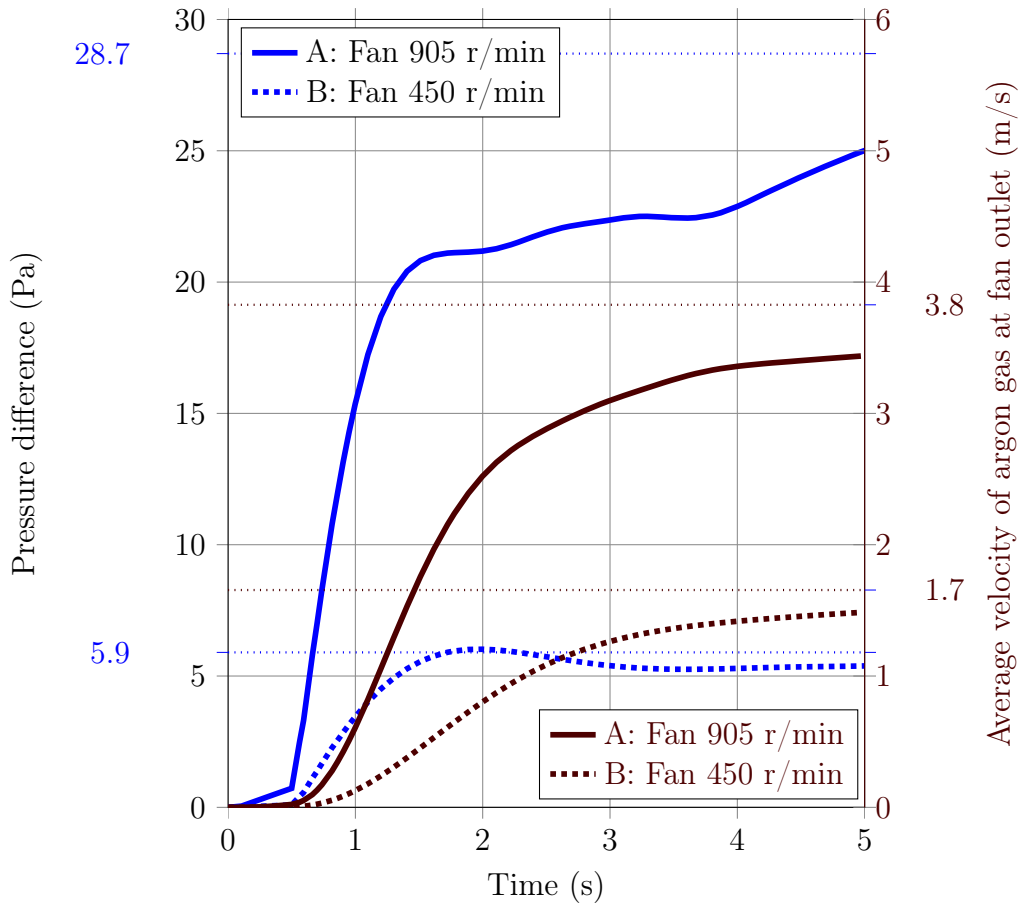

Figure 5.18: Pressure differences of the fan compared to velocities right after start of the simulation. All curves stabilize after 100 s to their operating point values marked on the diagram. The SST-turbulence model was used.

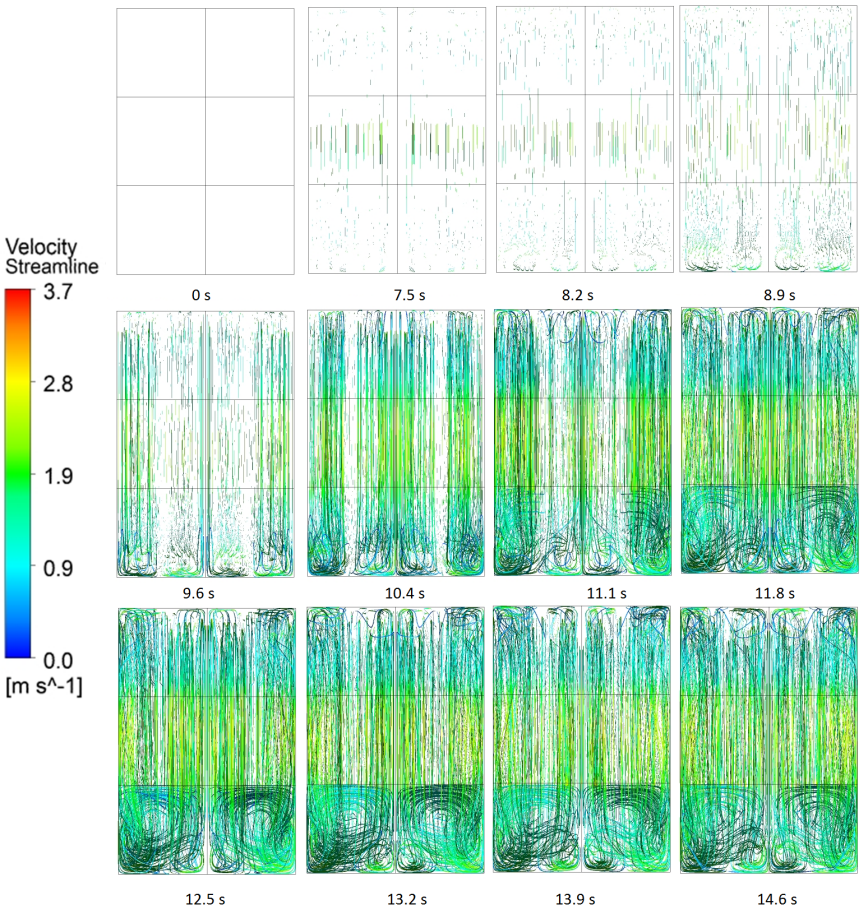

Figure 5.19: The velocity streamlines of the case B (SST) from 0-14.7 s towards the negative direction of the z-axis (the fan is located behind). Development of turbulence can be seen.

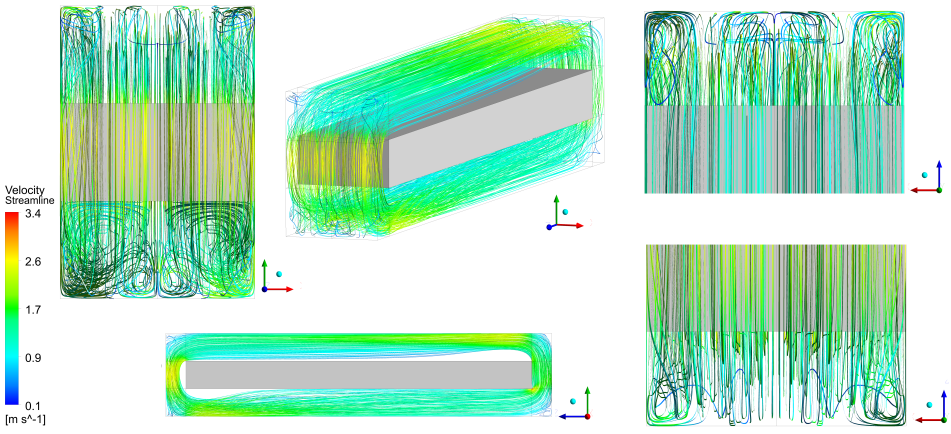

Figure 5.20: The velocity streamlines of the case B (SST) at $t = 6\ h$.

Validation of the heat transfer model using real furnace temperature measurements

5.13 Measurements of fixture and retort temperatures

Temperatures of the fixture and retort were measured during heating. The fan was switched on after 25 min of heating working with 50% of its maximum rotational speed (450 rotations/min). After 15 min of fan operation, circulation of the gas the four temperature sensors showed good agreement of temperatures differing only 2 degrees° C at maximum between 1.5-15 h of heating. Because the temperatures agreed well, the temperature data of one of these sensors was picked as a representative temperature of the retort and called the "Temperature Zone 1" (TZ 1). The ramping up of "Temperature Zone 1" can be seen in Figure 5.21.

Additionally 20 temperature sensors were placed on the fixture to monitor fixture temperature. For this thesis, the mean temperature of nine sensors amongst them is called the "Measured fixture average", that represents the average fixture surface temperature. All of the sensors were placed each on the bottom of a hole, 10 mm deep from the fixture surface.

The furnace heat transfer model was verified against the measured data. The curve "Temperature Zone 1" (TZ 1) was used as a temperature load boundary condition in CFX (TZ1 load for CFX in the graph). The temperature results of CFX were exctracted fom the points shown in Figure 5.27. The curve "Measured fixture average" was compared with different averaging between points in the CFX model (Case 1: average temperature of (T1, T2, T3, B1, B2, B3) Case 2: average temperature of (T2,B2), Case 3: temperature of M only.

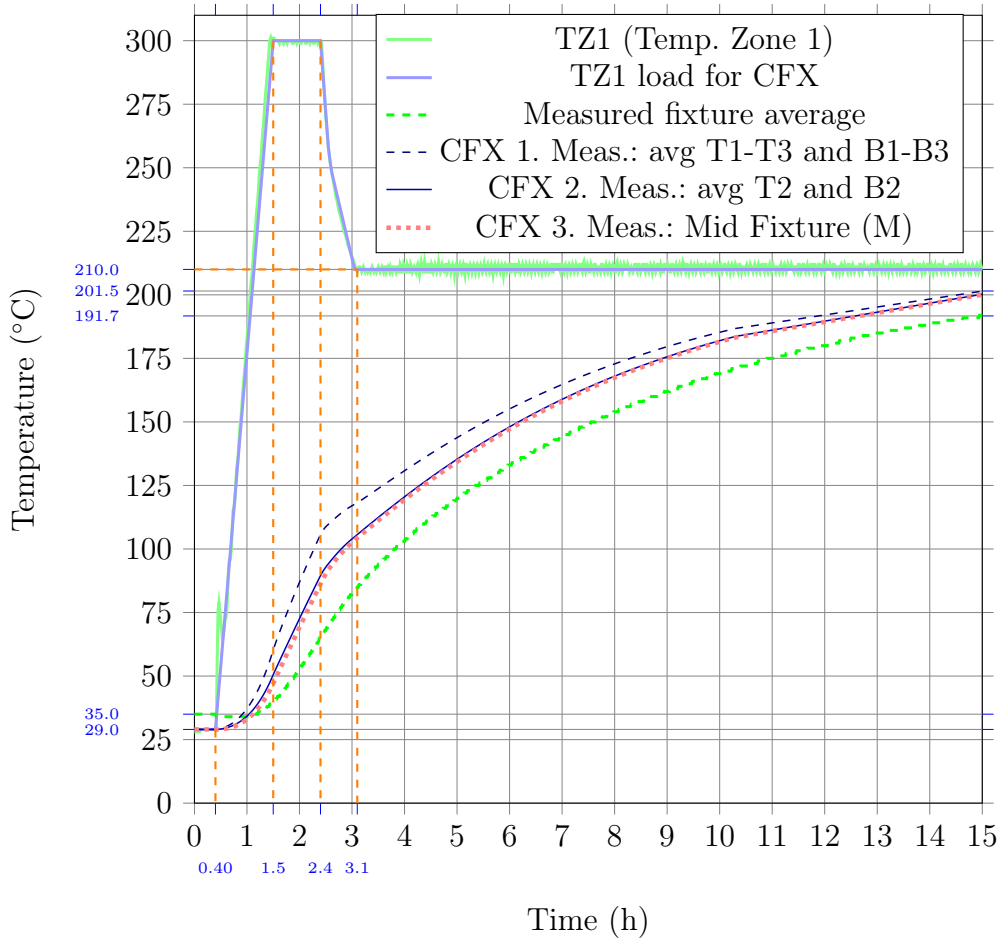

Figure 5.21: The comparison of the temperature of the real retort/furnace. The difference between real furnace and model is only 10 °C after 15 h showing relatively good agreement. The SST-turbulence model was used.

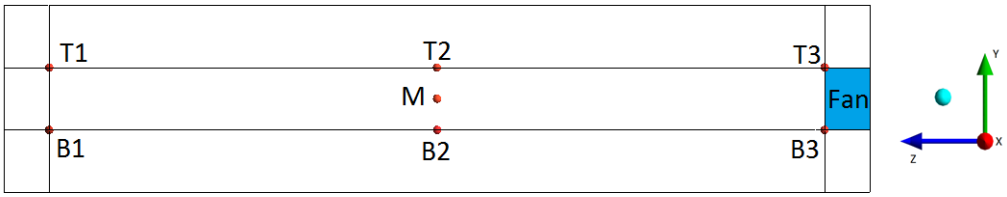

Figure 5.22: The results of this section were exctracted from these points.

The effect of turbulence model on heat transfer

The effect of turbulence model on heat transfer is shown in Figure 5.23. The maximum difference between the models is only 2 °C showing relatively good agreement between the models. It shows that both models can give similar results, but practice has shown that the SST-method is less time consuming by a factor of five. The SST-method can be recommended to be used if one has the choice between the two.

The result points are shown in Figure 5.24.

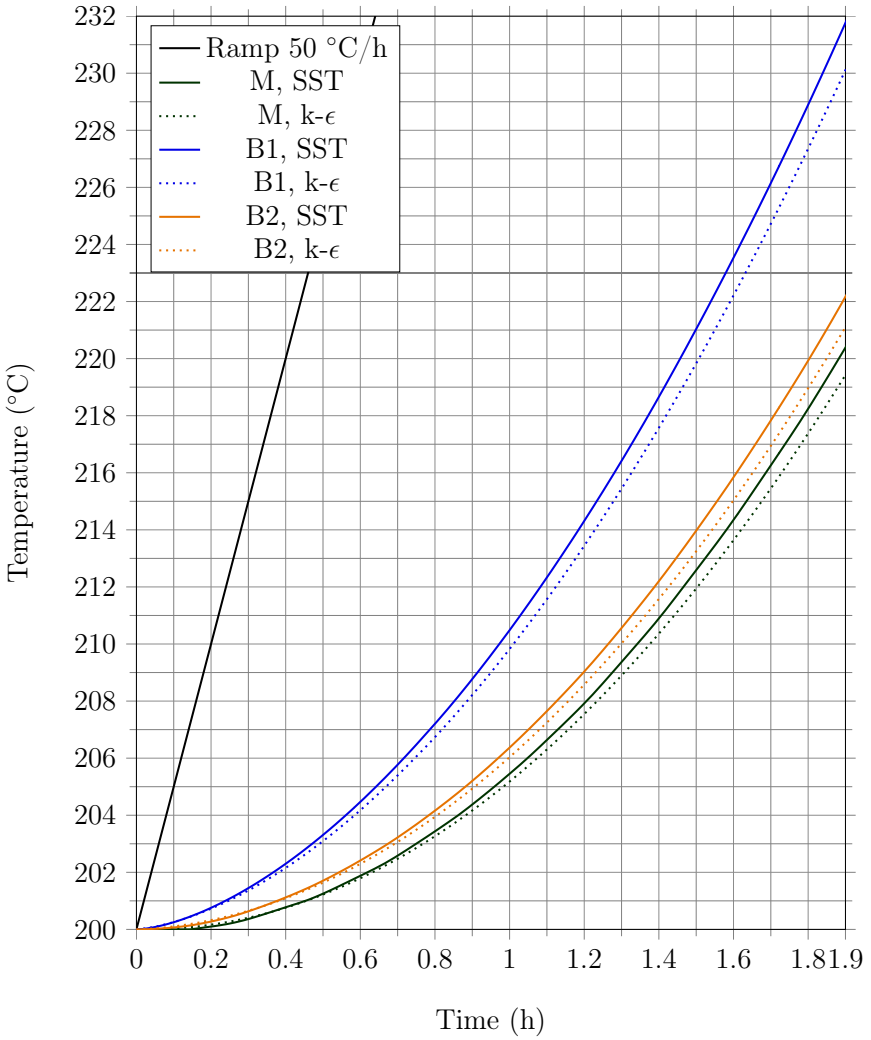

Figure 5.23: Comparison of the effect of turbulence models on heat transfer. Temperatures from 0 to 1.9 h calculated using $k-\varepsilon$ and SST- turbulence models of the case A (Fan 905 r/min) in measurement points M (fixture middle), B1 (bottom left), B2 (bottom middle) are shown. It can be seen that the maximum difference between models is only 2 °C showing relatively good agreement between the models.

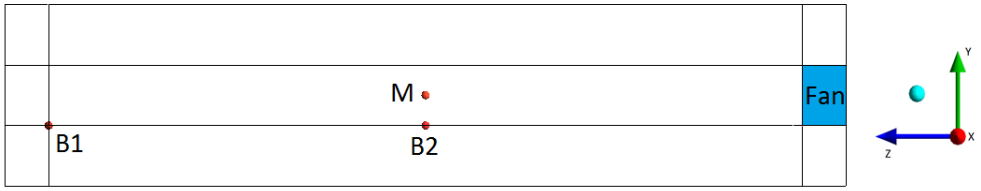

Figure 5.24: The results of this section were exctracted from these points.

Numerical accuracy

The RMS residual level can help to judge convergence of the run (i.e. the numerical errors during the run). The default residual parameters in CFX are explained in Table 5.4. The RMS residuals of the model with a fan running 905 r/min for six hours, using SST-method as a turbulence model can be seen in Figure 5.25. On it, red lines for 1e-4 and 1e-5 have been drawn. It can be stated based on CFX manual that:

- Values larger that 1e-4 may be sufficient to obtain a qualitative understanding of the flow field
- 1e-4 is relative loose convergence, but may be sufficient for many engineering applications
- 1e-5 is good convergence, and usually sufficient for most engineering applications
- 1e-6 or lover is very tight convergence, and occasionally required for geometrically sensitive problems.

Residual	Subsystem
HenergyGas	Heat transfer
KturbKE	Turbulence kinetic energy
UMom	Momentum x-dir.
VMom	Momentum y-dir.
WMom	Momentum z-dir.
PMass	Mass

Table 5.4: The equations solved in CFX and their residual monitor parameters. The SST-turbulence model was used.

Thus one managed to achieve very tight level of convergence for all the other RMS residuals except heat transfer, which stayed between relatively loose and good convergence levels. It has to be taken in account that largest numerical errors are made in the iterations during the first hour of simulation time. Convergence for all other models was also checked and the results were very similar. In overall, the convergence level can be judged sufficient for the simulation.

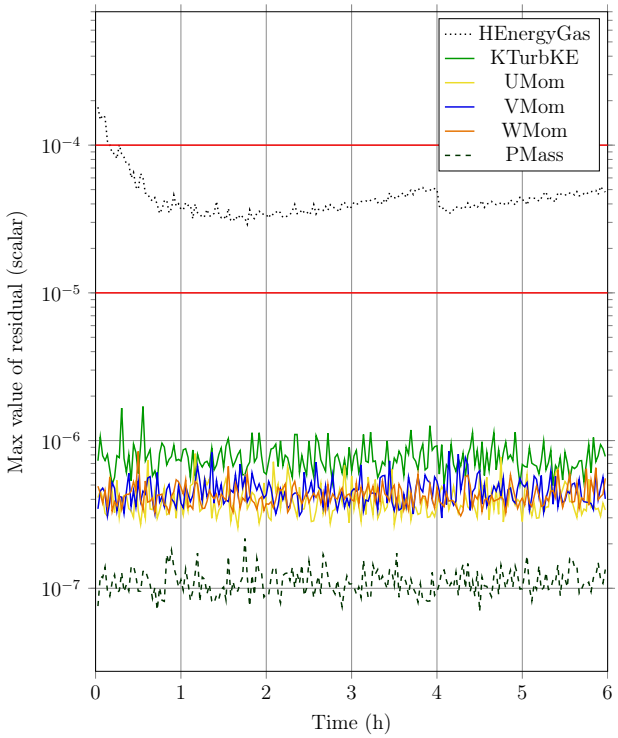

Figure 5.25: The RMS residuals of the case A (fan 905 r/min) running for six hours, using SST-method as a turbulence model. The red line for 1e-4 shows the level of sufficient convergence, and 1e-5 shows the level of good convergence.

5.14 Results of the simulation

The temperature distribution of the model is seen in Figure 5.26. It can be seen how the ends of the fixture heat up faster while the middle of the fixture stays colder longer. The temperature difference between the middle area of the fixture and the load surfaces is about 40°C.

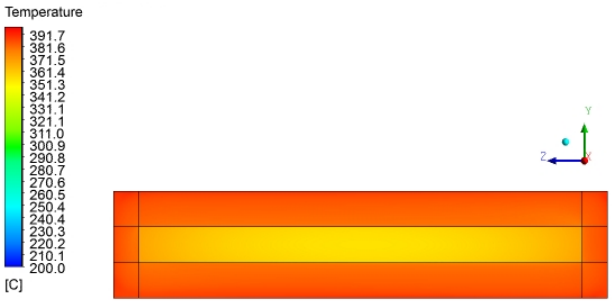

Figure 5.26: Temperature profile after 6h, case B, SST-turbulence model.

The temperatures of the three points M, B1 and B2 shown in Figure 5.27 can be seen in Figures 5.28, 5.29 and 5.30. After four hours, the ramping up of the temperature is stopped, but the temperatures still keep rising fast with the gradient of 30-40°C

from the plateau temperature.

It can be stated that the temperature of the case A after 6 h at the point B1 (bottom left) is 15°C higher than the temperature at the point at the point M (fixture middle). All graphs show that the temperatures increase faster when the fan rotational speed is increased.

Figures show the difference of the temperatures of between cases. The largest difference between the cases A and C, 14.3°C occurs after 5 h of heating for the point M. On the other hand, between the cases B and C the temperature differs 8.6°C for the point M.

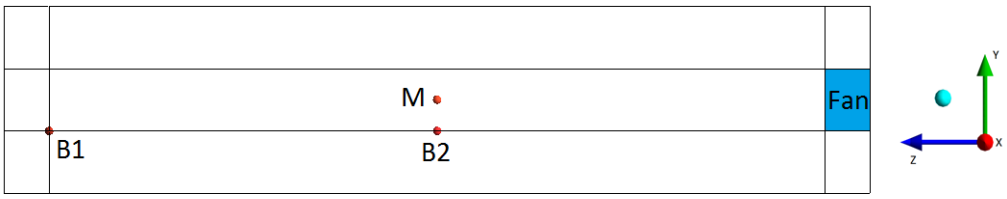

Figure 5.27: The results of this section were exctracted from these points.

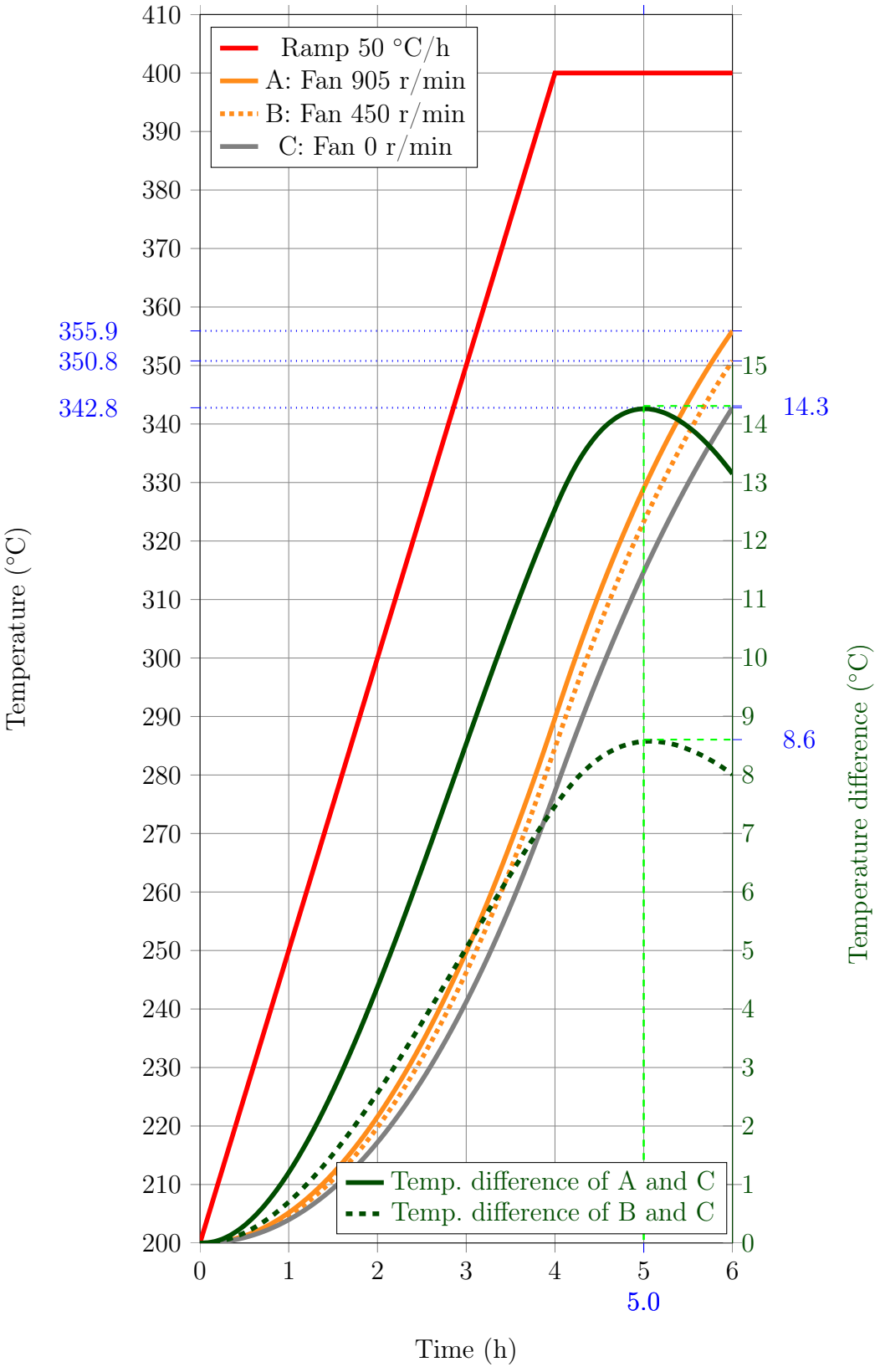

Figure 5.28: The temperature in the point M (fixture middle) is shown from 0 to 6 h (read values from the left side y-axis). The temperature difference between the cases can be seen in the green curves (read values from the right side y-axis). The SST-turbulence model was used. The location of the three points M, B1 and B2 is shown in Figure 5.27.

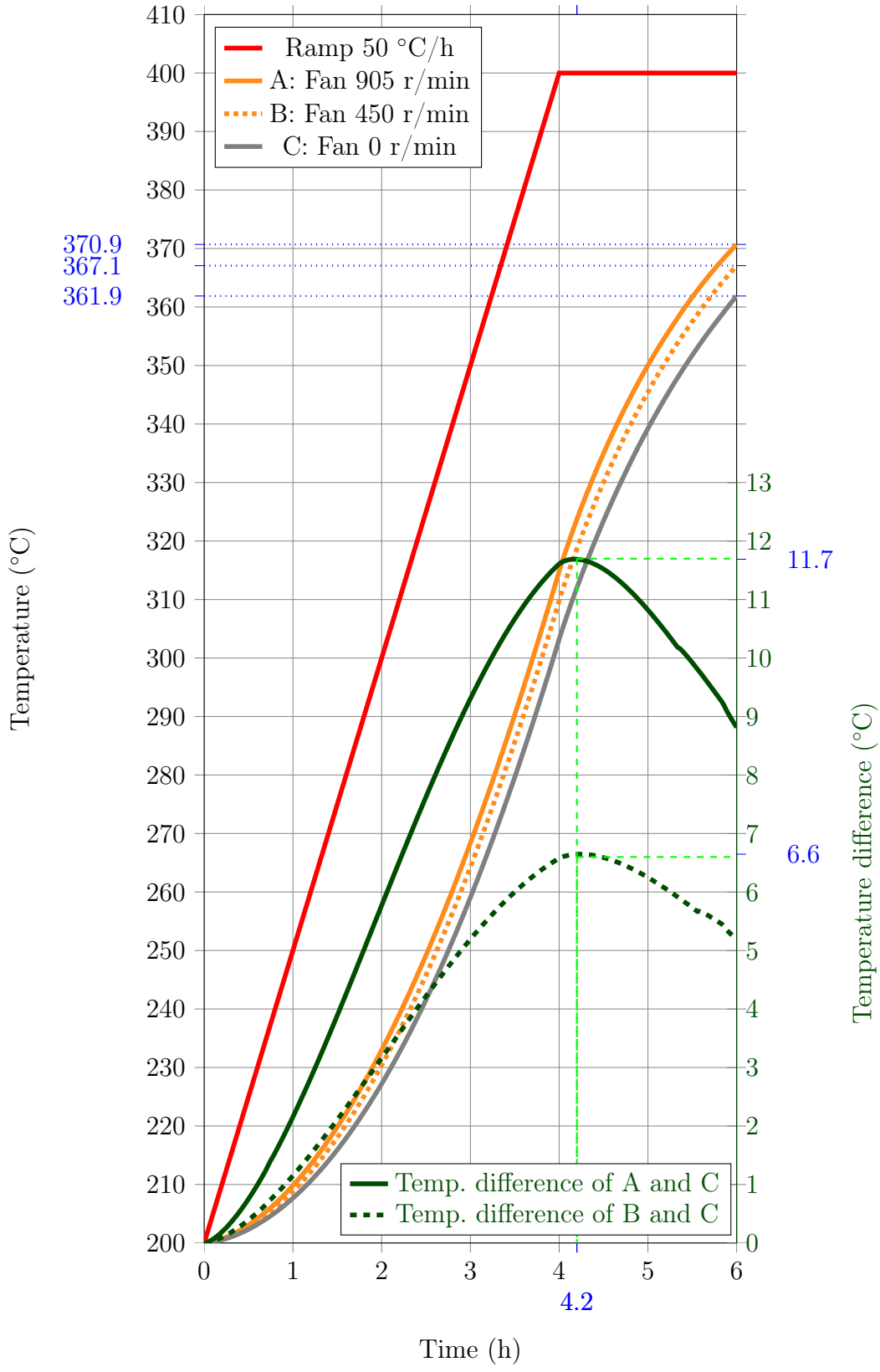

Figure 5.29: The temperature in the point B1 (bottom left) is shown from 0 to 6 h (read values from the left side y-axis). The temperature difference between the cases can be seen in the green curves (read values from the right side y-axis). The SST-turbulence model was used. The location of the three points M, B1 and B2 is shown in Figure 5.27.

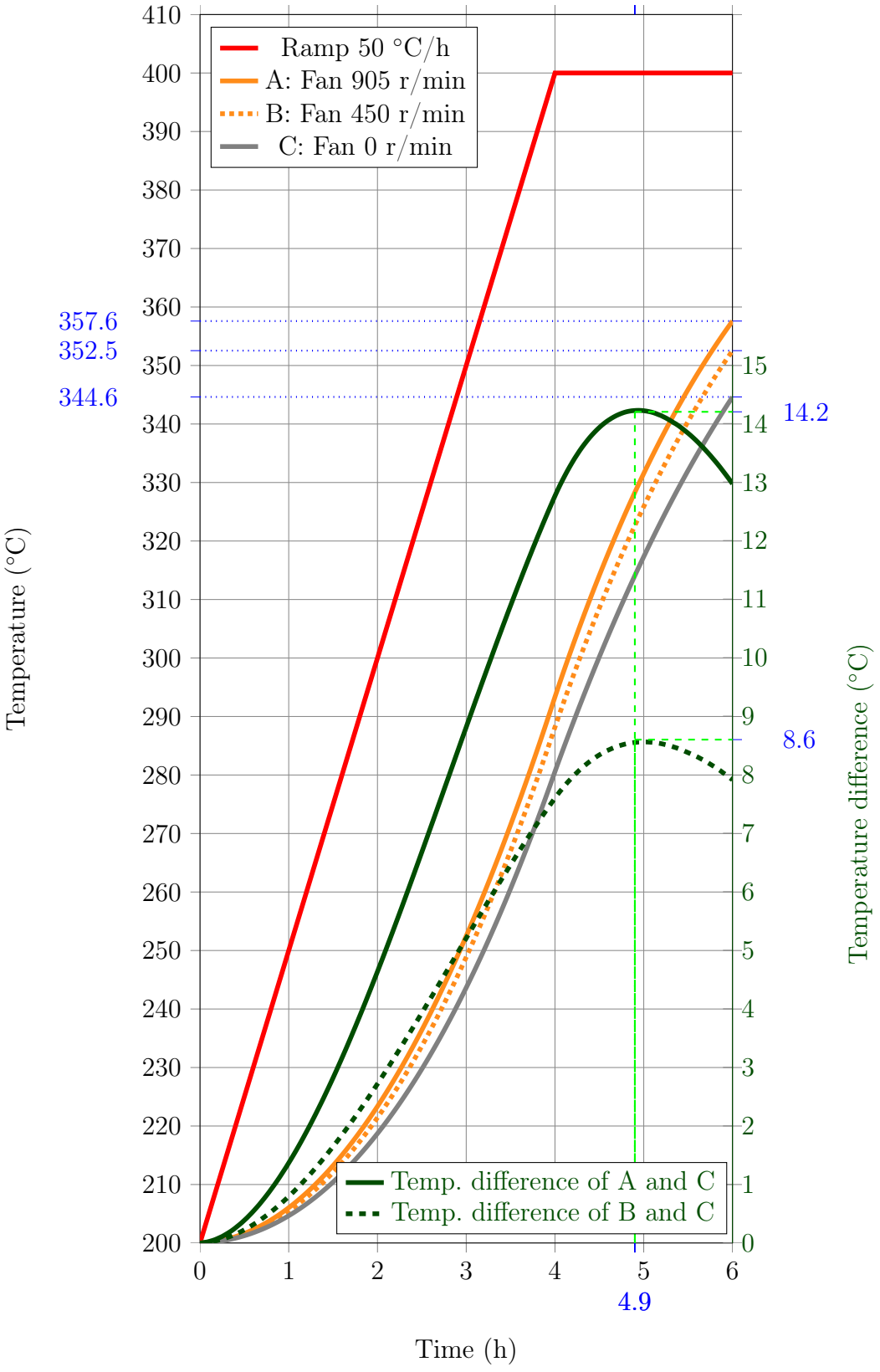

Figure 5.30: The temperature in the point B2 (bottom middle) is shown from 0 to 6 h (read values from the left side y-axis). The temperature difference between the cases can be seen in the green curves (read values from the right side y-axis). The SST-turbulence model was used. The location of the three points M, B1 and B2 is shown in Figure 5.27.

The temperature gradients between the point M and B1 and the gradient between the point M and B2 shown in Figure 5.31 and 5.32. It can be stated that the gradient between M and B1 is much higher than between points M and B2 for all cases. For the case A the gradient is about 25°C. The gradient for the case C (no fan) rises higher than for the cases A and B between the points B1 and M. On the contrary between the point B2 and M, the gradient of the cases A and B rises higher than for the case C. It implies that the fan works as it should; it cools down the hot spots on the corners of the fixture and heats up in the middle. It was verified that the other corners also have similar kind of behaviour than the point B1.

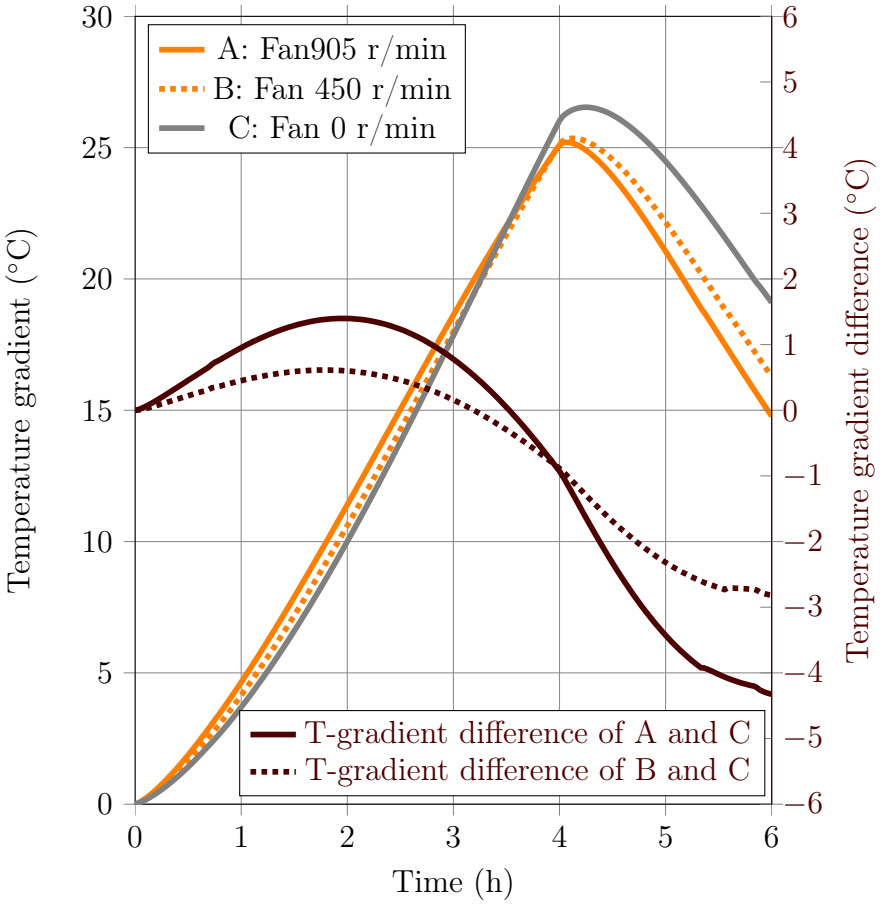

Figure 5.31: The temperature gradients of cases A-C between the points M (fixture middle) and B1 (bottom left) are shown from 0 to 6 h (read values from the left side y-axis). The brown curves show the difference between the cases (read values from the right side y-axis). The SST-turbulence model was used. The location of the three points M, B1 and B2 is shown in Figure 5.27.

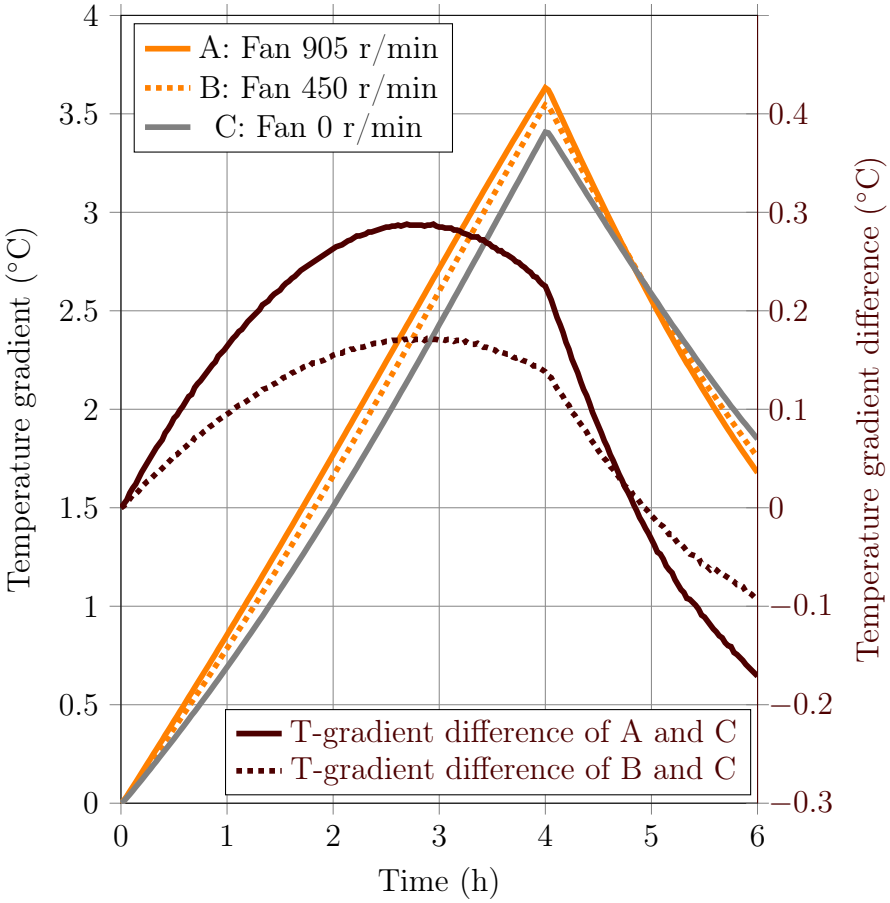

Figure 5.32: The temperature gradients of cases A-C between the points M (fixture middle) and B2 (bottom middle) are shown from 0 to 6 h (read values from the left side y-axis). The brown curves show the difference between the cases (read values from the right side y-axis). The SST-turbulence model was used. The location of the three points M, B1 and B2 is shown in Figure 5.27.

From all of these graphs it can be stated that the fixture heats up faster with the fan running. This can be verified from Figure 5.33 showing the heating power of the cases. The fan transfers heat from the corners to the middle, producing more homogenous temperature distribution on the surface of the fixture. However, the effect of the high ramp rate manages to overcome the effect of more uniform surface temperature, and the gradient increases due to too slow conduction. Based on this, the ramp rate should be reduced.

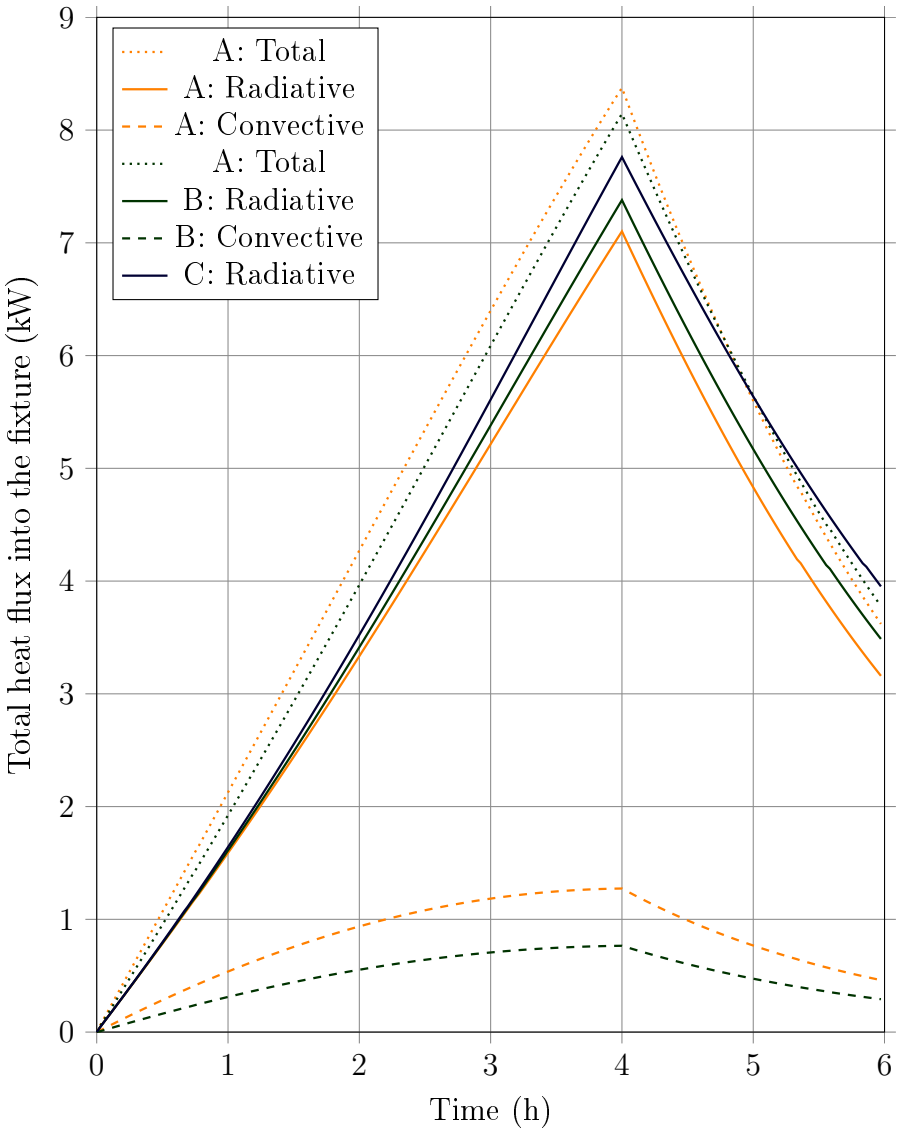

Figure 5.33: The total heat flux into the fixture through the four Gas-domain / Fixture-domain interfaces. The SST-turbulence model was used.

6. COMPREHENSIVE SUMMARY

This thesis was carried out as an important contribution to the further development program of superconductive magnets within the LHC high luminosity study currently on-going at CERN.

The thesis also provides an overview of the various steps implied in order to produce a superconductive magnet. It should be mentioned that the work carried out is mainly focusing on the mechanical assembly of the magnet components. This (part) does not imply the collaring of the coil as well as the coil winding and coil insulation process.

A major aspect was given by the welding assembly and the related aspects in terms of implied structural compression, explained in chapter four. This stress given by the so called shell stress was analysed base the FEA method and optimized in order to choose the right pressing force. As mentioned in the chapter three the pre-stress is required in order to close the gap in the half symmetry of the assembled mock-up. This is important in order to minimize the risk for so called quenches in the superconductive coil assembly.

All related constraints seen by the magnet were implied into the FEA model. This implies the cooling to 1.9 K as well as the operation at nominal current of 13 kA (12 T).

It was shown that the pressing force of 382 t/m corresponds to remaining average pre-stress of 190 MPa (azimuthal direction) inside the 15 mm thick welding shell at room temperature with a weld shrinkage of 0.47 mm.

Within this frame of work a sample press used for a short magnet mock-up welding has been refurbished. This implied the analysis of the required hydraulic system and the coordination of related activities. In addition the control user interface has been designed. The press allows finally a sectorization in 6 subsectors and can be controlled in an automated and manual mode.

An important contribution to the high luminosity upgrade of magnets is the utilization of Nb_3Sn superconductors. This method is different for the approach taken for the current NbTi conductors. The manufacturing of coils therefore implies the winding of the superconductor followed by a heat treatment in order to perform the diffusion towards superconductive characteristics.

This diffusion process is based on stringent temperature stability requirements

within 1°C on the temperature plateau. This defined heat treatment is based on three plateaus up to 650°C.
In order to achieve the homogeneity of this heat cycle CERN is currently launching an R&D program in order to verify the various parameters of influence. Therefore it was necessary to select and perform adequate numerical methods.

These methods will help to define critical process parameters as for example the ramping rate [°C/h], the circulation speed of the used Ar-inert gas [m/s]. All these parameters are having an important influence on the heat cycle and especially on the temperature stability.

In a first iteration of this work various numerical approaches based on different software packages were performed. It has been shown, that 2D- and 3D-modelling of such a complex tasks is feasible. The 2D-model has given a first indication for the heat transfer between the so called inner reaction fixture (coil mould) and the outer retort wall. In a further iteration the circulation of Ar-inert gas was implied. All iterations were compared to practical measurements which were performed within the MTF section of the superconducting magnet group at CERN.

After having defined the optimum numerical method a 3D-model of one symmetry of the furnace has been carried out. This approach implied the same stops as in the previous 2D model but further improvements were added.

This implied optimization of the used meshing as well as improved methods for the simulation of the fan circulation. The results are showing good correlation with the ones observed during the heat treatment of a first dummy mock-up coil. For example the ramping curve is correlated to the measured one and stays within 10°C during the required 15 h of heating. After reaching the first time plateau temperature in four hours and staying there for two hours, the results are showing the 25°C offset between the reaction fixture corner temperature and the inner coil temperature.

REFERENCES

[1] Karppinen[a], M., Andreev[b], N., Apollinari[b], G., Auchmann[a], B., Barzi[b], E., Bossert[b], R., Kashikhin[b], V.V., Nobrega[b], A., Novitski[b], I., Rossi[a], L., Smekens[a], D., Zlobin[b], A.V., [a] CERN, Geneva, Switzerland, [b] Fermilab National Accelerator Laboratory, Batavia, USA, February 2012, Design of 11 T Twin-Aperture Nb3Sn Dipole Demonstrator Magnet for LHC Upgrades, CERN-ATS-2012-033, 4p.

[2] Ahlbäck, J., Ikäheimo, J., Järvi, J., Leroy, D., Oberli, L. R., Perin, R., Perini, D., Russenschuck, S., Salminen, J., Savelainen, M., Soini, J., Spigo, G., Tortschanoff, T., July 1994, Electromagnetic and Mechanical Design of a 56 mm Aperture Model Dipole for the LHC, IEEE Trans. on Magnetics, vol 30, No. IV, pp. 1746-1749

[3] Bermudez S.I., With contribution of: Atieh, S., Favre, G., Mesenge, P., Morgadinho, F., Prever-Loiri, L. (EN-MME-AF), Piguiet, A-M. (EN-MME-MM), Auchmann, B., Karppinen, M., Kokkinos, C., Perez J. C. (TE-MSC-MDT), Prin, H., Savary, F. (TE-MSC-LMF), June 2012, Plane Welding tests, longitudinal welding of the shrinking cylinder, Internal Report of CERN's Main Workshop to set the geometry and welding parameters for the 1-in-1 dummy test for the 11T magnets, 7 p.

[4] Savary, F., with contributions from Auchmann, B., Grospelier, E., Bermudez, S. I. , Karppinen, M., Lackner, F., Murtomäki, J.S., Prin, H., 27th of September 2012, 11-T Dipole Collaboration Review, Cold Mass Fabrication and Tooling Procurement

[5] FS-MT/ESH, 11th October 1995, Mechanical measurements on 3 austenitic stainless steels. 1. The tensile tests on "base material (BM)" samples, May 1995, T=4.2 K, The value 316LN $BM_{average}$ = 748.67 MPa indicated in this thesis is the base material average based on three samples for the steel 316LN.

[6] Lackner, F., August 2012, Invitation to Tender, Technical Specification for the Supply of a Nb_3Sn Reaction Furnace, EDMS No.: 1224351, Group Code : TE/MSC, IT-3861/TE, 15 p.

[7] Pourrahim[a], S., Tuttle[b], J., Williams[a], J., Pourrahim[a], N., Shirron[b], P., [a] Superconducting Systems, Inc., 90 Rumford Avenue, Waltham, MA 02453, United States., [b] NASA Goddard Space Flight Center, Greenbelt, MD, United States., February-March 2006, Manufacturing of lightweight low-current Nb_3Sn ADR magnets operating at 10 K, Cryogenics, Volume 46, Issues 2-3, pp. 191-195

[8] Assmann, R., for the LHC Collimation Team: The reported work on the LHC collimation system was performed from 2003 to 2010 and relied on the work of the following persons at CERN and at outside collaborating institutes: Aberle, O., Assmann, R., Bacher, J.P., Baglin, V., Bellodi, G., Bertarelli, A., Bestmann, P., Billen, R., Boccone, V., Bouzoud, A.P., Bracco, C., Braun, H., Bruce, R., Brugger, M., Calatroni, S., Caspers, M. Cauchi, F. Cerruti, R. Chamizo, A. Cherif, E. Chiaveri, A. Dallochio, D. Deboy, B. Dehning, M. Donze, N. Hilleret, E.B. Holzer, D. Jacquet, J.B. Jeanneret, J.M. Jimenez, M. Jonker, F., Kadi, Y., Kershaw, K., Kruk, G., Lamont, M., Lari, L., Lendaro, J., Lettry, J., Losito, R., Magistris, M., Masi, A., Mayer, M., Métral, E., Mitifiot, C., Mounet, N., Perret, R., Perrolaz, S., Previtali, V., Rathjen, C., Redaelli, S., Robert-Demolaize, G., Roderick, C., Roesler, S., Rossi, A., Ruggiero, F., Santana, M., Schmidt, R., Sievers, P., Sobczak, M., Tsoulou, K., Valentino, G., Veyrunes, E., Vincke, H., Vlachoudis, V., Weiler, T., Wenninger, J., Wollmann, D., CERN, Geneva, Switzerland. Kaltchev, D. et al, TRIUMF, Canada. Bayshev, I., IHEP, Russia. Markiewicz, T., et al, SLAC, USA. Mokhov, N., et al, FNAL, USA., Ryazanov, A., et al, Kurchatov, Russia., Sammut, N., et al, University Malta, Malta., Simos, N., et al, BNL, USA., 2012, Proceedings of HB2010, Morschach, Switzerland, MOIB03, Collimation for the LHC high intensity beams, CERN, Geneva, Switzerland, pp. 21-33

[9] Jewell, M. C., Boutboul, T., Oberli, L.-R., Liu, F., Wu, Y., Vostner, A., Isono, T., Takahashi, Y., Park, S.-H., Shikov, A., Vorobieva, A., Martovetsky, N., Seo, K., Bessette, D., Devred, A., June 2010, World-Wide Benchmarking of ITER Nb_3Sn Strand Test Facilities, IEEE transactions on applied superconductivity, Vol. 20, NO. 3, 4 p.

[10] Chui[a], T., Zhang[a], B., Barmatz[a], M., Hahn[a], I., Penanen[a], K., Hays[a], C., Strayer[a], D., Liu[a], Y., Zhong[a], F., Young[a],J., Radey[a], T., Jones[a], J., Galitzki[a], N., Li[a], N., Lo[a], L., Horikoshi[a], S., Hollen[a], S., Paik[b] H.J., [a] Jet Propulsion Laboratory, Low Temperature Science and Quantum Sensor Group, California Institute of Technology, 4800 Oak Grove Drive, MS 79-24, Pasadena, CA 91109, USA. [b] Department of Physics, University of Maryland, College Park, MD 20742, USA., February-March 2006, Cryogenics for lunar exploration, Cryogenics, Volume 46, Issues 2-3, pp. 74-81

[11] Feldheim, V., Lybaert, P., Thermique Numérique, Umons, Mons, 2012-2013 Edition

[12] ANSYS CFX Solver Theory Guide, Release 12.0, April 2009

[13] Menter, F. R., "Two-Equation Eddy-Viscosity Turbulence Models for Engineering Applications," AIAA Journal, Vol. 32, No. 8, August 1994, pages 1598-1605.

[14] Menter, F. R., Kuntz, M., and Langtry, R., "Ten Years of Industrial Experience with the SST Turbulence Model," Turbulence, Heat and Mass Transfer 4, ed: K. Hanjalic, Y. Nagano, and M. Tummers, Begell House, Inc., 2003, pages 625 - 632.

[15] NASA, Langley Research Center, Turbulence Modeling Resource, Retrieved September 29th 2013

http://turbmodels.larc.nasa.gov/sst.html

[16] CFD-Wiki - a community project to create the ultimate, free Computational Fluid Dynamics reference, Retrieved September 29th 2013

http://www.cfd-online.com/Wiki/SST_k-omega_model

[17] Hachem, E., September 2009, Stabilized finite element method for heat transfer and turbulent flows inside industrial furnaces, Ecole des mines de Paris, Centre de mise en forme des matériaux, Sophia Antipolis, France

[18] Kreider, K. F., (ed.) 2001, Handbook of Heating, Ventilation and Air Conditioning, CRC Press, Boca raton, FL.

[19] Rhie, C.M., Chow, W.L., 1982, A Numerical Study of the Turbulent Flow Past an Isolated Airfoil with Trailing Edge Separation, AIAA Paper 82-0998

[20] S. Majumdar, May 26th 1987, Role of Underrelaxation in Momentum Interpolation for Calculation of Flow with Nonstaggered Grids, Numerical Heat Transfer pp. 13:125-132

[21] Auchmann, B., 25th of February, 2D Structural Analysis of 11-T Pole-Loading Magnet in Yoking Press, CERN Internal report

[22] Jackson, J. D., 1999, Classical electrodynamics (3rd ed.). New York, [NY.]: Wiley. ISBN 0-471-30932-X

[23] July, 2012, The design meeting of the section between Savary, F., Lackner, F., Auchmann, B., Murtomäki, J.

[24] Lackner, F., The press of the company Fjellman with a dummy magnet assembly to be welded.

[25] The Ansys APDL-model of the 1-in-1 dipole magnet (used to calculate the results of the second chapter) was originally built by Bernhard Auchmann. The author further extended the model with contributions of B. Auchmann.

[26] Single aperture dipole magnet intersections produced by the author using Bernhard Auchmann's APDL-model. As an exeption to this the cradle model intersections produced by the author from the model of the cradle of the author.

[27] Retrieved from CERN CDS on June 27th 2012, The part can be found with CDS Drawing number: LHCMBHSP0001

[28] Grospelier, E., Up cradle for skinning press V2, October 2012

[29] Grospelier, E., Low cradle for skinning press V2, October 2012

[30] Smekens, D., Short Mechanical Model, Pole Loading Concept, L: 120 mm, model by David Smekens, CERN

[31] Smekens, D., Preparing FNAL PC01 for pole loading, Extremity from practice coil (Nb3Sn) ; Integrated poles removed, photo taken by David Smekens, CERN

[32] A fan curve for ⌀355 x 102 x 236,5 mm fan without case).

[33] ITER, The machine, Magnets, Retrieved June 22th 2013

http://www.iter.org/mach/magnets

[34] Technology department (TE), Retrieved June 22th 2013

http://te-dep.web.cern.ch/te-dep/

[35] Magnets, Superconductors and Cryostats (MSC), Retrieved June 22th 2013

http://te-dep.web.cern.ch/te-dep/structure/MSC/

[36] Large Magnet Facility (LMF), Retrieved June 22th 2013

http://te-dep.web.cern.ch/te-dep/structure/MSC/LMF/index.html

[37] HL-LHC: High Luminosity Large Hadron Collider, Retrieved June 22th 2013

http://hilumilhc.web.cern.ch/HiLumiLHC/about/

[38] Peterson, T., "Explain it in 60 seconds: Magnet Quench", Symmetry Magazine, Fermilab/SLAC, Retrieved February 16th 2013.

http://www.symmetrymagazine.org/article/november-2008/explain-it-in-60-seconds-magnet-quench

[39] ANSYS Contact Technology Guide, ANSYS release 9.0, November 2004, Retrieved September 12th 2013

http://www.cae.tntech.edu/c̃hriswilson/FEA/ANSYS/g_ctec90.pdf

[40] Elements reference, Release 12.1, 2009, Documentation for ANSYS, Retrieved September 16th 2013

http://orange.engr.ucdavis.edu/Documentation12.1/121/ans_elem.pdf

[41] ANSYS Fluent help, Release 13.0, The discrete transfer model, 2010, Retrieved August 1st 2013

http://www.sharcnet.ca/Software/Fluent13/help/cfx_mod/i1311106.html

[42] Johnson, D., Principles of Simulating Contact Between Parts using ANSYS, Introduction, Penn State-Erie, Erie, Pennsylvania, USA, Retrieved September 16th 2013

http://www.ansys.com/staticassets/ANSYS/staticassets/resourcelibrary/confpaper/2002-Int-ANSYS-Conf-201.PDF

[43] Kurganov, V. A., Heat transfer coefficient, Retrieved September 24th 2013

http://www.thermopedia.com/content/841/

[44] Krüger, Technical Bulletin TBN002.2/2003, February 2003, Retrieved September 16th 2013

http://www.krugerfan.com/brochure/publications/TBN002.pdf

[45] ANSYS 14.5 Help, ANSYS Release 14.5, 2012

[46] CFD-Wiki - a community project to create the ultimate, free Computational Fluid Dynamics reference, Retrieved September 17th 2013

http://www.cfd-online.com

[47] ANSYS Fluent 14.0 Help, ANSYS Release 14.0, SHARCNET is a consortium of Canadian academic institutions who share a network of high performance computers.

http://www.sharcnet.ca/

[48] Fan performance and selection, Retrieved September 17th 2013

http://wiki.gekgasifier.com/f/Fan+Performance+and+Selection.pdf

[49] All you need to know about fans, Retrieved March 8th 2012

http://www.fl-eng.com/_lib/pdf/specs/cooling_guide.pdf

[50] Weisstein, E., Eric Weisstein's World of Physics, 1996-2007, Retrieved March 8th 2012

http://scienceworld.wolfram.com/physics/ForceDensity.html

A. APPENDIX

Material property	T=1.8 K	T=293 K	Unit
Impregnated cable (conductor)			
Young's modulus E_x, E_y	30 000	27 000	MPa
Shear modulus G_{xy}	16 541	=	MPa
Major Poisson's ratio ν_{xy}	0.33	=	-
Secant coeff. of thermal exp. α_x	3.3/(1000×293)	=	1/K
Secant coeff. of thermal exp. α_y	2.9/(1000×293)	=	1/K
Wedge, copper			
Young's modulus E_x, E_y	130 000	=	MPa
Minor Poisson's ratio ν_{yx}	0.3	=	-
Secant coeff. of thermal exp. α_x	3.6/(1000×293)	=	1/K
Secant coeff. of thermal exp. α_y	3.3/(1000×293)	=	1/K
Insulation			
Young's modulus E_x	34 000	28 000	MPa
Young's modulus E_y	23 000	14 000	MPa
Shear modulus G_{xy}	8 640	5 260	MPa
Minor Poisson's ratio ν_{yx}	0.33	=	-
Secant coeff. of thermal exp. α_x, α_y	2.4/(1000×293)	=	1/K
Ground insulation, Kapton			
Young's modulus E_x, E_y	2 500	=	MPa
Minor Poisson's ratio ν_{yx}	0.34	=	-
Secant coeff. of thermal exp. α_x, α_y	5.8/(1000×293)	=	1/K
Loading plate, titanium			
Young's modulus E_x, E_y	125 000	115 000	MPa
Major Poisson's ratio ν_{xy}	0.3	=	-
Secant coeff. of thermal exp. α_x, α_y	1.7/(1000×293)	=	1/K
Key, stainless steel			
Young's modulus E_x, E_y	210 000	190 000	MPa
Minor Poisson's ratio ν_{yx}	0.3	=	-
Secant coeff. of thermal exp. α_x, α_y	2.64/(1000×293)	=	1/K
Collaring shoe, stainl. steel - 1 mm thick			
Young's modulus E_x, E_y	215 000	195 000	MPa
Major Poisson's ratio ν_{xy}	0.3	=	-
Secant coeff. of thermal exp. α_x, α_y	2.7/(1000×293)	=	1/K

Table A.1: 1/2 The material properties of the 1-in-1 magnet model. Part of the material properties are linearly dependent on the temperature.

Material property	T=1.8 K	T=293 K	Unit
Collar, stainless steel			
Young's modulus E_x, E_y	215 000	195 000	MPa
Major Poisson's ratio ν_{xy}	0.3	=	-
Secant coeff. of thermal exp. α_x, α_y	2.7/(1000×293)	=	
Yoke, steel			
Young's modulus E_x, E_y	225 000	210 000	MPa
Minor Poisson's ratio ν_{yx}	0.3	=	-
Secant coeff. of thermal exp. α_x, α_y	2.05/(1000×293)	=	1/K
Shell, austenitic steel			
Young's modulus E_x, E_y	215 000	195 000	MPa
Major Poisson's ratio ν_{xy}	0.3	=	-
Secant coeff. of thermal exp. α_x, α_y	2.9/(1000×293)	=	1/K
Press, steel			
Young's modulus E_x, E_y	215 000	195 000	MPa
Major Poisson's ratio ν_{xy}	0.3	=	-
Secant coeff. of thermal exp. α_x, α_y	2.7/(1000×293)	=	1/K

Table A.2: 2/2 The material properties of the 1-in-1 magnet model. Part of the material properties are linearly dependent on the temperature.

Argon	Setting	Unit
Basic settings		
Option	Pure Substance	
Material Group	User	
Thermodynamic State	Gas	
Material Properties		
Option	General Material	
Thermodynamic Properties		
Equation of State		
Option	Value	
Molar Mass	39.94	kg/kmol
Density	1.6337	kg/m^3
Specific Heat Capacity	521.56	J/kgK
Specific Heat Type	Constant Pressure	
Reference State		
Option	Specified Point	
Reference Temperature	25	°C
Reference Pressure	1	atm
Reference Specific Enthalphy	0	J/kg
Reference Specific Entropy	0	J/kgK
Transport Properties		
Option	Value	
Dynamic Viscosity	0.000022606	kg/ms
Thermal Conductivity	0.017639	W/mK

Table A.3: The material properties of argon.

Steel	Setting	Unit
Basic settings		
Option	Pure Substance	
Material group	CHT Solids, Particle Solids	
Thermodynamic State	Solid	
Material Properties		
Option	General Material	
Thermodynamic Properties		
Equation of State		
Option	Value	
Molar Mass	55.85	kg/kmol
Density	7854	kg/m^3
Specific Heat Capacity	434	J/kgK
Reference State		
Option	Specified Point	
Reference Temperature	25	°C
Reference Specific Enthalphy	0	J/kg
Reference Specific Entropy	0	J/kgK
Transport Properties		
Option	Value	W/mK
Thermal Conductivity	60.5	W/mK
Boundaries of Steel		
Retort Container Wall		
Option	Opaque	
Emissivity	0.9	
Diffuse fraction (Diffuse reflectivity)	1	
Fixture Wall		
Option	Opaque	
Emissivity	0.8	
Diffuse fraction (Diffuse reflectivity)	1	

Table A.4: The material properties of the steel used in the fixture.

$\dot{V}_A \left(\frac{m^3}{s}\right)$	$p_A\ (Pa)$	$\dot{V}_B \left(\frac{m^3}{s}\right)$	$p_B\ (Pa)$
0.000	128.11	0.000	24.05
0.014	128.10	0.007	24.04
0.055	128.00	0.022	24.03
0.103	126.00	0.043	24.02
0.142	123.00	0.057	24.01
0.200	117.00	0.088	22.00
0.256	104.00	0.111	20.00
0.328	76.50	0.142	14.00
0.399	30.00	0.157	10.00
0.439	1.50	0.174	6.00
0.444	0.00	0.189	0.000

Table A.5: The Fan curves in tabular form.

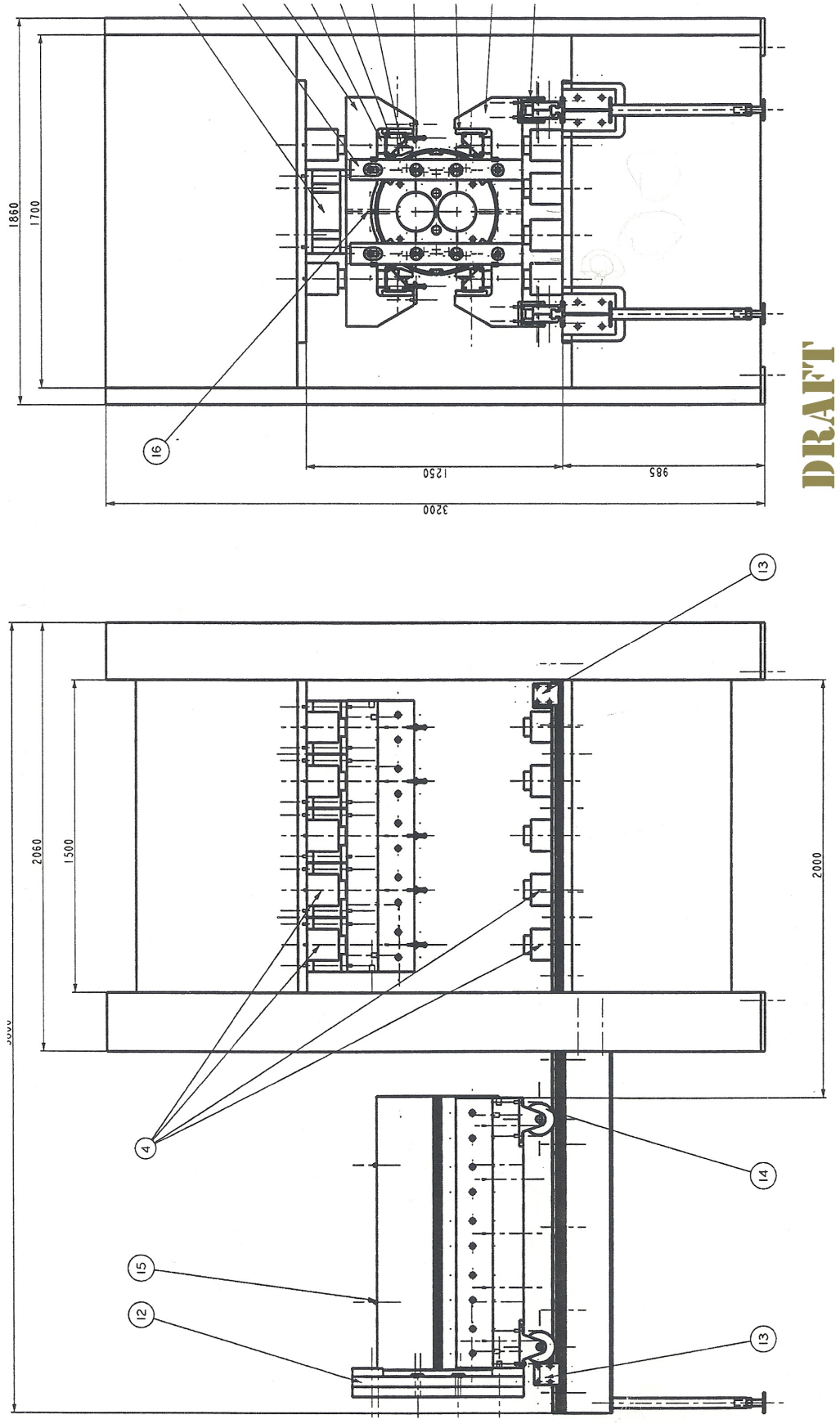

Figure A.1: Obsolete dimensions of the unmodified design: The press with the magnet assembly inside the original cradles, and a magnet assembly on the original sledge.

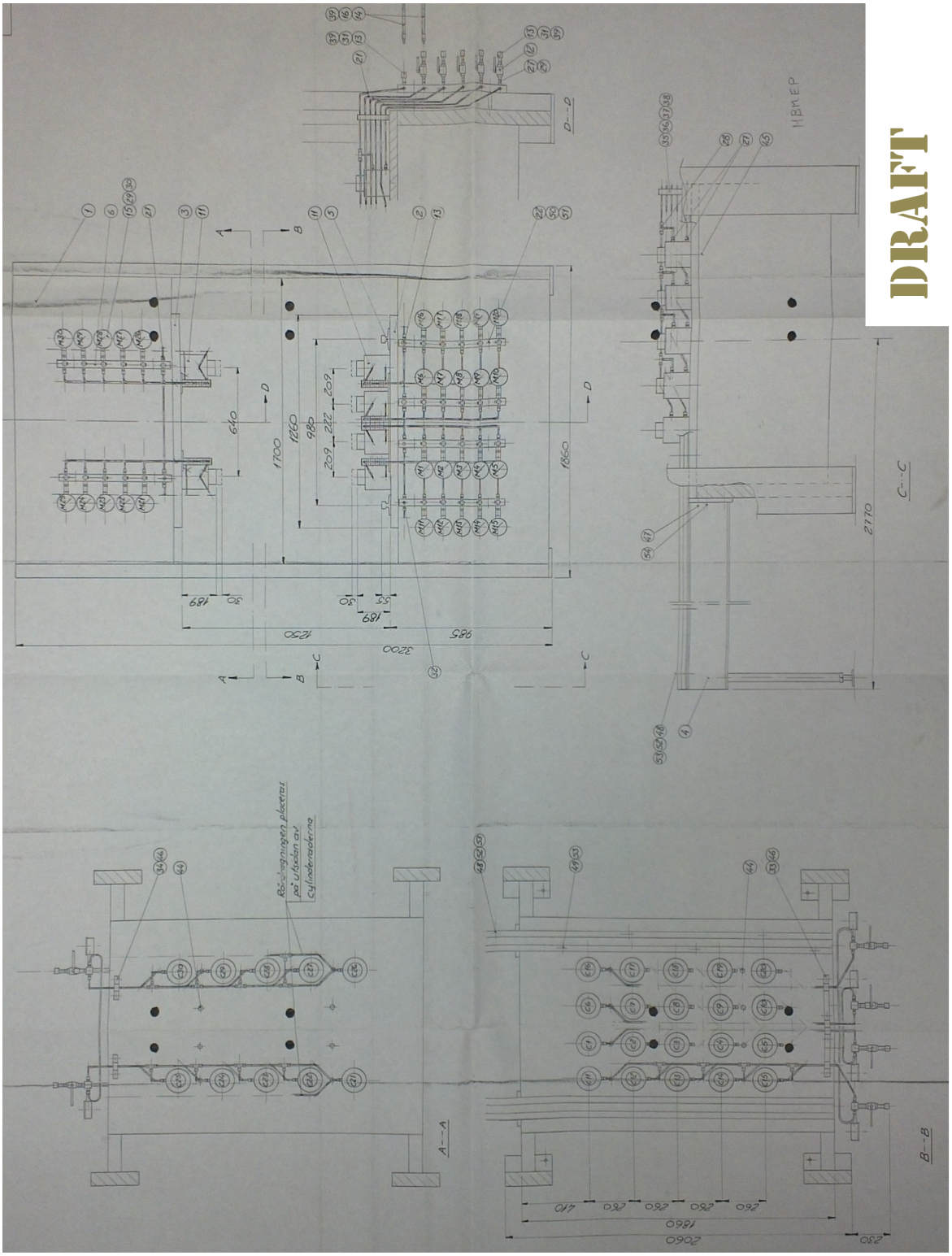

Figure A.2: Obsolete dimensions of the unmodified design: The hydraulic cylinder configuration of the press.

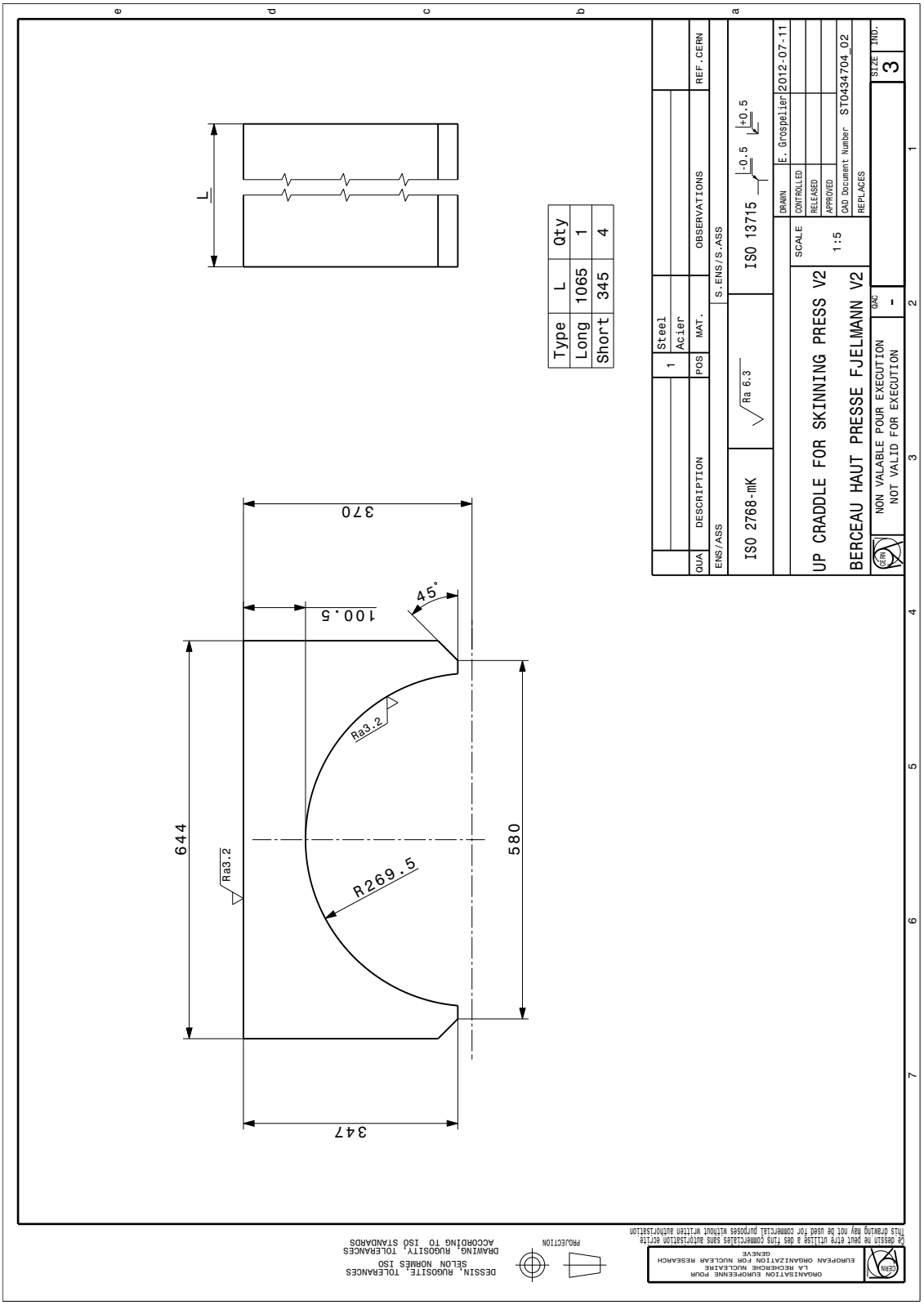

Figure A.3: The upper cradle. [4]

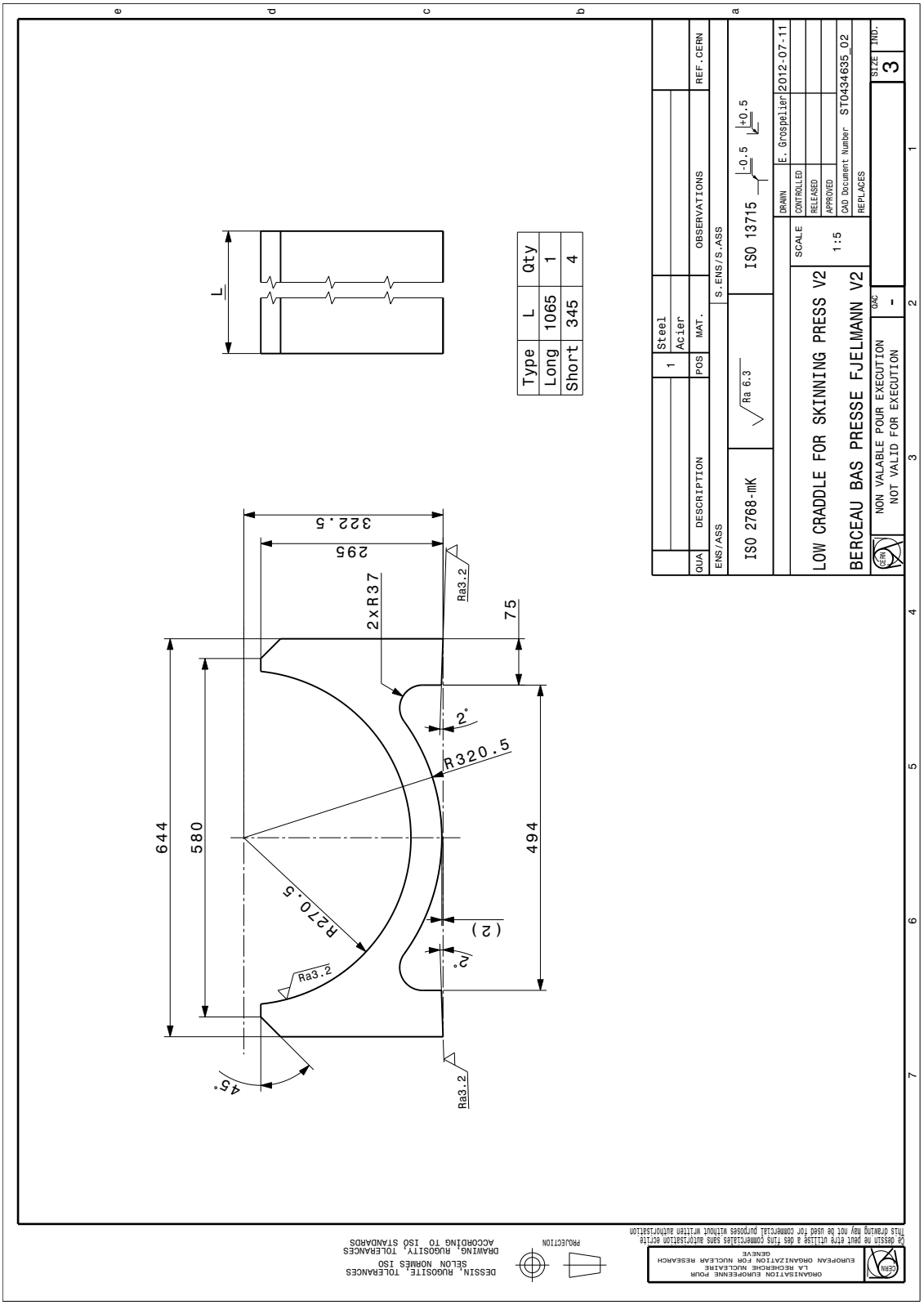

Figure A.4: The lower cradle. [4]

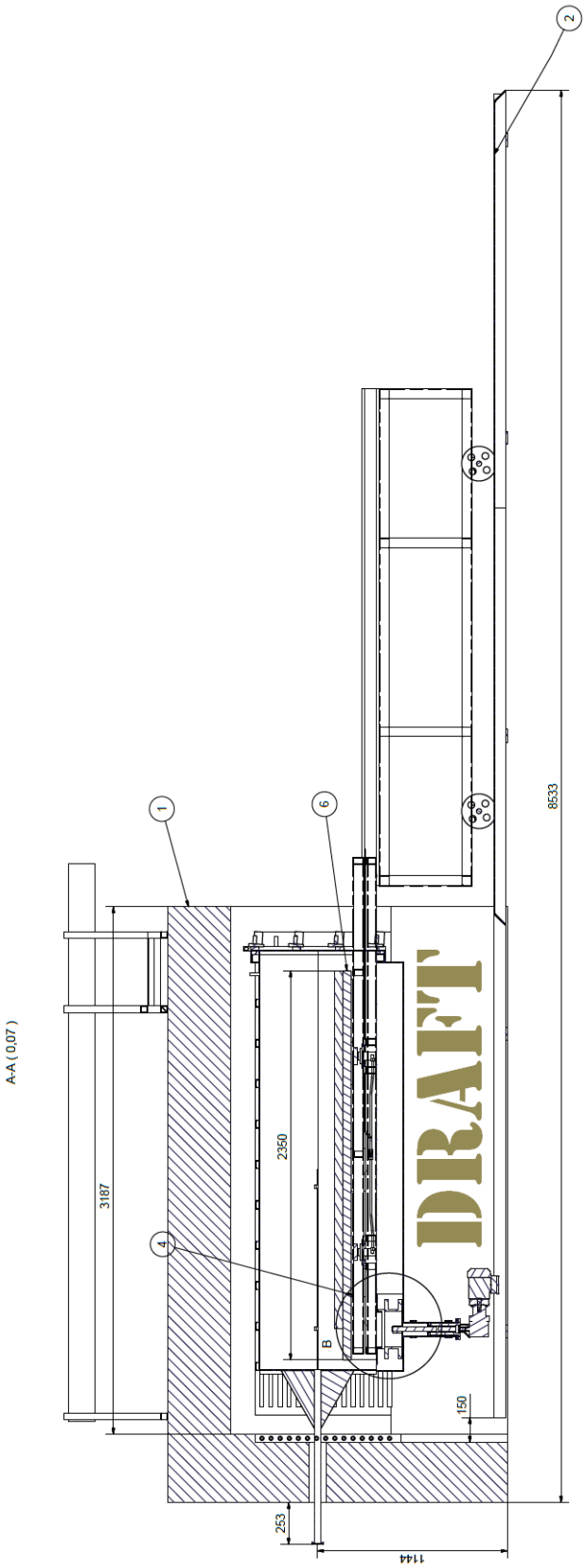

Figure A.5: Drawing of the furnace - a side half-cut

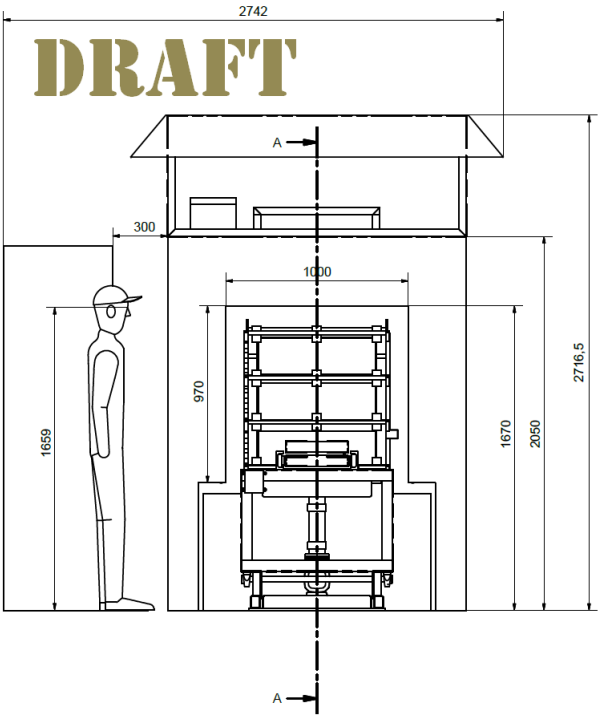

Figure A.6: Drawing of the furnace - front side

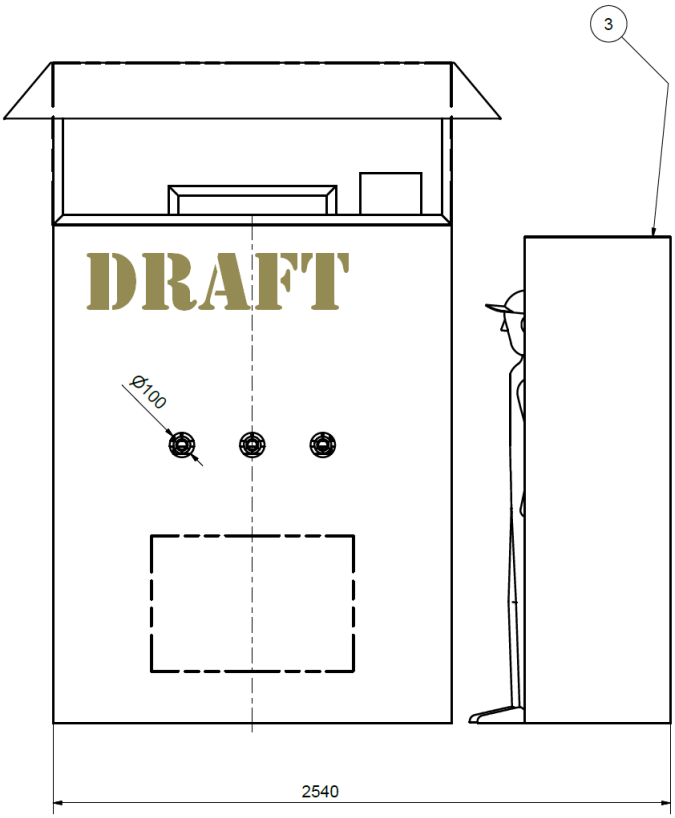

Figure A.7: Drawing of the furnace - back side